ADVANCED AIR ELECTRODE MATERIALS FOR HIGH-PERFORMANCE REVERSIBLE PROTONIC CERAMIC CELLS

YU NA

PhD

The Hong Kong Polytechnic University

2025

The Hong Kong Polytechnic University
Department of Building and Real Estate

Advanced Air Electrode Materials for High-Performance Reversible Protonic Ceramic Cells

YU Na

A thesis submitted in partial fulfilment of the
requirements for the degree of Doctor of Philosophy

August 2024

CERTIFICATE OF ORIGINALITY

I hereby declare that this thesis is my own work and that, to the best of my knowledge and belief, it reproduces no material previously published or written, nor material that has been accepted for the award of another degree or diploma, except where due acknowledgment has been made in the text.

________________________ (Signed)

YU Na (Name of Student)

ABSTRACT

The development of efficient and environmentally friendly energy conversion and storage devices is crucial for advancing renewable energy. Solid oxide cells (SOCs) demonstrate significant potential due to their high energy conversion efficiency and environmental benefits. However, SOCs typically operate at temperatures exceeding 700 °C, which accelerates component degradation and increases system costs.

Reversible protonic ceramic cells (RePCCs), a type of proton-conducting SOC, operate at intermediate temperatures (350-650 °C), extending component lifespan and reducing costs. However, the slow kinetics of the oxygen reduction reaction (ORR) and water oxidation reaction (WOR) at the air electrode limit the performance of these cells. Developing advanced air electrode materials is essential to enhance efficiency. Currently, most air electrode materials are Co-based perovskites, which exhibit excellent performance due to the catalytic activity of Co. However, Co-based electrodes generally have a high thermal expansion coefficient (TEC), leading to electrode delamination during long-term operation. Fe-based air electrodes, with relatively lower TEC and significantly lower costs compared to Co-based electrodes, are promising candidates for RePCC air electrodes.

This study focuses on the modification of Fe-based Ruddlesden-Popper (RP) layered perovskite oxides. RP layered perovskites are promising candidates for RePCC air electrodes due to their excellent oxygen transport properties and hydration characteristics, which make them $H^+/O^{2-}/e^-$ triple-conductive oxides. However, RP materials tend to decompose under humid atmospheres during long-term operation and exhibit lower activity compared to Co-based electrodes. In this thesis, we employ strategies such as oxygen-proton balancing, elemental doping, and self-assembly to develop a series of high-performance, high-stability Fe-based RP-type RePCC air electrodes, overcoming the low electrocatalytic activity and poor stability of conventional RP materials in steam environments.

Firstly, a high-valent ion doping strategy is used to regulate the oxygen and proton properties of RP materials under air electrode working conditions. Moderate doping effectively optimizes oxygen/water surface exchange, thereby enhancing electrochemical activity and providing guidance for the development of RP materials as RePCC air electrodes.

Secondly, a co-substitution strategy involving A-site vacancies and B-site elements is employed to improve the stability and electrochemical performance of RP perovskites, enabling the preparation of efficient RePCC air electrodes. High-valent Nb doping enhances phase and thermal stability, while appropriate A-site Sr deficiencies create oxygen vacancies to compensate for performance losses caused by Nb doping while maintaining the stability of the parent phase.

Furthermore, a self-assembly strategy is utilized to prepare a series of multiphase nanocomposite materials. The complementary properties of the individual phases collectively enhance electrode performance and stability. Additionally, phase regulation of the self-assembled composites is achieved by adjusting elemental composition. Optimized phase proportions lead to RePCC air electrode materials with excellent electrochemical activity and durability.

This study provides a comprehensive investigation of the reaction mechanisms, current research progress, and modification methods for air electrodes. Strategies including oxygen-proton balancing, the dual-modification approach, and controllable self-assembly material design are identified as crucial for further improving RePCC performance.

AUTHOR’S PUBLICATIONS

1. **Yu, N.**, Bello, I. T., Chen, X. *et al.* Rational design of Ruddlesden-Popper perovskite ferrites as air electrode for highly active and durable reversible protonic ceramic cells. *Nano-Micro Letter* **2024**, 16, 177.
2. **Yu, N.**, Liu, T., Chen, X. *et al.* Co-generation of liquid chemicals and electricity over Co-Fe alloy/perovskite fuel electrode catalyst in a propane fueled solid oxide fuel cell. *Separation and Purification Technology* **2022**, 291, 120890.
3. Chen, X., **Yu, N.**,Liu, T. et al. Synergistic bulk and surface engineering for expeditious and durable reversible protonic ceramic electrochemical cells air electrode. *Advanced Materials* **2024**, 2403998.
4. Chen, X., **Yu, N.**, Bello, I. T. et al. Facile anion engineering: A pathway to realizing enhanced triple conductivity in oxygen electrodes for reversible protonic ceramic electrochemical cells. *Energy Storage Materials* **2023**, 63, 103056.
5. Chen, X., **Yu, N.,** Bello, I. T. et al. Understanding the oxygen reduction reaction in the hierarchically oriented composite air electrode with open, straight pores. *Separation and Purification Technology* **2023**, 325, 124713.
6. Bello, I. T., **Yu, N.**, Song, Y. et al. Electrokinetic insights into the triple ionic and electronic conductivity of a novel nanocomposite functional material for protonic ceramic fuel cells. *Small* **2022,** 18, 2203207.

ACKNOWLEDGEMENTS

I would like to express my deepest gratitude to my Ph.D. supervisor, Prof. NI Meng. His encouragement, guidance, and support have enabled me to overcome numerous challenges along the way. I still remember when I was anxious about not having published any papers, he was more concerned about whether I was happy. His professional guidance, as well as his kindness, integrity, and empathy, have inspired me to become a better person.

Additionally, I want to thank my colleagues in the research group. We spent our days together, managing the lab and striving for our academic goals. Their assistance and encouragement were a source of comfort during many tough days. I would like to express my special gratitude to Dr. SONG Yufei for his guidance in my research and Dr. LIU Tong for his support with the experimental testing.

Furthermore, I want to thank my family, who have always been as accommodating and supportive as possible. My mother endured all my bad temper, and my father calmly dispelled all my worries. Every time I packed my bags and traveled far away, they wholeheartedly encouraged and supported my decisions, silently dealing with the sadness of parting as they watched me leave. Their respect, understanding, support, and love have helped me grow into an independent and self-aware person.

I also want to thank my boyfriend, CHEN Xi. His companionship over the past two years has made my Ph.D. journey less lonely. Every bit of my progress is due to his support and help. His qualities of rationality, tolerance, focus, diligence, and

kindness have profoundly influenced me.

Finally, I’m grateful for the staff of BRE, the staff at the Material Research Center of Hong Kong Polytechnic University, and everyone who has helped me. Their support has allowed me to successfully navigate this important stage of my life.

TABLE OF CONTENTS

LIST OF FIGURES

LIST OF TABLES

LIST OF ABBREVIATIONS

ASR	Area specific resistance
BZCY	$BaZr_{0.7}Ce_{0.2}Y_{0.1}O_{3-\delta}$
BZCYYb	$BaZr_{0.1}Ce_{0.7}Y_{0.1}Yb_{0.1}O_{3-\delta}$
D_{chem}	Bulk diffusion coefficient
DFT	Density functional theory
DOS	Density of State
DRT	Distribution of relaxation time
E_a	Activation energy
EC	Electrolysis cell
ECR	Electrical conductivity relaxation
EDTA	Ethylenediaminetetraacetic acid
EDX	Energy-dispersive X-ray spectroscopy
EIS	Electrochemical impedance spectrum
FC	Fuel cell
FT-IR	Fourier-transform infrared spectroscopy
HAADF-STEM	High-angle annular dark-field scanning transmission electron microscopy
ICP-OES	Inductively coupled plasma optical emission spectroscopy
k_{chem}	Surface exchange coefficient
MIEC	Mixed ionic and electronic conductor
ORR	Oxygen reduction reaction
O_2-TPD	Oxygen temperature programming desorption
PCEC	Protonic ceramic electrolysis cell
PCFC	Protonic ceramic fuel cell
PPD	Peak power density
RePCC	Reversible protonic ceramic cell
R_p	Polarization resistance
RP	Ruddlesden-Popper
SEM	Scanning electron microscope
SOC	Solid oxide cells
SOEC	Solid oxide electrolysis cell
SOFC	Solid oxide fuel cell
TCO	$O^{2-}/H^{+}/e^{-}$ triple conductive oxide
TEC	Thermal expansion coefficient
TEM	Transmission electron microscopy
TG	Thermogravimetric analysis
WOR	Water oxidation reaction
XPS	X-ray photoelectron spectroscopy
XRD	X-ray diffraction

CHAPTER 1 Introduction

1.1 Background

As industrialization progresses, the increased use of fossil fuels has led to the depletion of fossil fuel reserves and significant environmental pollution. There is an urgent need for an energy transition to reduce reliance on fossil fuels. Renewable energy sources, such as solar and wind, have great potential for achieving a sustainable power supply and reducing environmental pollution. However, the non-dispatchable and intermittent nature of these energy sources limits their ability to provide a consistent power supply, necessitating the development of reliable and low-cost grid-scale energy storage and conversion devices to buffer power production fluctuations and thus promote the development and utilization of renewable energy [1-2].

Solid oxide cells (SOCs) have significant advantages in energy conversion and storage [3]. They can convert the chemical energy of various fuels into electricity in fuel cell mode, with energy conversion efficiency far exceeding that of traditional thermal engine systems, and lower emissions. Besides, SOCs can operate in reversible mode, storing power by producing hydrogen through water electrolysis in electrolysis mode [4]. Additionally, the storage capacity of SOCs is not limited by the size of the device but is determined by the capacity of the fuel tank, making them more suitable for long-term energy storage compared to rechargeable batteries.

Depending on the type of electrolyte carrier, SOCs can be classified into traditional oxygen ion-conducting solid oxide cells (SOCs) and reversible protonic ceramic cells

(RePCCs). Compared to traditional oxygen-conducting electrolytes, proton-conducting electrolytes have lower activation energy, enabling RePCCs to operate efficiently at lower temperatures (450-650 °C), whereas typical SOCs operate at 700 °C and above [5-6]. Furthermore, the hydrogen produced by RePCCs in electrolysis mode is pure and dry, facilitating direct storage and use, and avoiding the issues of fuel electrode oxidation and coarsening. The reduced operating temperature and easy collection of exhaust gases significantly lower the system complexity and cost of RePCCs.

Despite these advantages, RePCCs face challenges in practical applications. For instance, under reduced operating temperatures with H_2 fuel, the fuel electrode in RePCCs undergoes only H_2 oxidation/reduction, involving hydrogen bond cleavage and proton transport. However, the reactions occurring at the air electrode are more complex than those in SOCs, as they still involve oxygen ion transport and O=O bond breaking[7]. Considering that the energy barrier for oxygen ion transport is typically twice that of proton transport, operation at intermediate temperatures severely limits the performance of RePCC air electrodes[8].

To date, no material fully meets the comprehensive performance requirements of RePCC air electrodes[9]. For example, Co-based air electrodes, which exhibit excellent catalytic performance, have been widely studied. However, their TEC differs significantly from that of electrolyte materials, leading to electrode delamination during frequent thermal cycling and prolonged operation, posing significant challenges for the stable operation of RePCCs[10].

Novel Fe-based air electrodes, on the other hand, offer promising alternatives due to their favorable catalytic performance, significantly lower TEC compared to Co-based electrodes, and cost-effectiveness[11]. Among these, $Sr_3Fe_2O_{7-\delta}$ (SF)-based Ruddlesden-Popper (RP) layered materials, known for their rapid oxygen migration properties, are particularly suitable for medium- to low-temperature RePCC applications[12]. Their excellent hydration properties also make SF-based RP materials ideal candidates for $H^+/O^{2-}/e^-$ triple-conducting materials[13].

However, the application of SF-based RP materials as RePCC air electrodes remains underexplored, primarily due to their vulnerability to steam and their electrochemical performance, which falls short of that of Co-based air electrodes[14]. Modification strategies such as ion substitution, defect engineering, and phase regulation have the potential to improve the performance and stability of RP-type air electrodes. These approaches may facilitate the development and application of novel, efficient, and stable Fe-based air electrode materials for RePCCs, expanding the range of material options for RePCC air electrodes.

1.2 Research Objective

This study aims to address the critical challenges of air electrodes in intermediate-temperature (450–650 °C) reversible proton ceramic fuel cells (RePCCs) to enhance the overall electrochemical performance and operational stability of the cells. To achieve this objective, targeted design and development of Fe-based air electrode materials are undertaken, with the following strategies proposed:

Firstly, Nb doping is employed to regulate the oxygen vacancy concentration and metal-oxygen bond strength in $Sr_3Fe_2O_{7-\delta}$ (SF)-based RP-type air electrodes, thereby improving the competition between oxygen and protons in the material. This strategy significantly optimizes the electrochemical performance of air electrodes under humid atmospheres.

Secondly, building upon the first strategy, A-site Sr deficiencies are introduced into phase-stabilized Nb-doped RP materials to synergistically enhance the oxygen reduction reaction (ORR) and water oxidation reaction (WOR) stability and activity of Fe-based Ruddlesden-Popper (RP) phase air electrodes. Experimental and computational studies demonstrate the feasibility of this strategy in RePCCs.

Finally, a self-assembly strategy is employed to design nanocomposite air electrodes consisting of an SF-based RP phase and an NiO phase modified on a cubic perovskite parent phase. The synergistic effect of the hydrated RP phase, the NiO phase, with excellent oxygen exchange properties, and the stable cubic parent phase enhances the stability and electrochemical performance of the air electrode.

1.3 Research Originalities

The originality of this study is reflected in three key aspects:

Firstly, a Nb doping strategy is employed to optimize the oxygen-proton balance of SF-based RP air electrodes. The critical role of high-valence element doping in controlling the competition between oxygen and protons is revealed, effectively regulate the oxygen surface exchange and hydration properties in the air electrode and achieving enhanced electrode performance.

Secondly, a straightforward elemental/vacancy dual-doping strategy is applied to Fe-based RP electrodes, significantly increasing the power density and stability of the cells. Experimental and computational studies elucidate the effectiveness of this dual-doping strategy in improving ORR/WOR performance, confirming the feasibility of using RP materials for RePCC air electrodes.

Finally, controllable self-assembled materials are prepared by regulating elemental content. Furthermore, the synergistic effects among multiple phases on the electrocatalytic activity of RePCC air electrodes are demonstrated, providing valuable insights for the development of novel and efficient RePCC air electrodes.

1.4 Outline of This Thesis

This thesis presents the development strategies for highly active and stable Fe-based air electrodes for RePCCs through the design and mechanistic study of electrocatalytic materials. The structure of the thesis is organized into seven chapters as follows:

Chapter 1: Introduction. This chapter outlines the background of RePCCs, including research objectives, status, and challenges in this field. It also introduces the aims, main content, innovations, and structure of this thesis.

Chapter 2: Literature Review. This chapter details the reaction mechanisms and key components of RePCCs. It then analyzes the current state of research and major challenges regarding air electrodes based on their reaction mechanisms and summarizes general strategies for the development and modification of air electrodes.

Chapter 3: Methodology. This chapter presents the preparation and performance characterization methods for air electrodes and RePCCs. The characterization methods include the physicochemical properties of materials, electrochemical performance, and single-cell testing.

Chapter 4: Engineering Synergistic Oxygen-Proton Properties for High-Performance Reversible Protonic Ceramic Cell Air Electrodes. This study introduces an oxygen defect regulation strategy using high-valent Nb doping to enhance the performance and stability of $Sr_3Fe_2O_{7-\delta}$ (SF) air electrode. The Nb-doped $Sr_3Fe_{1.9}Nb_{0.1}O_{7-\delta}$ (SFNb0.1) electrode achieves a balance between surface oxygen/water exchange and bulk ionic transport, while also improving structural stability and thermal expansion.

Chapter 5: Rational Design of Ruddlesden-Popper Perovskite Ferrites as Air Electrode for Highly Active and Durable Reversible Protonic Ceramic Cells. This chapter introduces the study of a novel RP-type material, $Sr_{2.8}Fe_{1.8}Nb_{0.2}O_{7-\delta}$ (D2-SFN), for RePCC air electrodes. Comprehensive experimental characterization and simulation results demonstrate that the Nb/A-site deficiency co-substitution strategy effectively enhances the catalytic activity and stability of SF-based materials.

Chapter 6: Multiphase Self-Assembled High-Efficiency Air Electrode for Reversible Protonic Ceramic Cell Application. This chapter discusses the development of a series of nanocomposite materials by regulating elemental composition. The synergistic effect of the Fe-based simple perovskite parent phase, RP phase, and NiO phase, prepared through the self-assembly method, enhances the electrochemical performance of the electrode.

Chapter 7: Conclusions and Perspectives. This chapter comprehensively summarizes the key findings of the thesis and proposes future directions for the development of RePCC air electrodes.

CHAPTER 2　Literature Review

2.1　Introduction of RePCCs

The operating principles of RePCCs are illustrated in **Figure 2.1** [15]. In fuel cell mode, known as protonic ceramic fuel cells (PCFCs), the fuel electrode facilitates the oxidation of the fuel (e.g., H_2), producing H^+ ions and electrons. The electrons travel through an external circuit to the air electrode, while H^+ ions migrate through the electrolyte to the air electrode. At the air electrode, the oxygen reduction reaction (ORR) occurs, where oxygen combines with the electrons from the external circuit to form O^{2-} ions. These O^{2-} ions then react with the H^+ ions transported through the electrolyte to produce steam at the air electrode. In electrolysis mode, the cell operates as a protonic ceramic electrolysis cell (PCEC). During this process, H_2O is oxidized at the air electrode, releasing e^- and generating H^+ ions and O_2. The H^+ ions pass through the electrolyte to the fuel electrode, where they gain e^- from the external circuit to form H_2.

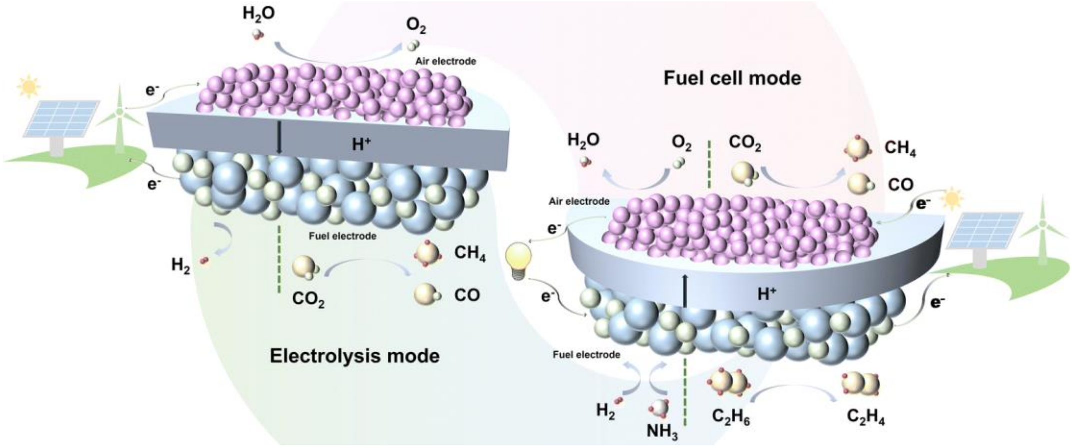

Figure 2.1 The working principle of RePCCs [15].

The operating temperature of ceramic cells typically depends on the temperature required to achieve sufficient ionic conductivity in the electrolyte [16]. Due to the significantly lower activation energy needed for proton conduction (0.4–0.5 eV) compared to O^{2-} ion conduction (0.8–1.2 eV) [17], RePCCs can operate at lower temperatures than SOCs. Proton-conducting electrolytes are typically based on $BaCeO_3$– and $BaZrO_3$–based oxides, such as $BaZr_{0.1}Ce_{0.7}Y_{0.1}Yb_{0.1}O_{3-\delta}$ (BZCYYb1711 or BZCYYb), $BaZr_{0.4}Ce_{0.4}Y_{0.1}Yb_{0.1}O_{3-\delta}$ (BZCYYb4411), and $BaZr_{0.1}Ce_{0.7}Y_{0.2}O_{3-\delta}$ (BZCY), $BaZr_{0.8}Y_{0.2}O_{3-\delta}$ (BZY) [18-20].

The fuel electrode provides reaction sites for fuel oxidation and typically requires excellent electronic and H^+ conductivity, as well as sufficient porosity. It must also exhibit good thermal expansion compatibility with the electrolyte. Fuel gases commonly used include H_2, CH_4, and NH_3, with H_2 being the most prevalent. The most common fuel electrode materials are cermet fuel electrodes, such as Ni-BZCYYb [18]. In this composite material, Ni provides excellent electronic conductivity and catalytic activity, while the BZCYYb oxide ensures good proton conductivity and thermal expansion compatibility with the electrolyte.

Air electrode reactions, involving O=O bond breaking/formation, generally have slower kinetics compared to fuel oxidation reactions. As a result, polarization losses in the cell are predominantly attributed to the air electrode [21]. These losses typically increase as the operating temperature decreases [22]. Thus, enhancing the performance of intermediate-temperature RePCCs relies on the development of more active air electrode materials. Air electrodes require excellent $H^+/e^-/O^{2-}$ triple conductivity, a porous structure, and good thermal and chemical compatibility with the electrolyte. Common air electrode materials include single perovskite oxides, such as

$BaCo_{0.4}Fe_{0.4}Zr_{0.1}Y_{0.1}O_{3-\delta}$ (BCFZY), double perovskite oxides, such as $PrBa_{0.5}Sr_{0.5}Co_{1.5}Fe_{0.5}O_{6-\delta}$ (PBSCF), and RP-type layered perovskite oxides, such as La_2NiO_4 and $Sr_3Fe_2O_{7-\delta}$ [23-26].

2.2 Fundamental of Air Electrode

2.2.1 Reaction Mechanism

Despite the differences between the ORR and water oxidation reaction (WOR), the strategies employed can enhance the performance of both reactions [15]. Therefore, this discussion focuses on the ORR mechanism to avoid the complexity of addressing both reactions simultaneously. The main reaction at the air electrode is represented by Equation 2.1:

$$O_2 + 4H^+ + 4e^- \rightarrow 2H_2O \tag{2.1}$$

The corresponding defect equation is as follows:

$$4OH^- + O_2 + 4e^- \rightarrow 2H_2O + 4O_O^\times \tag{2.2}$$

The ORR is essentially a multi-step process. Based on the literature review, the elementary steps of the RePCC air electrode reaction are illustrated in **Figure 2.2** [7, 13, 27]. The reaction begins with the adsorption and dissociation of O_2. Oxygen molecules from the gas phase diffuse to the electrode surface, where they adsorb and dissociate at oxygen vacancies, forming adsorbed oxygen species (O_{ad}). These oxygen species gain electrons and are reduced to O^{2-}. In mixed ionic-electronic conductor (MIEC) air electrodes, the O^{2-} ions diffuse through the electrode bulk to the three-phase boundary (TPB), where they react with H^+ from the electrolyte to form water (H_2O), which subsequently diffuses back into the gas phase.

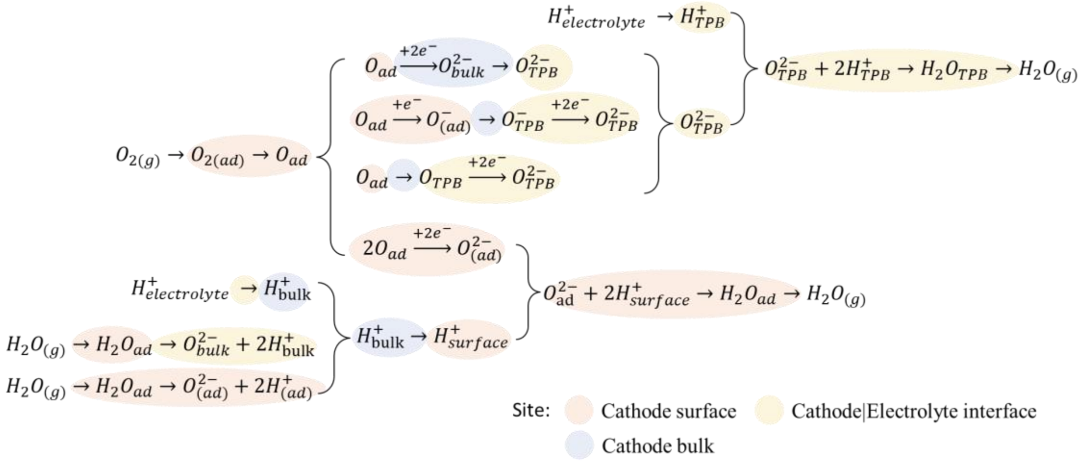

Figure 2.2 ORR elemental steps of the RePCC air electrode.

In H^+- O^{2-}-e^- triple-conducting oxide (TCO) air electrodes, H^+ ions conduct to the TPB and also diffuse through the electrode bulk to the electrode surface, where they react with O^{2-} to form adsorbed water. Since proton transport has a lower energy barrier than oxygen ion transport, optimizing performance can be achieved through bulk proton conduction. Continuous proton conduction pathways require a sufficient number of proton defects in the material. Typically, in humid atmospheres, proton defects in the air electrode are formed via hydration reactions (Equation 2.3) or hydrogenation reactions (Equation 2.4) [28]:

$$H_2O_{ad} + O_O^{\times} + V_O^{\cdot\cdot} \leftrightarrow 2OH_O^{\cdot} \tag{2.3}$$

$$H_2 + 2O_O^{\times} \leftrightarrow 2OH_O^{\cdot} + 2e^- \tag{2.4}$$

It is generally believed that proton defects are primarily transported through the Grotthuss mechanism in both the electrode and electrolyte [29]. Protons bind to lattice oxygen, rotate around the lattice oxygen, and move to adjacent lattice oxygen sites, followed by a jump to neighboring sites, continuing the process of proton rotation and hopping. Materials with proton uptake and proton conductivity typically exhibit water storage properties [7].

According to the research by He et al., the rate of the electrode reaction is closely related to the oxygen/water partial pressures, as represented by Equation 2.5 [27]:

$$R_p \propto p_{O_2}^{m} \cdot p_{H_2O}^{n} \tag{2.5}$$

Where R_p denotes the polarization resistance of the electrode, *m* represents the reaction order concerning the oxygen partial pressure, and *n* represents the reaction order for the water partial pressure. The reaction orders of the oxygen /water partial pressures for each sub-step are listed in **Table 2.1.**

By testing the R$_p$ under varying water and oxygen partial pressures and combining these test results with equivalent circuit simulations or distribution of relaxation time (DRT) analysis, detailed insights into the reaction sub-steps and rate-determining steps of the reactions can be obtained.

Table 2. 1 ORR elemental steps and the reaction orders concerning oxygen and water partial pressures [27].

Step	Elementary reaction	m	n
1	$O_{2(g)} \rightarrow O_{2,ad}$	1	0
2	$O_{ad} + e^- \rightarrow O_{ad}^-$	3/8	0
3	$O_{ad}^- \rightarrow O_{TPB}^-$	1/4	0
4	$O_{TPB}^- \rightarrow O_{TPB}^{2-}$	1/8	0
5	$OH_{electrolyte}^- \rightarrow H_{TPB}^+ + O_{electrolyte}^{2-}$	0	1/2
6	$O_{TPB}^{2-} + H_{TPB}^+ \rightarrow OH_{TPB}^-$	0	1/2
7	$OH_{TPB}^- + H_{TPB}^+ \rightarrow H_2O_{TPB}$	0	1
8	$H_2O_{TPB} \rightarrow H_2O_{(g)}$	0	1

2.2.2 Efficient Properties

To achieve effective ORR and WOR, the air electrode needs to possess several key properties:

Firstly, the air electrode should be porous to facilitate the rapid transport and diffusion of O_2 and H_2O. Rapid gas transport through porous electrodes minimizes energy loss due to concentration polarization. Additionally, the surface of the air electrode must possess sufficient oxygen vacancies, as the O_2 adsorption and dissociation occur at the defect sites. Moreover, the hydration reactions also require the participation of surface oxygen vacancies.

Most importantly, the air electrode should exhibit excellent e^{-}-O^{2-}-H^{+} triple-conducting properties to facilitate ORR/WOR. Electronic conduction follows the polaron hopping mechanism, that is, electrons jump and conduct between the B-site transition metal ion and oxygen ion: B^{n+}-O^{2}-$B^{(n+1)+}$→$B^{(n+1)+}$-O^{-}-$B^{(n+1)+}$→$B^{(n+1)+}$-O^{2-}-B^{n+} [30], where $B^{n+/(n+1)+}$ serves as hopping sites for electrons/holes. More available hopping sites result in higher conductivity. High electronic conductivity promotes oxygen reduction and minimizes ohmic losses. An electronic conductivity greater than 100 S cm^{-1} is ideal but values higher than 0.1 S cm^{-1} are also acceptable for well-designed air electrodes [31-32]. Doping with multivalent transition metal elements can increase electronic conductivity.

Rapid bulk oxygen diffusion facilitates the transport of O^{2-} from the air electrode surface to the electrolyte/air electrode/gas three-phase boundary (TPB), participating in the electrochemical reaction. The migration of O^{2-} is equivalent to the reverse diffusion of oxygen vacancies, thereby constituting a vacancy diffusion mechanism. In most perovskite materials, O^{2-} diffuse via this vacancy diffusion mechanism [28, 33]. The migration of O^{2-} is influenced by the crystal structure. For instance, in cubic perovskites (ABO_3), the diffusion path of O^{2-} is three-dimensional, while in double-layer or RP-type layered perovskites, interlayer differences cause two-dimensional diffusion pathways [34-35]. Additionally, the unit cell volume also affects the ion migration, with larger free volumes reducing the activation energy for O^{2-} migration [36].

Proton conductivity exceeding 10^{-5} S cm^{-1} can extend the ORR/WOR TPB across the entire air electrode surface [37-38], significantly accelerating the reaction rate. Effective proton uptake is critical for achieving high proton conductivity [10]. Proton uptake is influenced by the electronegativity of cations and the concentration of oxygen vacancies [39-40]. Lower electronegativity of A/B-site cations increases the basicity of lattice oxygen, thereby enhancing the material's hydration capacity and proton uptake. Increasing the concentration of oxygen vacancies improves water adsorption [39]. Proton conduction is also affected by the crystal structure symmetry and unit cell volume. Highly symmetric cubic phases are more favorable for proton conduction, while deviations from the cubic phase increase the O-O bond distance, hindering proton hopping. A larger unit cell volume reduces the energy barrier for proton rotation, thereby improving proton conductivity [10].

Optimizing RePCC air electrodes involves balancing conflicting properties [41]. High cobalt content enhances electronic conductivity and catalytic activity but reduces stability and increases electrode TEC [42]. High-basicity elements at the A-site promote hydration reactions but may segregate insulating phases in a steam atmosphere, reducing O_2/H_2O adsorption sites [43-44]. Achieving optimal performance requires balancing these properties and careful consideration of doping ratios. Developing composite materials and modifying electrode structures can help meet diverse performance requirements [38].

Additionally, air electrode materials should remain stable under operating conditions, exhibiting good thermal and chemical stability. They should not react chemically with adjacent components (electrolyte and current collector layer). Matching TEC with adjacent components is crucial to prevent delamination due to temperature fluctuations [45].

2.2.3 Common Materials

Based on crystal structure, air electrode materials are usually categorized into three types: simple perovskite materials, double perovskite materials, and RP-type layered perovskite materials.

Based on conductivity properties, air electrode materials can be divided into four categories: mixed proton-electron conductors (MPECs), mixed oxide ion-electron conductors (MIECs), composite oxide ion-electron and proton conductors (MIEC+PCs), and H^+-O^{2-}-e^- triple conductors (TCOs). The following sections introduce common RePCC air electrode materials according to these classification methods.

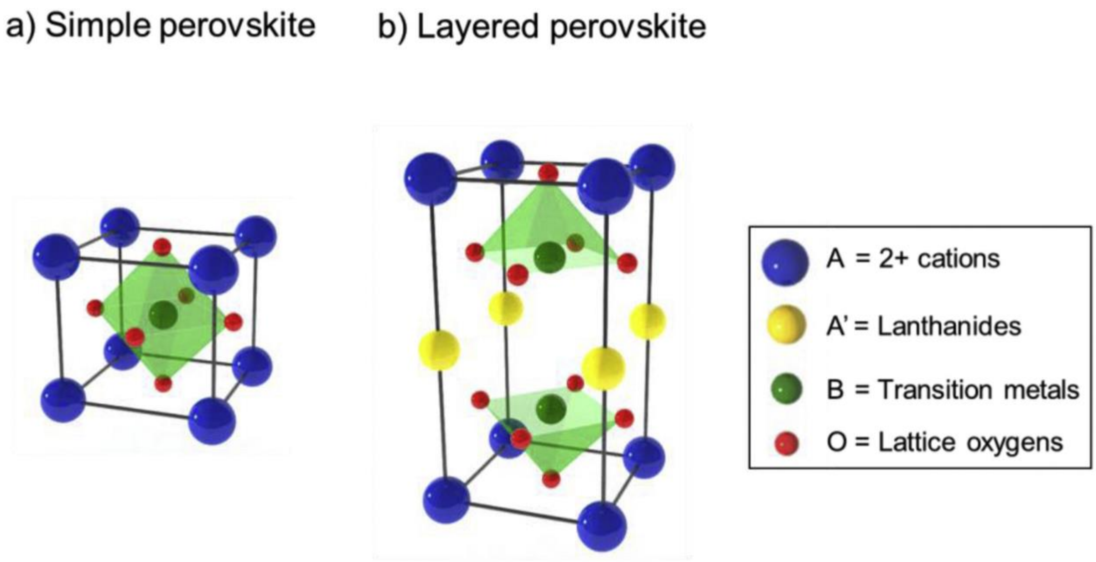

Figure 2.3 Schematic crystal structures of (a) single perovskite and (b) double-layered perovskite [8].

Perovskite-related structures allow significant elemental doping to adjust the properties of air electrodes. The general formula for the structure of simple cubic perovskites is ABO_3 (**Figure 2.3a**), where the A-site is typically occupied by +2 or +3 valence elements in a 12-coordinated structure. The B-site is occupied by +4 or +3 valence transition metal elements, which form an °Ctahedral coordination with oxygen [46]. These B-site elements provide catalytic activity for electrode reactions. Common ABO_3-type air electrode materials include (La, Ba, Sr)(Co, Fe)O_3 and Ba(Ce, Zr)O_3 [47-49].

The general formula of double perovskites is $AA'B_2O_{5+\delta}$, formed by alternating stacking of AO-BO_2-A'O-BO_2 layers (**Figure 2.3b**). A sites are occupied by lanthanide elements (e.g., La, Pr, Nd), A' sites by alkaline earth metals (e.g., Sr, Ba), and B sites by transition metal elements (e.g., Fe, Co, Ni, Mn) [50-51]. The size differences between A and A' cations lead to cation ordering, resulting in properties like two-dimensional diffusion paths for oxygen ions and enhanced proton uptake [52-54]. Additionally, the uneven distribution of oxygen vacancies lowers the average valence state of the transition metal oxide layers adjacent to the AO layers, which is beneficial for proton uptake [55]. Widely used double perovskite layered materials include $Sr_2Fe_{1+x}Mo_{1-x}O_{6-\delta}$ [56], $PrBaCo_2O_{5+\delta}$ [42], $PrBa_{0.5}Sr_{0.5}Co_{1.5}Fe_{0.5}O_{5+\delta}$ [50, 57 58].

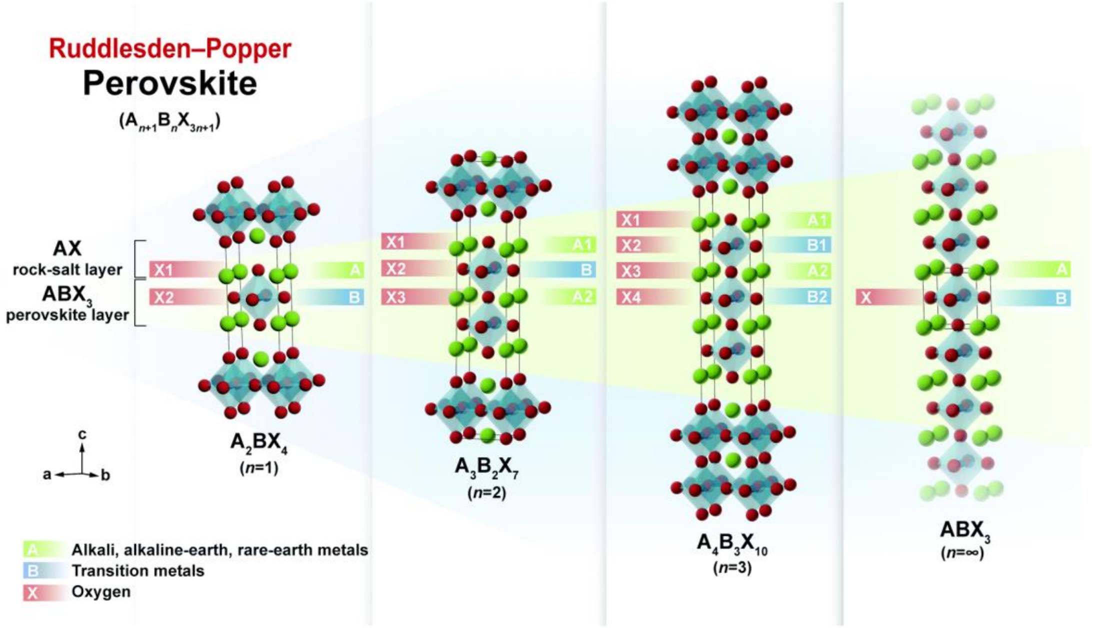

Figure 2.4 Schematic crystal structures of Ruddlesden-Popper perovskites $A_{n+1}B_nO_{3n+1}$ (n=1, 2, 3, +∞) [59].

The general formula of RP-type perovskites is $A_{n+1}B_nO_{3n+1}$ (n=1,2,3,…), consisting of alternating n layers of perovskite and one layer of rock salt. The A-site is typically occupied by lanthanide elements (such as Pr, La) and alkaline earth metals (such as Sr), while the B-site is occupied by transition metal elements (such as Fe, Ni, and Co) [59]. Ideal RP oxides exhibit a layered tetragonal symmetry (space group: I4/mmm) [60], as shown in **Figure 2.4**. The alternating perovskite and rock salt layers provide properties like excellent oxygen migration and good hydration capabilities. For example, in RP-type $Sr_3Fe_2O_7$ air electrode, proton defects preferentially form in the

SrO rock salt layer, while proton diffusion occurs along the perovskite layer's [010] direction, promoting proton migration within the RP phase [13]. RP materials undergo phase decomposition at high temperatures, with higher-order RP phases generally exhibiting better thermal stability compared to lower-order ones [61-62]. Common RP materials include La_2NiO_4 [63], Pr_2NiO_4 [64], and $Sr_3Fe_2O_7$ [38, 65].

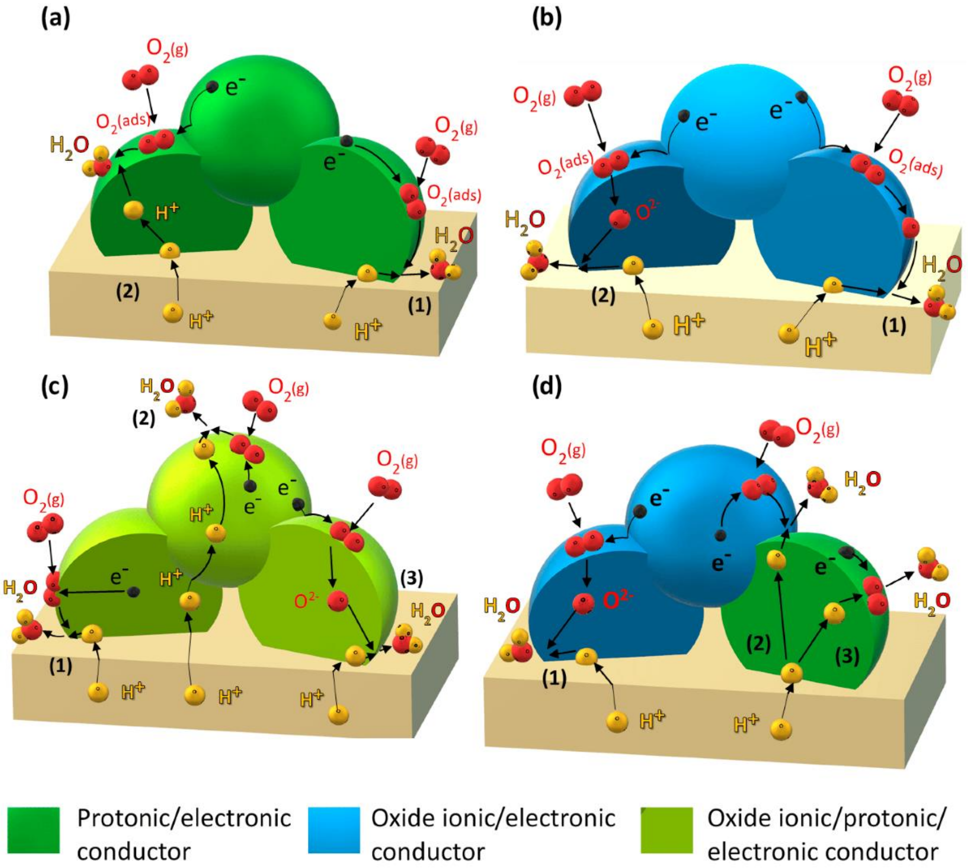

Figure 2.5 Several different conductive materials for PCFC air electrodes. (a) Mixed proton-electron conductors (MPECs). (b) Mixed oxygen-ion-electron conductors (MIECs). (c) TCOs. (d) Composite oxygen-ion-electron conductors and proton conductors (MIEC+PCs) [46].

As shown in **Figure 2.5**, air electrode materials are categorized based on conductivity properties into MIECs, MPECs, MIEC+PCs, and TCOs [46]. Common proton conductors, such as $BaZrO_{3-\delta}$ and $BaCeO_{3-\delta}$ based materials, can become MPECs by doping with variable-valence elements like transition metals (Fe, Co, Ni) or lanthanides (Pr, La)[66]. Early studies showed that doping Pr into $BaCe_{0.8}Y_{0.2}O_{3-\delta}$ significantly improved electrode conductivity, extending the electrochemical reaction sites, and thereby greatly reducing R_p [67]. Similarly, partially substituting Zr with Fe in $BaZr_{0.2}Fe_{0.6}Y_{0.2}O_{3-\delta}$ can lower R_p and increase peak power density (PPD) [68]. However, due to solubility limits, the ability of element doping to enhance electronic conductivity is limited, and materials exhibit poor stability at high doping levels [46]. Thus, MPECs are difficult to develop as ideal air electrode materials.

Typical SOC air electrode materials such as $LaMnO_3$-based materials [69], $La_{0.6}Sr_{0.4}Co_{0.2}Fe_{0.8}O_{3-\delta}$ (LSCF) [70-72], $SrCo_{0.9}Nb_{0.1}O_{3-\delta}$ [73], and $Ba_{0.5}Sr_{0.5}Co_{0.8}Fe_{0.2}O_{3-\delta}$ (BSCF) [74] have been investigated as candidates for RePCC air electrodes. However, MIEC electrodes lack proton conductivity, restricting electrochemical reactions to the electrolyte/air electrode interface, where they react with protons to form H_2O. Despite their initial use in RePCCs, these O^{2-}/e^- conductors have shown unsatisfactory performance.

To develop air electrodes with simultaneous conductivity for O^{2-}, e^-, and H^+, a common approach is to directly combine protonic conductive materials with MIEC materials. For instance, $BaZr_{0.1}Ce_{0.7}Y_{0.2}O_3$ (BZCY172) is often combined with MIEC phase $Sm_{0.5}Sr_{0.5}CoO_{3-\delta}$ (SSC) or $La_{0.6}Sr_{0.4}Co_{0.2}Fe_{0.8}O_{3-\delta}$ (LSCF) [75-76]. Other common composite electrodes include $La_{0.7}Sr_{0.3}FeO_{3-\delta}$-$Ba(Ce_{0.51}Zr_{0.3}Y_{0.15}Zn_{0.04})O_{3-\delta}$ and $BaZr_{0.1}Ce_{0.8}Y_{0.1}O_{3-\delta}$ (BZCY181)-SSC [77-78]. Although physical mixing can enhance proton conductivity, electrode performance remains suboptimal due to issues such as uneven phase mixing, limited interphase contact area, and poor material stability [10].

Optimizing the preparation methods can improve composite electrode performance. For example, a composite electrode prepared by infiltrating $BaCo_{0.4}Fe_{0.4}Zr_{0.1}Y_{0.1}O_{3-\delta}$ (BCFZY) into a $BaCe_{0.6}Zr_{0.3}Y_{0.1}O_{3-\delta}$ (BCZY631) framework achieved a peak power density of 0.455 W cm^{-2} at 550 °C [79]. Similarly, the proton conductor-MIEC composite electrode, nominally $BaCo_{0.7}(Ce_{0.8}Y_{0.2})_{0.3}O_{3-\delta}$ (BCCY), prepared using the one-pot method, achieves a maximum power density of 0.743 W cm^{-2} at 600 °C [80]. Despite advancements in preparation techniques, controlling the fabrication of composite electrodes remains challenging, and most composite electrodes still exhibit less-than-ideal performance.

Advanced O^{2-}/e^{-} conductors serve as the foundation for H^{+}-O^{2-}-e^{-} conductors. By doping MIEC materials, triple conductive materials can be obtained. For instance, the first triple conductor, $PrBa_{0.5}Sr_{0.5}Co_{1.5}Fe_{0.5}O_{5+\delta}$ (PBSCF), was developed by doping Pr into BSCF, demonstrating a peak power density (PPD) of 2.2 W cm^{-2} at 600 ^{o}C when applied in PCFC [81]. Subsequently, promising RePCC air electrodes, such as $NdBa_{0.5}Sr_{0.5}Co_{1.5}Fe_{0.5}O_{5+\delta}$ (NBSCF) and BCFZY, have also been developed [50, 79, 82]. Another approach to developing single-phase triple conductors involves identifying MIEC materials that can undergo hydration reactions, as hydration properties are generally easier to measure than proton conductivity. For example, $Sr_2Fe_{1.5}Mo_{0.5}O_{6-\delta}$ and $Sr_3Fe_2O_{7-\delta}$ materials exhibit proton conductivity in humid atmospheres [13, 39].

2.3 Air Electrode Modification Strategy

The efficient operation of RePCCs requires the optimization of the air electrode's structure, composition, and elemental composition to expand the TPB and accelerate

ORR/WOR at mid-to-low temperatures. Based on a literature review, we have summarized common air electrode modification strategies, including element regulation, surface modification, phase regulation, and microstructure regulation. These modification strategies will be introduced individually in the following sections.

2.3.1 Element Regulation

Element regulation is a common modification method for air electrode materials. As perovskite materials are typically used as air electrode materials for RePCCs, their good stability and excellent doping performance enable the application of elemental regulation strategies. Typically, elemental regulation strategies include ion substitution and defect regulation. Specifically, high-entropy oxides, which are a type of ion substitution strategy, are introduced separately due to their unique properties. Elemental regulation is generally a means to achieve specific functions, and all other air electrode development strategies rely on it. This section primarily summarizes the modification of single-phase air electrodes through elemental regulation.

(1) Ion substitution

Perovskite materials are commonly employed as air electrodes in RePCCs due to their exceptional stability and ability to withstand partial structural distortions while maintaining the original phase. Taking the simple perovskite ABO_3 as an example , ion substitution can occur at the A, B, and O sites. The B-site elements (6-coordinated) and O elements form a BO_6 octahedron that serves as the structural framework, while the larger A-site ions (12-coordinated) occupy the interstitial positions between the octahedra.

The fundamental properties of A-site and B-site elements should be considered when doping, such as the ionic radius, oxidation state, electronegativity, and basicity of the cations to select appropriate A/B-site dopants. Increasing the ionic radius of the B-site cations can help mitigate lattice distortions caused by larger A-site elements, thus preserving the symmetry of the BO_6 octahedron and the cubic structure of the material. Good symmetry and a cubic structure can maximize ion transport efficiency. Generally, the ionic radius of B-site elements should exceed 0.51 Å [83-84].

The ionic radius of A-site elements has a dual impact on the perovskite structure and properties: a larger A-site ionic radius can exacerbate lattice distortion and potentially induce phase transitions; however, the larger the radius of the A-site elements, the greater the free volume, which facilitates the bulk transport of oxygen ions and protons. Additionally, a large unit cell volume can accommodate changes in ionic radii during high-temperature reduction without undergoing phase transitions [83-84]. In mainstream RePCC air electrode materials, A-site elements are primarily Ba, Sr, Pr, and La, with Sr being the most popular for ion substitution due to its suitable ionic radius.

When conducting ion substitution, the differences in ionic radii among A/B/O-site elements also need to be considered, typically described by the tolerance factor t to represent the geometric size differences of ions at different sites:

$$t = \frac{r_A + r_O}{\sqrt{2}(r_B + r_O)} \tag{2.7}$$

Where r_A, r_B, and r_O represent the ionic radii of the A-site, B-site, and O-site ions, respectively. When t = 1, the material exhibits a perfect cubic structure with optimal symmetry. Doping can lead to distortions in the crystal structure; however, to maintain structural stability, the *t* value typically needs to be within the range of 0.75~1.00. When t < 1, as the *t* value decreases, the crystal structure gradually transitions from a cubic phase to rhombohedral and orthorhombic phases. Conversely, when t>1, the BO6 octahedron becomes tilted, resulting in a gradual transformation of the crystal structure from cubic to hexagonal [83, 85].

The oxidation states of the elements must also be considered during doping. To maintain electrical neutrality, the total charge of the doped A-site and B-site elements must equal the total charge of the O-site ions. Consequently, A-site elements can include alkaline earth metals (such as Ca, Sr, and Ba), alkali metals (such as K), or lanthanides (such as La, Pr, and Nd), while B-site elements typically consist of transition metals (such as Co, Fe, Ni, Cu, Zr, and Mo) and lanthanides (such as Ce and Yb). Common combinations of oxidation states for A and B sites include $A^{2+}B^{4+}O_3$ or $A^{3+}B^{3+}O_3$.

The electronic configuration of B-site elements significantly influences the electrochemical performance of the material, as the BO_6 octahedron is generally regarded as the active site for electrochemical reactions [86]. The incorporation of elements with mixed oxidation states at the B-site can enhance the material's electronic conductivity. However, elements with variable oxidation states tend to undergo reduction at high temperatures, resulting in changes in ionic radii and structural transformations. Therefore, elements with constant oxidation states, such as Ti^{4+}, Nb^{5+}, and Zr^{4+} , are often incorporated to suppress phase transitions. Nonetheless, doping with these elements may decrease electronic conductivity and the bulk diffusion rates of oxygen ions; hence, their use should be approached with caution [83].

When low-valence elements are doped into the A-site or B-site, the oxygen vacancy concentration and/or the average oxidation state of the B-site elements tends to increase to maintain electrical neutrality. When elements such as Ba or Ca are incorporated at the A-site, their high basicity can influence the material's proton conductivity and hydration behavior. Generally, a higher basicity of the elements enhances the hydration and proton conductivity of the material [87-88].

The O lattice sites of perovskite materials can also be doped. Non-metal ions such as F^-, Cl^-, S^{2-}, and N^{3-} can typically be introduced to adjust the electronegativity of oxygen sites, thereby enhancing the material's performance. For example, Ni et al. demonstrated that the incorporation of F^- significantly enhanced the activity of oxygen ions, increasing the electrochemical reaction activity of the electrode and elevating the maximum power density of the PCFC from 657 mW cm^{-2} to 977 mW cm^{-2} at 650 ^oC [89]. The highly electronegative F^- ion attracts more electrons, which reduces the valence electron density of the surrounding oxygen ions. This weakens the B-O bond strength, thereby enhancing the activity of lattice oxygen and improving the mobility of both oxygen ions and protons [89-90]. Increasing the electronegativity at the O site can also decrease the electron spin of transition metal ions, thereby suppressing the thermal expansion behavior of the electrode. Conversely, introducing elements with lower electronegativity, such as Cl^- or Br^-, at the O site can reduce the basicity of the material and enhance its resistance to CO_2 [91].

However, it should be noted that although ion substitution is generally aimed at improving a specific property, the introduced elements have a systematic impact on the material's performance. Sometimes doping results in a trade-off in other properties and exceeding a certain doping limit can be counterproductive. For example, Merkle et al. improved the proton uptake performance of $Ba_{0.95}La_{0.05}Fe_{0.8}Zn_{0.2}O_{3-\delta}$ by Zn doping, but when the Zn content exceeded 30%, the electronic conductivity of the material decreased [92]. This implies that the doping limits often need to be carefully explored, and the interactions among various properties remain to be fully understood. Additionally, due to the limitations of doping levels, the performance improvements achieved through ion substitution can sometimes be minimal. For instance, enhancing the electronic conductivity of mixed proton-electron conductor materials through element doping is often less than ideal [66], necessitating the combination of other modification methods to further enhance the relevant properties.

(2) Deficiency engineering

Introducing cation-site defects in the perovskite structure, particularly A-site defects, is an effective strategy for enhancing air electrode performance. Minor A-site or B-site cation vacancies (typically around 10%, but up to 27%) do not disrupt the overall phase structure of perovskite materials [93-96]. However, these defects significantly introduce additional oxygen vacancies to maintain charge neutrality while improving the material's triple-conducting properties[93, 97]. Moreover, the structural instability caused by these cation defects may promote in-situ phase segregation, forming catalytic species on the surface that accelerate reactions involving oxygen and protons[98-99]. These improvements collectively enhance the catalytic activity and durability of RePCC air electrodes.

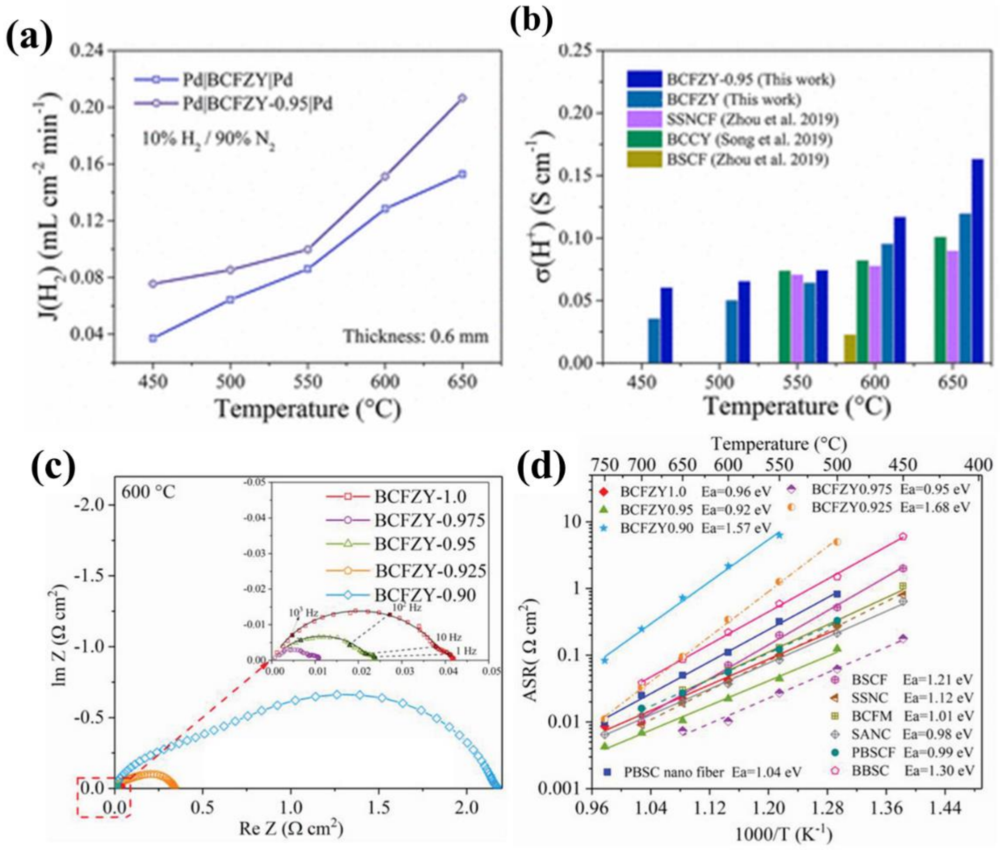

Figure 2. 6 (a) H_2 permeation flux of Pd|Ba$(Co_{0.4}Fe_{0.4}Zr_{0.1}Y_{0.1})_xO_{3-\delta}$ (BCFZY-x, x=0.95, 1.00)|Pd membranes; (b) Proton conductivity of BCFZY-x in 450-650 °C [100]. (c) EIS plots of Ba$(Co_{0.4}Fe_{0.4}Zr_{0.1}Y_{0.1})_xO_{3-\delta}$ electrodes (x = 1.0, 0.975, 0.95, 0.925, and 0.90) obtained at 600 °C in air from symmetrical cells; and (d) Arrhenius plots of the area-specific resistance (ASR) for B(CFZY)$_x$ and some conventional electrodes at different temperatures [101].

Compared to B-site defects, A-site defects in perovskites are energetically more favorable due to the higher coordination numbers and larger ionic radii of A-site cations [102-103]. However, some studies demonstrate that B-site defects can also enhance the electrochemical activity of air electrodes. For instance, introducing 5% B-site vacancies in the Ba$(Co_{0.4}Fe_{0.4}Zr_{0.1}Y_{0.1})_{0.95}O_3-\delta$ (BCFZY-0.95) air electrode improves its proton conductivity and ORR catalytic activity compared to stoichiometric BCFZY[100]

(**Figures 2.6a-b**). Nevertheless, controlling B-site vacancies requires precision, as excessive defects can compromise material activity. For example, studies on BCFZY air electrodes indicate that B-site defects should not exceed 10%[101] (**Figures 2.6c-d**).

(3) High-entropy materials

High-entropy perovskites (HEPs) consist of five or more principal elements, with molar ratios close to equimolar proportions (typically ranging from 5% to 35%) [104-105]. These materials exhibit high configuration entropy, offering enhanced thermodynamic stability compared to conventional materials. Notably, they maintain their stability without compromising catalytic activity[106-107].

High-entropy perovskite oxides (HEPOs) are currently under extensive investigation as air electrode materials for RePCCs. For example, to address the issues of interfacial degradation and delamination between cobalt-based perovskite air electrodes and proton-conducting electrolytes, $BaCo_{0.2}Zn_{0.2}Ga_{0.2}Zr_{0.2}Y_{0.2}O_{3-\delta}$ (BCZGZY) is designed with a cubic-phase structure [108]. The introduction of Zn, Ga, and Y cations not only reduces the average oxidation state of $Co^{3+/4+}$ but also increases the ionic radius at the B-site in the perovskite structure. This modification weakens the Co–O bond strength, facilitating the formation of oxygen vacancies in BCZGZY. Results indicate that BCZGZY exhibits enhanced hydration performance and a reduced TEC of 12.75×10^{-6} K^{-1}. These promote the formation of protonic defects and stabilize the interfacial connection, thereby improving the catalytic activity and stability for ORR/WOR.

Overall, HEPOs demonstrate significant potential as air electrode materials for RePCCs due to their complex atomic arrangement with multivalent cation sites and extensive compositional tunability. However, further exploration and improvement are required. The multicomponent composition leads to complex structures and compositions, complicating the catalytic active sites typically formed by metallic elements during reactions [109-110].

2.3.2 Surface Modification

Considering that the surface of the material serves as the reaction site for the oxygen/steam adsorption and dissociation and transport of $O^{2-}/H^+/e^-$, enhancing surface activity through surface modification is a crucial approach to improving the electrode performance [111-113]. Additionally, surface modification is essential for maintaining the structural integrity and properties of the parent phase of the air electrode, thereby preventing the formation of secondary phases that can degrade performance during electrochemical reactions. Common surface modification strategies for air electrodes include surface infiltration, in-situ exsolution, and core-shell engineering.

(1) Infiltration engineering

The surface infiltration method, which involves infiltrating nanoscale active catalysts onto porous scaffolds, has been demonstrated as a simple and effective approach fo fabricating composite air electrodes. This structure increases the specific surface area of the electrode materials, providing more active sites for electrochemical reactions. Furthermore, since the preparation of infiltrated nanoparticles and scaffolds is relatively independent, the catalytic coating can be prepared at lower temperatures, preserving the nanoparticles' desired morphology. Compared to other nanotechnologies such as chemical vapor deposition and electrospinning, the infiltration method is simpler in terms of process and equipment while requiring less active material to achieve the same loading.

The infiltration technique effectively develops TCO composite materials with ORR/WOR activity and stability under harsh conditions but faces challenges like repeated infiltration and high-temperature sintering, making it time-consuming and costly [114]. Additionally, the infiltration process may fail to ensure the uniform distribution of nanoscale catalytic particles, and the adhesion between the infiltrated layer and the scaffold may be affected by mismatched TEC and chemical reactions [115-117]. These drawbacks could lead to delamination and performance degradation, reducing activity and stability during long-term operation. Excessive infiltration can also decrease active sites and porosity, hindering reaction rates and mass transfer [118]. Thus, while beneficial, this method still has limitations requiring further optimization.

(2) Exsolution engineering

Exsolution is a technique for growing nanoparticles (NPs) on perovskite substrates, enhancing catalytic activity through improved surface and interface properties. The NPs are strongly anchored, resisting agglomeration, coking, and sulfur poisoning for stable operation. However, exsolution mainly occurs in reducing atmospheres, with NPs potentially re-dissolving in oxidizing conditions, such as air electrodes at high temperatures. Therefore, research aims to develop stable NPs for humid air environments.

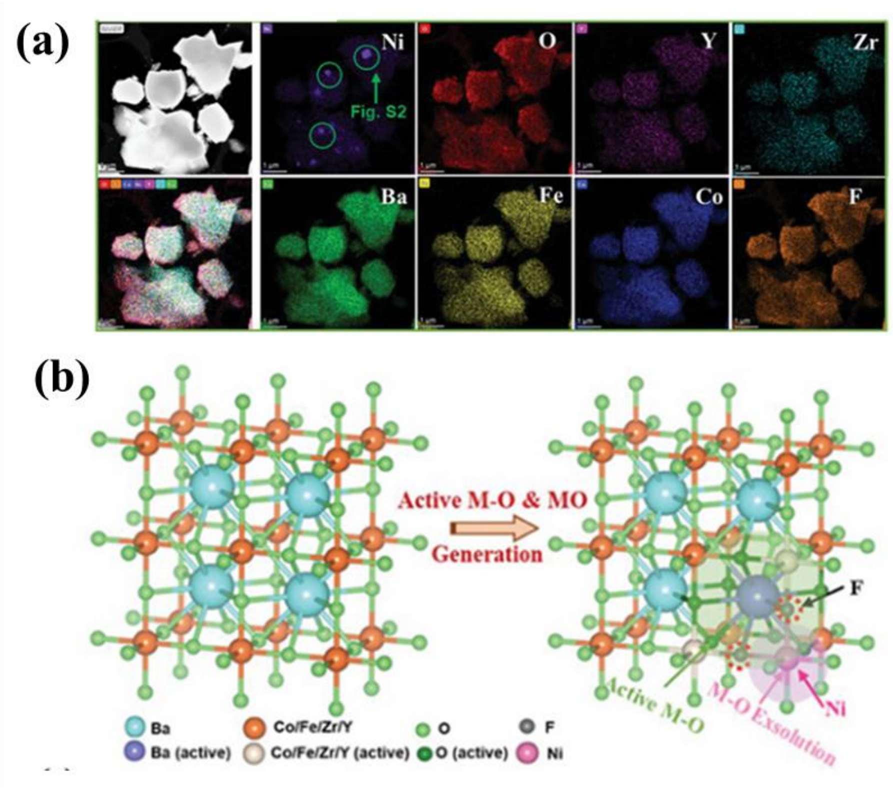

Figure 2. 7 (a) EDX mapping results. (b)Active metal-oxygen bond and NiO for N-BCFZYNF composite electrode [90].

Utilizing H_2O as a mediator to induce the in-situ formation of active catalytic nanoparticles has demonstrated significant potential for enhancing electrochemical performance. For example, when exposed to humid air, H_2O facilitates the segregation of Ba ions from the $PrBa_{0.8}Ca_{0.2}Co_2O_{5+\delta}$ parent material, which then undergoes topotactic cation exchange with Co ions, resulting in the in-situ exsolution of $BaCoO_{3-\delta}$ catalysts that coat the PBCC bulk surface [119-120]. This process significantly enhances oxygen surface exchange kinetics.

Additionally, research by Ni et al. indicates that anion doping can also facilitate the dissolution of B-site metal oxides [90]. For example, introducing 10% F^{-} ions into the perovskite oxide, nominally formulated as $Ba(Co_{0.4}Fe_{0.4}Zr_{0.1}Y_{0.1})_{0.95}Ni_{0.01}F_{0.1}O_{2.9-\delta}$ (BCFZYNF), results in the precipitation of a 1.0% NiO phase on the surface of the cubic perovskite, forming a composite material (N-BCFZYNF) [90] (**Figure 2.7a**). The formation of NiO nanoparticles is attributed to the low eutectic energy of Ni ions and the weakened metal-oxygen bonds in the lattice. The weakened metal-oxygen bonds and the generation of surface metal oxide nanocatalysts significantly improves the rate of oxygen adsorption/desorption (**Figure 2.7b**).

(2) Core-shell engineering

The core-shell structure, which involves covering the core material with an additional phase as the shell, plays a crucial role in regulating the surface properties of air electrodes. By introducing a shell structure on the electrode surface as a nanocatalyst or protective layer, the reactive surface area of porous microstructured air electrode materials (core) significantly increases, thereby enhancing their stability in H_2O, CO_2, and Cr-containing atmospheres[121]. Furthermore, when shell nanoparticles with superior mixed ionic/electronic conductivity form a continuous charge transport pathway in appropriate quantities, the electronic and ionic conductivity of the nanocomposite electrode markedly improves. This heterojunction structure also facilitates grain refinement, preventing the excessive agglomeration of internal nanometal particles during high-temperature sintering [122]. These beneficial effects drive the development of nanocomposite air electrodes with high electrocatalytic activity and stability.

2.3.3 Phase Regulation

For RePCC air electrode materials, it is often difficult for single-phase materials to achieve the diverse properties necessary for efficient ORR/WOR. As a result, phase-controlling strategies have been developed. Different phases contribute specific properties, addressing various electrochemical reaction needs, and enabling the development of high-performance air electrodes. Phase regulation strategies can be categorized into mechanical mixing methods and self-assembly methods (or phase segregation methods) based on the preparation techniques.

(1) Mechanical mixing

The thermal mismatch between single-phase MIEC and proton-conducting electrolytes is a significant challenge. However, mechanically mixing MIEC with proton-conducting materials to form composite electrodes effectively alleviates this issue. Moreover, compared to single-phase air electrodes, composite electrodes exhibit a substantial expansion of active sites, which facilitates the charge transfer process[123-124].

Additionally, triple-conducting air electrodes can be synthesized by combining different perovskite oxides. For instance, a composite oxide prepared by mechanically mixing $Sm_{0.5}Sr_{0.5}CoO_{3-\delta}$ (SSC) and $SmBaCo_2O_{5+\delta}$ (SBC) demonstrates enhanced oxygen reduction capabilities and structural robustness [125].

However, most composite materials prepared via physical mixing methods exhibit several drawbacks, such as inhomogeneity, micro-scale phases, high thermal expansion coefficients, undesired chemical interactions between phases, and limited interfacial contact area. These issues significantly reduce the activity of air electrodes.

(2) Self-assembly

Composite electrodes with self-assembled nanoparticles are typically synthesized using a simple one-pot method. The different phases are nanoscopically mixed, exhibiting synergistic interactions and uniform distribution, which significantly expand the heterointerfaces and result in enhanced electrode activity and durability [126].

For instance, $BaCo_{0.7}(Ce_{0.8}Y_{0.2})_{0.3}O_{3-\delta}$ (BCCY) spontaneously reconstructs into a Ce-rich proton/electron-conducting phase (P-BCCY) and a Co-rich oxygen ion/electron-conducting phase (M-BCCY) after one-pot sintering [80]. This nanocomposite material demonstrates excellent triple-conducting properties, with proton and O^{2-} ion conductivities ranging from 0.07 to 0.10 S cm^{-1} and 0.01 to 0.03 S cm^{-1}, respectively, at operating temperatures of 525 °C to 650 °C.

2.3.4 Microstructure Regulation

In addition to regulating the specific composition (such as elemental composition, surface composition, and phase composition) of air electrode materials to alter their physicochemical properties, precise control of their microstructure is also a crucial approach for further performance enhancement. Specifically, the microstructure of air electrodes significantly influences their catalytic performance through porosity and pore size distribution, thickness, and particle size.

Thin-film air electrode layers fabricated using electrostatic spray deposition (ESD), pulsed laser deposition (PLD), and atomic layer deposition (ALD) exhibit smaller particle sizes and higher porosity than those produced by the sol-gel method. These features significantly enhance ion transport and gas diffusion, thereby increasing electrode ion conductivity and power output.

Using ESD technology, one-dimensional air electrode fibers composed of $La_{0.6}Sr_{0.4}Co_{0.2}Fe_{0.8}O_{3-\delta}$ (LSCF)-$BaCe_{0.5}Zr_{0.35}Y_{0.15}O_{3-\delta}$ (BZCY) were successfully synthesized [127] (**Figure 2.8a**). These highly porous electrodes, characterized by continuous fiber microstructures and well-developed perovskite structures with diameters ranging from 90 to 150 nm (**Figures 2.8b-c**), effectively promote gas diffusion and charge transfer processes.

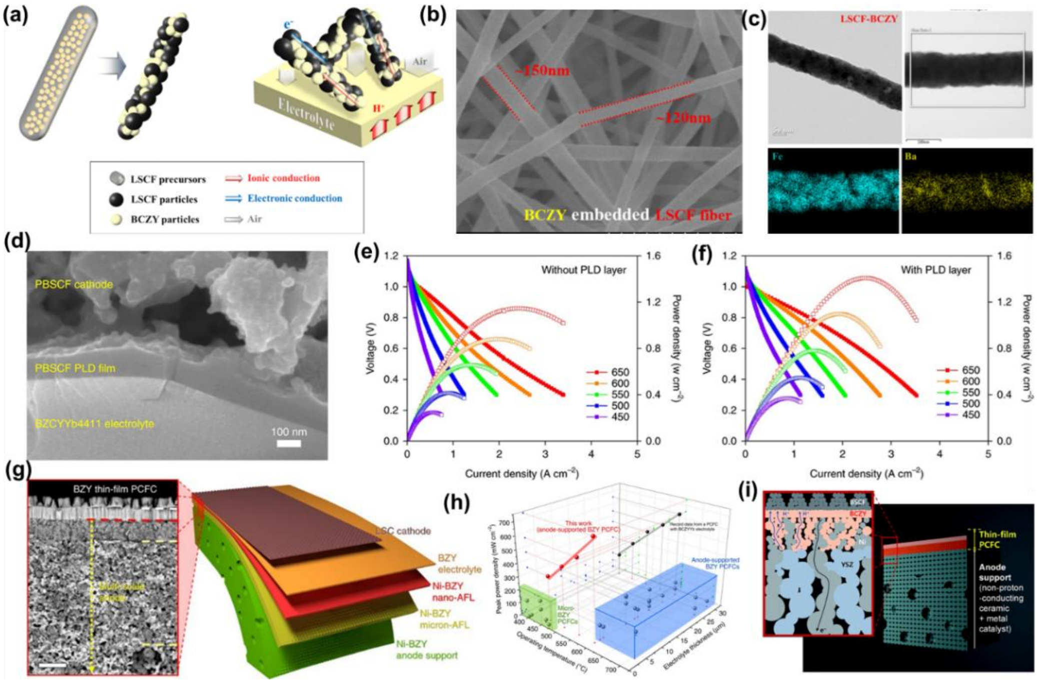

Figure 2. 8 (a) Schematic microstructures of BCZY particles embedded LSCF fiber; (b) SEM and (c) TEM images and element distribution of LSCF-BCZY composite electrode prepared by ESD[128]. (d) PCFC with ultra-thin PBSCF prepared by PLD. I-V-P curves of a representative cell (e) without and (f) with a PLD layer[58]. (g) SEM and schematic diagram of the overall microstructure of PCFC with LSC-coated composite electrode prepared by PLD technique. (h) Performance comparison. (i) Schematics of a thin-film PCFC with a non-proton-conducting matrix phase[129].

PLD is also widely employed to enhance the surface structure of air electrodes. For example, a dense interlayer between the air electrode and the electrolyte is prepared using PLD [58] (**Figure 2.8d**). This approach significantly reduces the contact resistance caused by electrode-electrolyte mismatch, achieving a peak power density (PPD) exceeding 800 mW cm^{-2} at 600 °C (**Figures 2.8e-f**). Another instance involves incorporating a $La_{0.6}Sr_{0.4}CoO_{3-\delta}$ (LSC) air electrode into the dense electrolyte layer using PLD technology (**Figures 2.8g-i**) [129].

ALD, known for its atomic-level control over film thickness, ability to form sub-nanometer films, and capability to achieve uniform coatings on complex surfaces, is particularly well-suited for ceramic cell electrodes[130-131]. For instance, ALD is used to uniformly deposit high-performance CoO_x active materials onto the surface of porous PBSCF materials, fabricating composite air electrodes to maximize surface activity [132]. Moreover, the coating of nanoparticles enhances the stability of composite electrodes by suppressing secondary phase formation caused by Ba or Sr aggregation and by preventing deformation through the electrostatic attraction between oxygen vacancies and cations.

CHAPTER 3 Methodology

3.1 Chemical Reagents

The specifications and models of the reagents are listed in **Table 3. 1**.

Table 3. 1 Reagents used in the experiments.

Reagent name	Chemical formula	Purity	Manufacturer
Strontium nitrate	$Sr(NO_3)_2$	AR, 99.5%	Aladdin
Ferric nitrate	$Fe(NO_3)_3·9H_2O$	AR, 99.5%	Aladdin
Nickel nitrate	$Ni(NO_3)_2·6H_2O$	AR, 99.5%	Macklin
Barium acetate	$C_4H_6O_4·Ba$	AR, 99.5%	Macklin
Niobium oxalate hydrate	$C_{10}H_5NbO_{20}$	AR,99%	Macklin
Zirconium nitrate	$Zr(NO_3)_4·5H_2O$	AR, 99.5%	Macklin
Cerium nitrate	$Ce(NO_3)_4·5H_2O$	AR, 99.5%	Macklin
Yttrium nitrate	$Y(NO_3)_3·6H_2O$	AR, 99.5%	Macklin
Ytterbium nitrate	$Yb(NO_3)_3·6H_2O$	AR, 99.5%	Macklin
Citric acid	$C_6H_8O_7$	AR, 99.5%	Macklin
Ethylenediaminetetraacetic acid (EDTA)	$C_{10}H_{16}N_2O_8$	AR, 99.5%	Macklin
Ammonium hydroxide	$NH_3·H_2O$	AR, 26-28%	Macklin
Soluble starch	$(C_6H_{10}O_5)_n$	AR	Macklin
Nitric acid	HNO_3	AR	Macklin
Isopropanol	C_3H_8O	AR	Macklin
Ethylene glycol	$C_2H_6O_2$	AR	Macklin
Glycerol	$C_3H_8O_3$	AR	Macklin

Silver conductive slurry	/	/	Shanghai Synthetic Resin Research Institute

3.2 Powder Synthesis

In this study, the air electrode materials and BZCYYb electrolyte materials are prepared using the sol-gel method. The detailed process for preparing the powder via the sol-gel method is exemplified using BZCYYb. First, stoichiometric amounts of barium acetate, $Zr(NO_3)_4 \cdot 5H_2O$, $Ce(NO_3)_3 \cdot 6H_2O$, $Y(NO_3)_3 \cdot 6H_2O$, and $Yb(NO_3)_3 \cdot 5H_2O$ are weighed and dissolved in deionized water. Subsequently, EDTA and citric acid are added to the solution in a mass ratio of $m_{\text{metal ions}}$: m_{EDTA}: $m_{\text{citric acid}}$ = 1:1:1.5. The mixture is stirred until dissolved, and then ammonia solution is added to adjust the pH to 7-8. The solution is then heated and stirred on a magnetic stirring hot plate at 180 °C until it becomes gel-like. The gel is placed in an oven and maintained at 180 °C for 12 hours to obtain a black, fluffy precursor powder. The precursor powder is then calcined at 1100 °C for 5 hours to obtain the BZCYYb electrolyte powder.

3.3 Cell Fabrication

3.3.1 Preparation of Air Electrode Slurry

1 gram of air electrode powder, 10 mL of isopropanol, 2 mL of ethylene glycol, and 0.6 mL of glycerol are thoroughly mixed by high-speed ball milling for 1 hour. The resulting mixture forms the air electrode slurry.

3.3.2 Preparation of Symmetrical Cells

In this study, the structure of symmetrical cells is air electrode | BZCYYb | air electrode. Dense BZCYYb electrolyte discs are prepared first. 0.35 g of BZCYYb powder is weighed and pressed into discs using a 13 mm diameter mold. The BZCYYb discs are then calcined in a muffle furnace at 1400 °C for 5 hours. Later, the prepared electrode slurry is uniformly sprayed on both sides of the electrolyte discs and calcined at the appropriate temperature.

3.3.3 Preparation of Single Cells

In this study, all single cells are Ni-BZCYYb fuel electrode-supported cells with the configuration of Ni-BZCYYb|BZCYYb|air electrode. Firstly, the Ni-BZCYYb|BZCYYb half-cell is prepared. NiO powder, BZCYYb powder, and corn starch are mixed in a planetary ball mill for 1 hour at a mass ratio of m_{NiO}:m_{BZCYb}:$m_{corn\ starch}$ = 13:7:2, where corn starch acts as a pore-forming agent. Later, 0.35 g of the mixed powder is weighed and pressed into NiO-BZCYYb discs using a mold under a pressure of 150 MPa. Subsequently, 0.015 g of BZCYYb powder is weighed and evenly spread using a 200-mesh sieve, which is pressed at 300 MPa to prepare NiO-BZCYYb/BZCYYb green disks. These green disks are subsequently calcined in a high-temperature furnace at 1400 °C for 5 hours to obtain dense NiO-BZCYYb/BZCYYb half-cells. The air electrode slurry is sprayed onto the BZCYYb side of the half-cell and then calcined in a high-temperature furnace to obtain the required single cells. During the experiments, the single cell is mounted on a homemade cell mold, and both electrodes are separately connected with silver wires to an electrochemical workstation for performance testing.

3.4 Performance Characterization Methods

3.4.1 Microstructural Composition of Materials

The phase structure of the samples is analyzed using an X-ray diffractometer (XRD, Rigaku SmartLab 9kW). The measurements are conducted with Cu-Kα radiation, at a working voltage of 40 kV and a current of 40 mA. The scanning range is from 10° to 80°, with a step size of 0.02°. XRD refinement data are obtained using the FullProf software. The microstructure of the samples is observed using a scanning electron microscope (SEM, Tescan MIRA). Before testing, the samples are gold-coated for 90 seconds to improve conductivity. Transmission electron microscopy (TEM, FEI Talos F200x) is used to acquire low- and high-magnification images of the samples, providing detailed information on their microstructure and lattice fringes.

3.4.2 Elemental Composition of Materials

Elemental distribution on the sample surfaces is analyzed using a scanning transmission electron microscope equipped with energy-dispersive X-ray spectroscopy (STEM-EDX, FEI Talos F200x). Quantitative analysis of the elemental composition is conducted using inductively coupled plasma optical emission spectrometry (ICP-OES, Thermo Scientific iCAP 7600). For ICP-OES analysis, 0.1 g of the powdered sample is dissolved in 5 mol L^{-1} nitric acid. The solution is then transferred to a volumetric flask and diluted to a specific volume. Standard solutions containing the elements of interest are used to create calibration curves. The sample solution is measured three times, and the ion concentrations are determined based on the calibration curves. The average value of the three measurements is reported as the ion concentration.

3.4.3 Surface Elemental Valence States

The surface elemental valence states of the samples are analyzed using X-ray photoelectron spectroscopy (XPS, Thermo Fisher Scientific Nexsa). The measurements are performed with Al Kα radiation, and the peak positions are calibrated using the C 1s standard binding energy (284.8 eV). Data fitting is carried out using the Avantage software. The electronic structure of Fe is examined using soft X-ray absorption spectroscopy (XAS), with an energy resolution of 1.2 eV. The Fe metal foil is used for calibration. The EXAFS measurement range spans from 7146 to 7610 eV.

3.4.4 Thermochemical Properties

The TEC of the electrode samples is obtained using a dilatometer (DIL 402CL, Netzsch). The samples are first prepared into bar-shaped specimens. A 0.7 g sample of powder is weighed and pressed into bar-shaped green bodies using a mold. These are then calcined at 1200 °C for 5 h to obtain dense bar-shaped samples. After calcination, the sample dimensions are 5 mm×2 mm×15 mm. Thermal expansion tests are typically conducted in air, with a temperature range from room temperature to 1000 °C, and a heating rate of 10 °C min^{-1}.

3.4.5 Hydration Properties

The hydration properties of the samples are analyzed using Fourier-transform infrared spectroscopy (FT-IR, Thermo Scientific Nicolet iS5). Samples are first treated in humid air for some time and then dried in an oven at 100 °C for 5 hours to remove physically adsorbed water from the sample surfaces. During the test, the wavelength scan range is set from 1500 to 4000 cm^{-1}.

3.4.6 Oxygen Non-Stoichiometry

The oxygen non-stoichiometry of the material at room temperature is determined using iodometric titration. A 0.1 g powder sample is completely dissolved in concentrated HCl solution (6 mol·L^{-1}) with an excess of KI powder. The resulting solution is then diluted with water to maintain a slightly acidic pH (pH=6). The solution is titrated twice with a fresh $Na_2S_2O_3$ standard solution (0.05 mol·L^{-1}). Near the endpoint of the titration, a fresh starch indicator is added to indicate the endpoint. The average volume of $Na_2S_2O_3$ solution consumed in the two titrations is used to determine the valence state of Fe and the concentration of oxygen vacancies.

Thermogravimetric analysis (TG, TGA5500) is used to measure the mass loss of the sample during the heating process and calculate the oxygen non-stoichiometry of the material. The temperature range for the test is from room temperature to 1000 °C, with a heating rate of 10 °C min^{-1}.

3.4.7 Oxygen Desorption Properties

Oxygen temperature-programmed desorption (O_2-TPD) analysis is performed using a temperature-programmed chemisorption analyzer (Xianquan 5080B). The sample is initially pretreated at 200 °C in a He atmosphere for 1 hour to remove moisture, followed by cooling to 50 °C. Subsequently, a 10% O_2/He gas mixture is introduced for 1 hour to ensure sufficient oxygen adsorption on the sample. Afterward, He gas is purged for 1 hour to remove physically adsorbed oxygen from the surface. Finally, the sample is heated from 50 °C to 900 °C at a rate of 10 °C min^{-1} under a He atmosphere, and the desorbed gases are detected using a thermal conductivity detector (TCD, Xianquan 5080B).

3.4.8 Conductivity Testing

Bar samples are prepared following the same procedure as for the thermal expansion tests. Mounted on homemade fixtures, the conductivity of the dense bar samples is measured using the DC four-probe method, with fixed silver wires serving as current collectors. A constant current of 100 mA is applied to the sample, and the voltage is recorded using a digital source meter (Keithley 2440). The test atmosphere is flowing air or mixed gas of N_2 and O_2 with a gas flow rate of 100 mL·min^{-1}. The conductivity of the material is calculated using Equation 3.1:

$$\sigma = \frac{1}{\rho} = \frac{I}{U}\frac{l_2}{l_1 l_3} \tag{3.1}$$

Where ρ is the resistivity, Ω·m, I, and U are the output current signal, A; U is the output voltage signals in A and V, respectively, and l_2, l_1, and l_3 are the length, width, and thickness of the bar sample in cm.

3.4.9 Electrical Conductivity Relaxation Testing

Electrical conductivity relaxation (ECR) tests are performed using bar samples to obtain the bulk oxygen diffusion coefficient (D_{chem}) and surface oxygen exchange coefficient (k_{chem}) of the samples. During testing, a constant current of 100 mA is applied to the samples using a digital source meter (Keithley 2460), and the voltage response is recorded.

Initially, the samples are placed in an atmosphere of 21 vol.% O_2-79 vol.% N_2 with a gas flow rate of 100 mL min^{-1}. Once the voltage output signal of the samples stabilizes, the atmosphere is switched to 10 vol.% O_2-90 vol.% N_2 while maintaining the total gas flow rate at 100 mL min^{-1}. The corresponding relaxation curve is recorded until the curve reaches equilibrium. The conductivity of the sample during the relaxation process is then calculated using Equation 3.1, and the result is converted to normalized conductivity using Equation 3.2:

$$g(t) = \frac{\sigma_t - \sigma_0}{\sigma_\infty - \sigma_0} \tag{3.2}$$

$$= 1 - \sum_{n=1}^{\infty}\sum_{m=1}^{\infty}\sum_{p=1}^{\infty} \frac{2C_1^2 \exp\left(-\alpha_{1n}^2 D_{chem} \frac{t}{l_1^2}\right)}{\alpha_{1n}^2(\alpha_{1n}^2 + C_1^2 + C_1)} \cdot \frac{2C_2^2 \exp\left(-\alpha_{2m}^2 D_{chem} \frac{t}{l_2^2}\right)}{\alpha_{2m}^2(\alpha_{2m}^2 + C_2^2 + C_2)} \cdot \frac{2C_3^2 \exp\left(-\alpha_{3p}^2 D_{chem} \frac{t}{l_3^2}\right)}{\alpha_{3p}^2(\alpha_{3p}^2 + C_3^2 + C_3)}$$

Where σ_0, σ_t, and σ_∞ represent the conductivity at t=0, t=t, and t=∞ in S cm^{-1}. D_{chem} represents the chemical bulk diffusion coefficient of the material (cm^2 s^{-1}), while α_{1n}, α_{2m} , α_{3p} denote the nth, mth, and pth roots of the transcendental equation, respectively. Further details of the fitting procedure can be found in the literature [133-134]. In this study, the relaxation curves were fitted using the ECRTOOLS tool developed by Prof. Ciucci et al.[135].

3.4.10 Electrochemical Performance Testing

The electrochemical impedance spectra (EIS) of the symmetrical cells are measured using a homemade symmetrical cell test mold. The EIS measurements are conducted with an electrochemical workstation (Solartron 1287+1260) over a frequency range of 10^5 Hz to 10^{-1} Hz with a signal amplitude of 30 mV. Subsequently, the distribution of relaxation times (DRT) method is used to analyze the EIS results to obtain information on the electrode reaction sub-steps.

For single cells, the i-V-p curves and constant voltage tests are conducted using a homemade single-cell test mold, and data are recorded with a digital source meter (Keithley 2440). The single cell is supplied with 50 mL min^{-1} of H_2 as fuel and 100 mL min^{-1} of synthetic air as the oxidant. Water vapor is introduced via a water bath heating method.

3.5 Computational Details

The first-principles computations were conducted within the framework of DFT using VASP [136-137]. The exchange-correlation interaction was treated employing a generalized gradient approximation (GGA) as described by the Perdew-Burke-Ernzerhof (PBE) function [138]. The kinetic energy cutoff of the plane wave utilized to extend the Kohn-Sham electron wave function was set to 400 eV, with the iterative convergence of energy being 10^{-5} eV. All atomic positions were allowed to relax until the Hellmann-Feynman force fell below 0.01 eV Å^{-1}. The Brillouin zone was sampled by a 2× 2× 2 k-point grid.

ORR proceeds through a four-electron mechanism [139-140]:

$$* + O_2 + H^+ + e^- \rightarrow * OOH \tag{3.3}$$

$$* OOH + H^+ + e^- \rightarrow * O + H_2O \tag{3.4}$$

$$* O + H^+ + e^- \rightarrow * OH \tag{3.5}$$

$$* OH + H^+ + e^- \rightarrow H_2O \tag{3.6}$$

The Gibbs free energy (ΔG) change for ORR/WOR intermediates was determined using the Equation 3.7 [141]:

$$\Delta G = \Delta E + \Delta ZPE + T\Delta S - eU \tag{3.7}$$

Here, ΔE represents the energy change in each step, ΔZPE is the change in the zero-point energy calculated from vibrational frequencies, ΔS is the entropy change based on thermodynamics databases, and T denotes the room temperature of 298.15 K. $-eU$ is the standard electrochemical potential of the electron involved in the reaction, obtained when the electrode potential is referenced to the reversible hydrogen electrode. Simultaneously, the standard electrochemical potential of the proton (G_{H_2}) is set to be equivalent to that of a hydrogen atom in gaseous H_2 ($\frac{1}{2}G_{H_2}$). Owing to limitations in characterizing the triplet state of the O_2 molecule within the present DFT framework, the free energy of the O_2 molecule was determined by the following equation [142]:

$$G_{O_2} = 2G_{H_2O} - 2G_{H_2} + 4.92 \tag{3.8}$$

Corrected free energy values were computed using a plugin for VASP, named VASPKIT. To quantitatively assess the stability of the perovskite lattice, the formation energy of the Ruddlesden-Popper layered perovskite Dx-SFN crystal structure was calculated using the formula below [143-144]:

$$3SrO + Fe_2O_3 + 0.5O_2 \leftrightarrow Sr_3Fe_2O_7 \tag{3.9}$$

$$3SrO + 0.9Fe_2O_3 + 0.1Nb_2O_5 + 0.4O_2 \leftrightarrow Sr_3Fe_{1.8}Nb_{0.2}O_7 \tag{3.10}$$

$$2.8SrO + 0.9Fe_2O_3 + 0.1Nb_2O_5 + 0.5O_2 \leftrightarrow Sr_{2.8}Fe_{1.8}Nb_{0.2}O_7 \tag{3.11}$$

The formation energy is determined by subtracting the energy of the reactants on the left-hand side from the energy of the products on the right-hand side of the equation. The more negative the formation energy, the higher the stability of the perovskite.

CHAPTER 4 Engineering Synergistic Oxygen-Proton Properties for High-Performance Reversible Protonic Ceramic Cell Air Electrodes

4.1 Introduction

Reversible protonic ceramic cells (RePCCs) typically operate at low to intermediate temperatures (400–650 °C) [5, 56], making them more compatible with renewable energy sources in a broader range of applications compared to traditional high-temperature (700–1000 °C) solid oxide cells (SOCs). Additionally, low-temperature operation enhances system stability, reduces system costs and complexity, and allows for the utilization or production of dry, pure fuel gases, thereby lowering product handling costs [145].

Despite their significant potential, operating RePCCs at low to intermediate temperatures can negatively affect the kinetics of ORR/WOR at the air electrode due to the high energy barriers associated with O=O bond breaking and O^{2-} transfer [9]. Furthermore, compared to SOCs, RePCCs impose higher requirements on the performance of air electrode materials. These include high oxygen surface exchange capacity, sufficient $e^-/H^+/O^{2-}$ triple conductivity, excellent durability and moisture resistance, and high ORR/WOR activity. Therefore, the development of air electrodes with superior performance and stability is crucial for the practical application of RePCCs. Ruddlesden-Popper perovskite materials (RP perovskites), with the general formula $A_{n+1}B_nO_{3n+1}$ (n=1, 2, 3, ...), are considered ideal materials for RePCC air electrodes due to their excellent oxygen transport properties, tunable structures, and adjustable physicochemical characteristics [13, 59, 146-147].

Traditional mixed oxygen ion-electron conductors used as candidate materials for RePCC air electrodes often exhibit insufficient proton conductivity [28, 66]. However, $Sr_3Fe_2O_{7-\delta}$ (SF)-based RP materials contain abundant oxygen vacancies that facilitate hydration reactions and the formation of proton defects, thereby enhancing proton conductivity [13]. Oxygen vacancies not only serve as active sites for water adsorption/dissociation but also act as sites for surface oxygen adsorption and dissociation and carriers for bulk oxygen ion transport. Consequently, there is a competitive relationship between hydration reactions and ORR/WOR processes in these materials.

Excessive hydration caused by abundant oxygen vacancies can reduce the oxygen surface exchange capacity of the electrodes. For instance, Chen et al. reported that an excessive oxygen vacancies can lead to excessive water adsorption competition, thereby negatively affecting ORR performance [148]. Additionally, Shao et al. demonstrated that a high oxygen vacancy concentration is unfavorable for proton transport, as proton migration in the bulk occurs via hopping between adjacent lattice oxygen sites [149]. On the other hand, a low oxygen vacancy concentration hinders both the oxygen surface exchange and bulk diffusion properties of the electrode. Thus, an optimized oxygen vacancy concentration is expected to enhance both the hydration/proton transport properties and the ORR/WOR rates of the material.

Previous studies have shown that hydration performance can be regulated by adjusting the water vapor concentration in the atmosphere to optimize electrode performance [7]. This study proposes balancing oxygen-proton competition by tuning the strength of the B-site metal-oxygen bond and the oxygen vacancy concentration. A strategy involving substitution with high-valence Nb ions was employed to modulate the oxygen vacancy concentration and hydration properties of Fe-based high-dimensional RP perovskite SF materials, thereby coordinating the oxygen- and proton-related properties of the material.

To investigate the effects of varying oxygen vacancy concentrations on the ORR, WOR, and hydration reactions at the air electrode, three candidate materials with different Nb doping levels ($Sr_3Fe_{2-x}Nb_xO_{7-\delta}$, abbreviated as SFNbx, x=0, 0.1, 0.2) were synthesized. Through a comprehensive analysis of the physicochemical and electrochemical properties of these materials, the mechanisms balancing ORR/WOR and hydration reactions in SFNbx materials were explored. By optimizing the hydration/proton transport properties and oxygen exchange/transport characteristics, enhanced electrocatalytic activity and long-term stability under operating conditions were achieved.

4.2 Material Synthesis

SFNbx (x=0, 0.1, and 0.2) is prepared by the sol-gel method. Stoichiometric amounts of strontium nitrate, ferric nitrate, and niobium oxalate are weighed and dissolved in deionized water. Citric acid and EDTA are added as complexing agents and fuels in a molar ratio of 1.5:1:1 with the metal ions. Ammonia water is used to adjust the solution pH to 7-8. The solution is then heated to reduce the solvent and form a gel, which is subsequently transferred to an oven at 180 °C to obtain the precursor. The collected powder is calcined at 1100 °C for 10 hours to obtain the initial SFNbx powders.

4.3 Microstructure and Composition of the Material

As shown in **Figure 4.1a**, the SFNbx powders prepared via the sol-gel method exhibit the RP phase structure of $Sr_3Fe_2O_{6.74}$ (PDF#01-082-0428), indicating good phase formation. Further XRD analysis in the range of 31.3–33.3° (**Figure 4.1b**) reveals that the main peak shifts to lower angles with the introduction of Nb, suggesting lattice expansion due to Nb doping. **Figure 4.1c** illustrates the crystal structure of the Nb-doped $Sr_3Fe_2O_{7-\delta}$ material.

To obtain more detailed information on the phase structure, the XRD spectra of the three materials are refined, and the refined results are presented in **Figures 4.1d–f** and **Table 4.1**. The introduction of Nb increases the lattice parameters, leading to an expansion of the unit cell volume from 0.301 nm^3 for SF to 0.304 nm^3 for SFNb0.1, and further to 0.306 nm^3 for SFNb0.2, consistent with the results shown in **Figure 4.1b**. Considering that the ionic radius of Nb^{5+} (0.64 Å) is comparable to that of Fe^{3+} (0.645 Å) but significantly larger than that of Fe^{4+} (0.585 Å), the increase in unit cell volume with higher Nb content is likely due to the partial reduction of Fe^{4+} to Fe^{3+} ions.

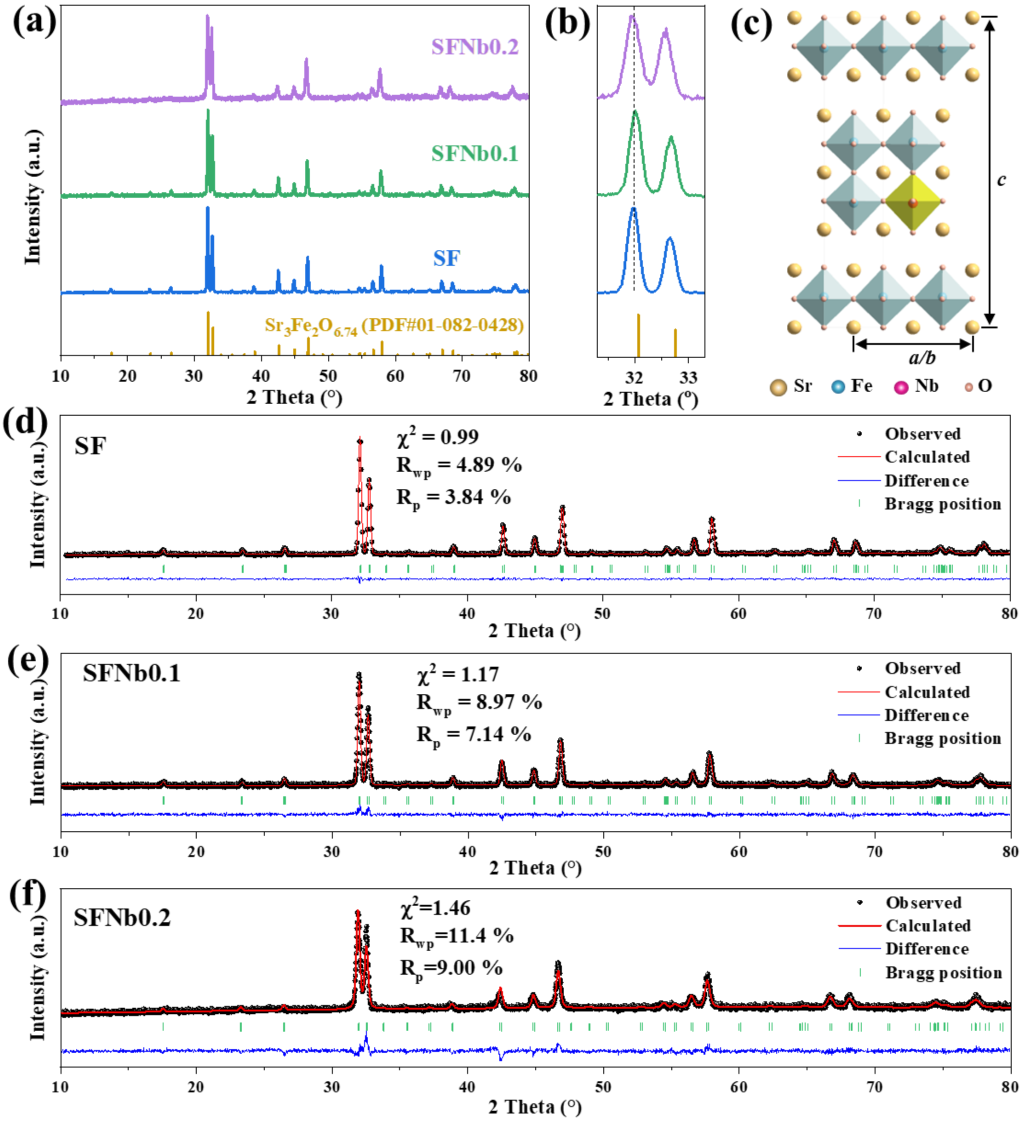

Figure 4. 1 Phase structure of SFNbx. (a) XRD patterns of the fresh samples. (b) Local magnification of XRD. (c) Structural schematic diagram of SFNb0.1. (d-f) XRD refinement results.

Table 4. 1 Results of the refined XRD patterns.

Lattice parameter	SF	SFNb0.1	SFNb0.2
a (Å)	3.86587	3.87972	3.89263
b (Å)	3.86587	3.87972	3.89263
c (Å)	20.15923	20.20369	20.21467
Space group	I4/mmm	I4/mmm	I4/mmm
Volume (nm^3)	0.30128	0.30411	0.30630
Crystallite size (nm)	33.02	29.29	23.74

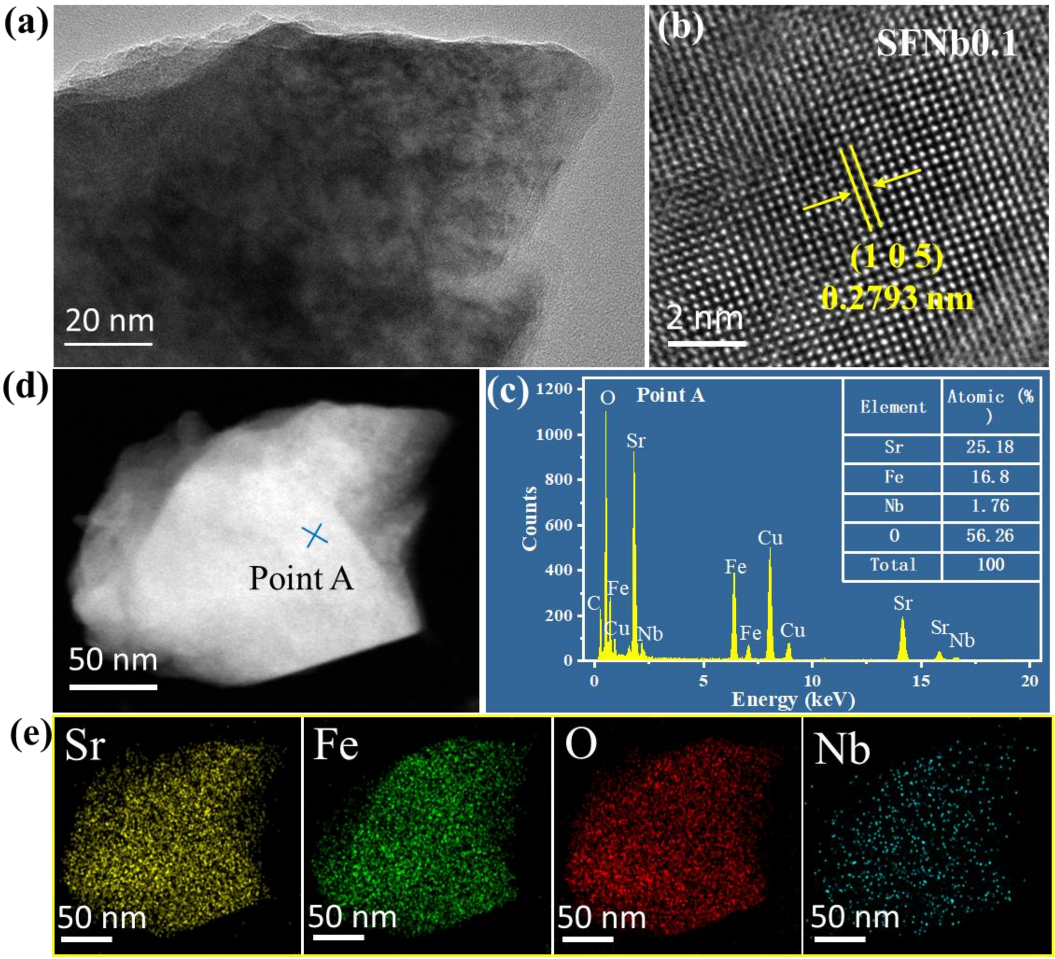

Figure 4. 2 Morphology of SFNb0.1. (a) TEM of SFNb0.1, (b) HRTEM lattice fringes of SFNb0.1, (c) EDX of SFNb0.1, (d-e) HADDF-EDX mapping.

The micromorphology of the SFNb0.1 material is analyzed using TEM, as shown in **Figure 4.2**. The HRTEM images reveal lattice fringes corresponding to the (105) crystal plane of SFNb0.1 (**Figure 4.2b**). **Figure 4.2c** presents the EDX results of the SFNb0.1 powder, showing elemental proportions of Sr, Fe, Nb, and O at 25.2%, 16.8%, 1.8%, and 56.2%, respectively, which are closely aligned with the nominal ratios. **Figures 4.2d–e** display the HAADF-EDX elemental mapping results of SFNb0.1, indicating a uniform distribution of Sr, Fe, Nb, and O elements within the 200 nm-sized SFNb0.1 particles.

4.4 Mechanism of Balancing Oxygen-Proton Related Properties

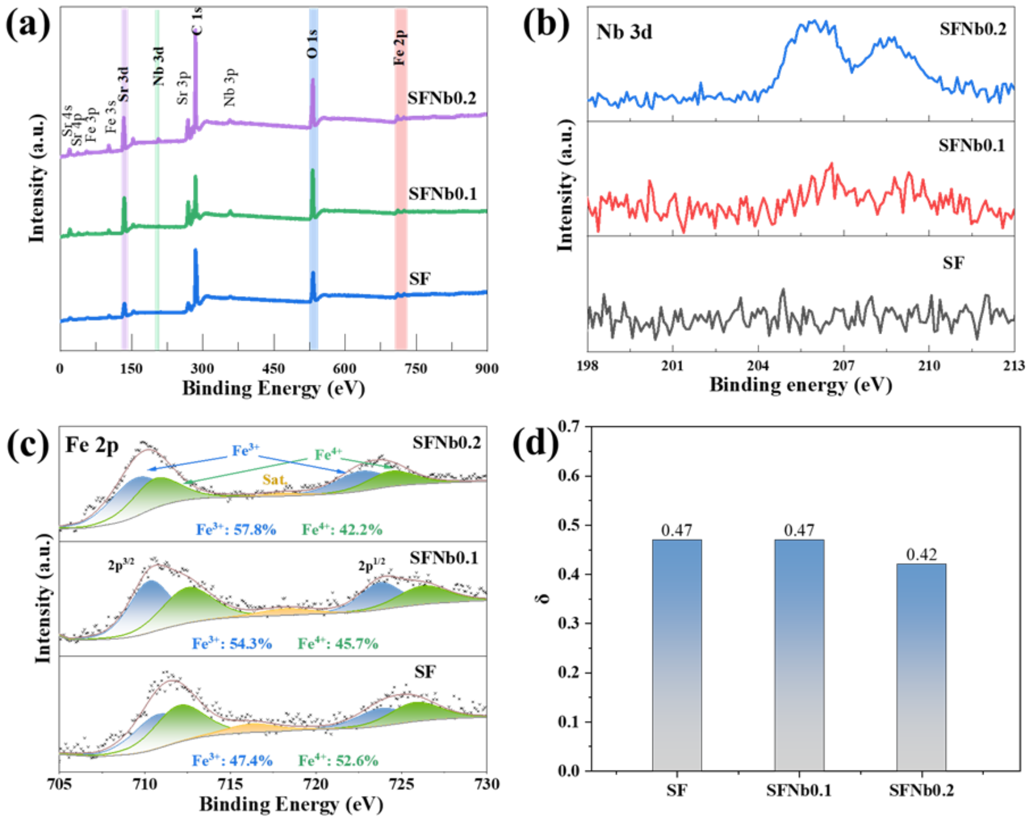

Figure 4. 3 Surface information of SFNbx materials. (a) XPS sum spectra. (b) Nb 3d spectra. (c) Fe 2p XPS spectra. (d) Surface oxygen vacancy calculated by the XPS fitting results.

The surface properties of materials significantly influence the activity of electrode reactions. In this study, the surface element composition and chemical valence states of fresh samples with varying Nb doping levels were analyzed using XPS, and the survey spectra are shown in **Figure 4.3a**. **Figure 4.3b** presents the XPS spectra of Nb 3d, where the intensity of the Nb 3d peaks increases progressively with higher Nb doping levels. **Figure 4.3c** illustrates the Fe 2p spectra of the SFNbx materials, in which the peaks of Fe^{3+} appear at 710.1 eV and 723.6 eV, while those of Fe^{4+} are located at 712.1 eV and 725.9 eV. With increasing Nb^{5+} doping levels, the content of Fe^{3+} continuously increases, whereas the content of Fe^{4+} decreases.

The oxygen non-stoichiometry (δ) of the material surface, calculated based on the average valence state of the B-site metal elements, is determined to be 0.47 for SF, 0.47 for SFNb0.1, and 0.42 for SFNb0.2 (**Figure 4.3d**). These results indicate that low Nb doping (SFNb0.1) does not alter the surface oxygen vacancy concentration, and the valence compensation of the material is primarily achieved by reducing the valence state of B-site Fe ions. In contrast, at higher Nb doping levels (SFNb0.2), the electrical neutrality of the material is maintained by lowering the average chemical valence of Fe and partially sacrificing oxygen vacancies.

To investigate the bulk oxygen vacancy content of the materials, iodometric titration tests are conducted on three samples. The detailed procedure is described in the experimental section. With the introduction of Nb, the bulk oxygen vacancy content decreases progressively, with values of 0.51, 0.49, and 0.46 for SF, SFNb0.1, and SFNb0.2, respectively.

Thermogravimetric (TG) analysis is performed to study the weight loss of the three materials from room temperature to 900 °C, as shown in **Figure 4.4a**. With increasing temperature, the weight loss of all samples increases continuously, with total weight losses of 6.82%, 6.40%, and 6.17% for SF, SFNb0.1, and SFNb0.2, respectively, over the entire temperature range. The weight loss observed from room temperature to 200 °C is attributed primarily to the loss of physically adsorbed water. At approximately 400 °C, the TG curves of the three samples begin to show noticeable slope changes and significant weight loss, indicating the release of lattice oxygen.

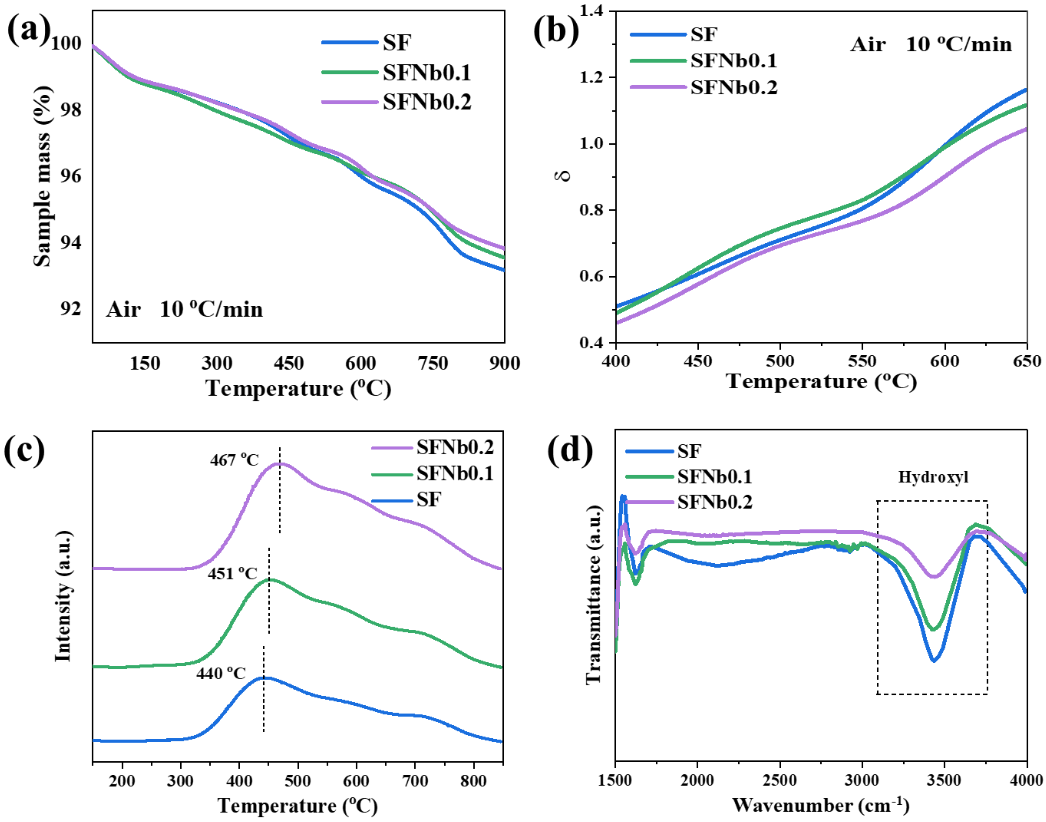

Figure 4. 4 Bulk oxygen and proton defect concentrations of SFNbx materials. (a) TG curves of the samples measured from room temperature to 900 °C. (b) Oxygen non-stoichiometry at 400–650 °C derived from TG curves and iodometric titration results. (c) O_2-TPD profiles of the fresh samples. (d) FT-IR spectra of SFNbx samples after hydration in 6% H_2O-air for 5 hour at 600 °C.

To further quantify oxygen loss at operating temperatures, the oxygen vacancy concentration is calculated by combining the room-temperature oxygen vacancy content with the weight changes observed in the intermediate temperature range (400–650 °C), as shown in **Figure 4.4b**. Under low Nb doping levels (SFNb0.1), the average oxygen vacancy concentration remains comparable to that of SF. However, as the Nb doping level increases to SFNb0.2, the oxygen non-stoichiometry (δ) significantly decreases.

O_2-TPD analysis is conducted to characterize the oxygen desorption properties of the three samples, as shown in **Figure 4.4c**. The initial desorption temperatures of lattice oxygen for SF, SFNb0.1, and SFNb0.2 are 440, 451, and 467 °C, respectively. The increased oxygen desorption temperature indicates that oxygen ions become more difficult to escape from the lattice with the introduction of Nb. This phenomenon is likely attributed to the elevated average metal–oxygen bond energy at the B-site caused by Nb incorporation.

Figure 4.4d shows the FT-IR spectra of the three samples after treatment in a humid atmosphere. SFNbx samples are hydrated in 6% H_2O-air at 600 °C for 5 hours to facilitate hydration reactions. Subsequently, the samples are annealed to 100 °C in dry air to remove surface-adsorbed water. As the Nb doping level increases, the intensity of the -OH absorption peak near 3600 cm^{-1} gradually weakens, indicating a reduction in the surface hydration capacity of the materials.It is generally recognized that the bond strength and bond length of metal–oxygen bonds in a material influence its hydration energy [10]. Considering that the surface oxygen vacancy concentration of the SFNb0.1 sample is similar to that of SF, its suppressed hydration performance may be associated with the enhanced strength of metal–oxygen bonds on the material's surface.

The excellent ORR/WOR performance of air electrodes typically depends on good bulk oxygen ion conductivity and surface exchange rates. For example, in proton ceramic fuel cells (PCFCs), higher oxygen ion conductivity facilitates the transport of oxygen ions to electrochemical reaction sites, while superior oxygen surface exchange performance enables faster dissociation and reduction of oxygen molecules to form oxygen ions. Therefore, the electrical conductivity relaxation (ECR) curves of three materials were tested to investigate their oxygen-related properties in the temperature range of 500–650 °C, as shown in **Figures 4.5a–c**. The ECR curves were obtained by rapidly switching the oxygen partial pressure from 0.21 atm (21 vol.% O_2–79 vol.% N_2) to 0.10 atm (10 vol.% O_2–90 vol.% N_2).

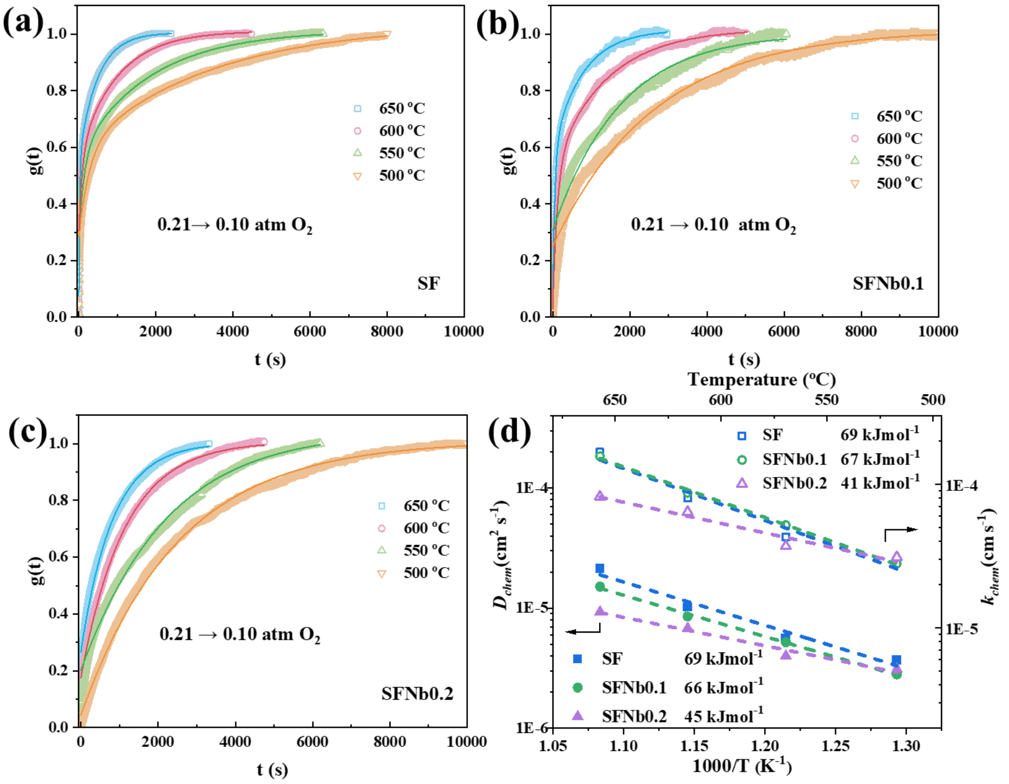

Figure 4. 5 Oxygen exchange and transport properties of SFNbx materials in a dry atmosphere. (a-c) ECR curves during the transition from 21%O_2-79%N_2 to 10%O_2-90%N_2. (d) Surface oxygen exchange coefficient (k_{chem}) and bulk oxygen diffusion coefficient (D_{chem}) of the samples in a dry atmosphere.

The curves were fitted using ECRTOOLS to determine the surface oxygen exchange coefficient (k_{chem}) and the bulk oxygen diffusion coefficient (D_{chem}) for the three samples [135], as presented in **Figure 4.5d**. As the testing temperature increased from 500 °C to 650 °C, the time required for the samples to reach a steady state significantly decreased, indicating faster bulk mass transport and surface exchange rates. When a small amount of Nb was incorporated (SFNb0.1), the surface oxygen exchange performance of the material remained largely unchanged, while the bulk oxygen diffusion rate slowed down. With the Nb doping level increased to SFNb0.2, both k_{chem} and D_{chem} of the material decreased significantly, possibly due to the excessive introduction of Nb reducing the content of oxygen vacancies in both the surface and bulk phases [150].

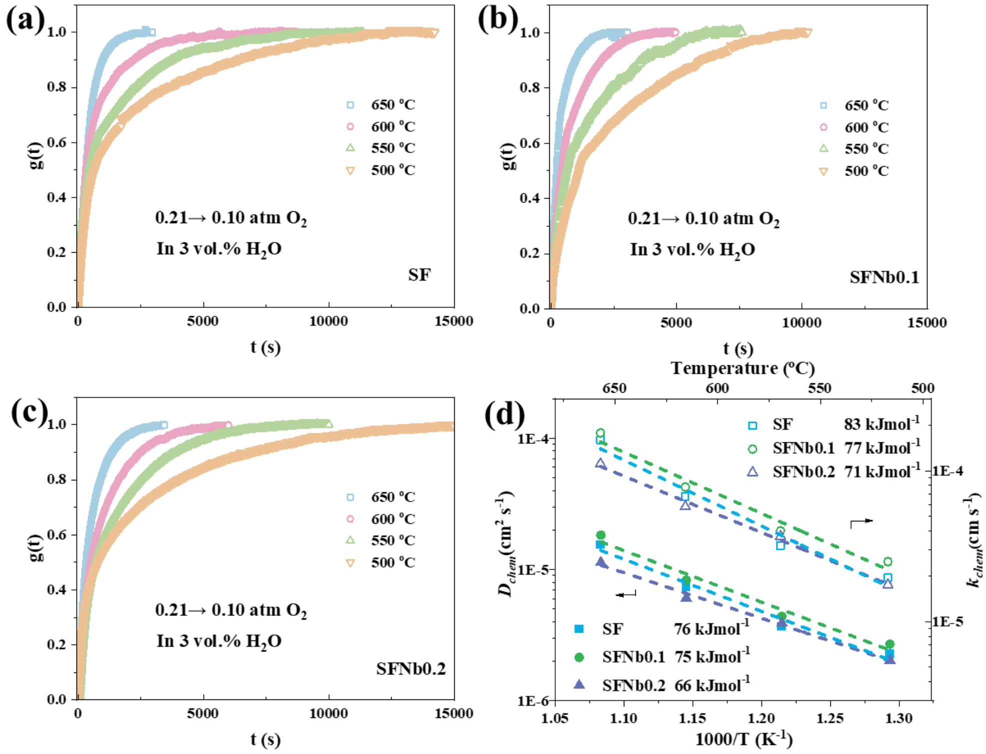

Figure 4. 6 Oxygen exchange and transport properties of SFNbx materials in a humid (3 vol.% H_2O) atmosphere. (a-c) ECR curves during the transition from 21%O_2-79%N_2 to 10%O_2-90%N_2. (d) D_{chem} and k_{chem} of the samples in a humid atmosphere.

The ECR curves of the three samples in humid atmospheres were also tested to further investigate their oxygen-related properties under humid working conditions, as shown in **Figures 4.6a–c**. The oxygen partial pressure was rapidly switched from 0.21 atm to 0.10 atm using N_2 as the balancing gas. The k_{chem} and D_{chem} values for the three samples are presented in **Figure 4.6d**. Compared to dry atmospheres, both D_{chem} and k_{chem} of the three samples decrease within the temperature range of 500–650 °C under humid conditions, indicating competition between surface water/oxygen adsorption and bulk proton/oxygen transport. Moreover, SFNb0.1 exhibits increased Dchem and kchem compared to SF, while the surface and bulk oxygen-related properties of SFNb0.2 remain inferior to those of SF. These results suggest that a small amount of Nb incorporation improves the oxygen surface exchange and bulk transport properties of the material under humid conditions, whereas excessive Nb doping adversely affects its oxygen-related properties.

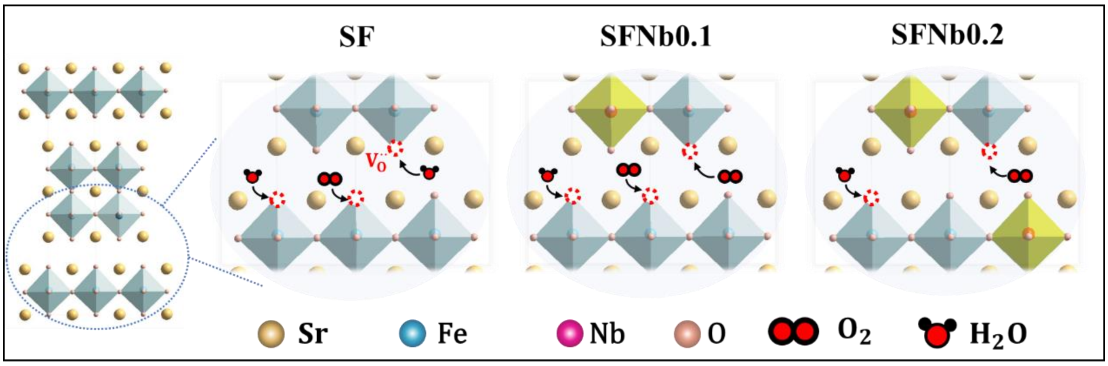

Figure 4. 7 Mechanism of Nb doping in regulating the oxygen–proton-related properties of the material.

Figure 4.7 illustrates the mechanism by which Nb incorporation influences the oxygen- and proton-related properties of the material. The incorporation of Nb enhances the metal–oxygen bond strength, affecting the material’s hydration performance and oxygen vacancies, which in turn impacts proton/oxygen transport and surface exchange. In SFNb0.1, the introduction of a small amount of Nb weakens surface hydration without altering the oxygen vacancy concentration. This creates more surface oxygen vacancies available for oxygen surface exchange, resulting in improved oxygen surface exchange and bulk transport properties under humid conditions. In contrast, excessive Nb doping in SFNb0.2 reduces oxygen vacancies in both the surface and bulk phases, leading to the suppression of both oxygen- and proton-related properties.

4.5 Electrochemical Performance of Air Electrode Candidates

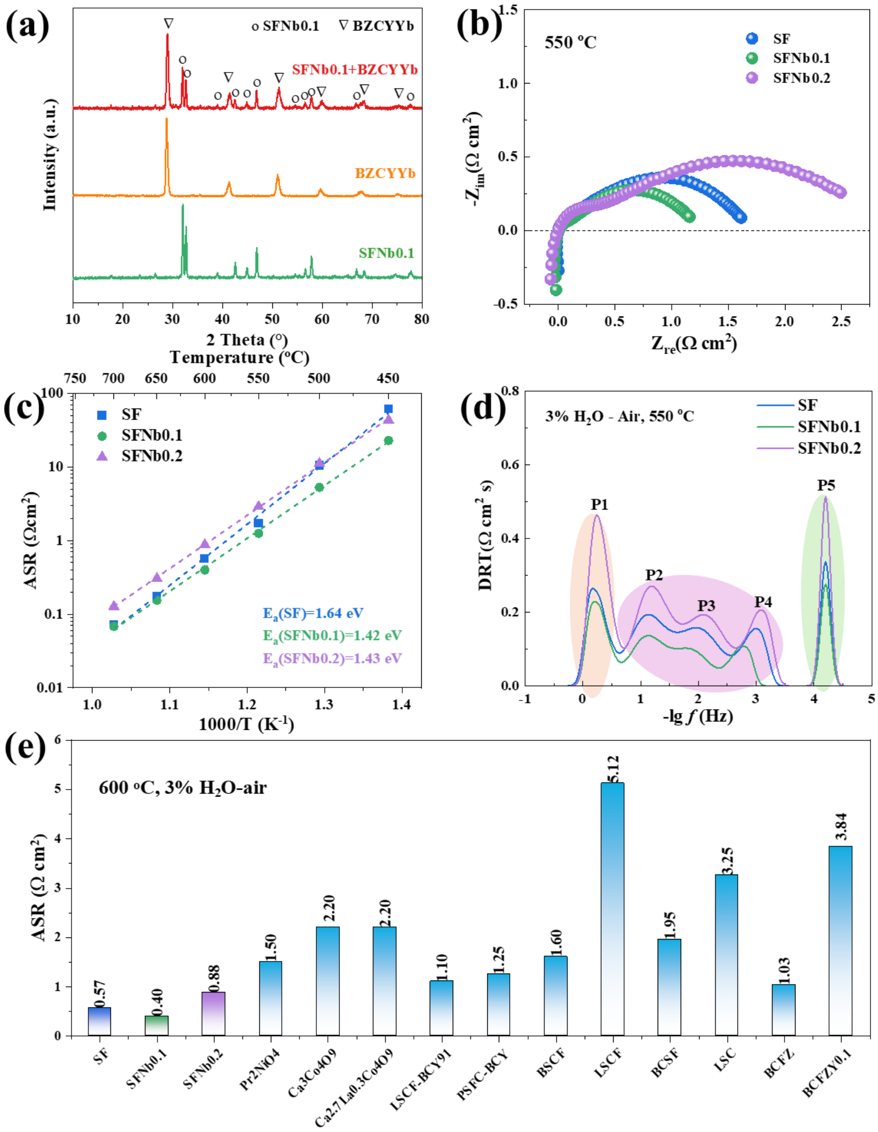

Figure 4. 8 Performance of SFNbx electrodes based on symmetrical cells. (a) XRD of a mixed powder of SFNb0.1 and electrolyte. (b) EIS under a humid atmosphere at 550 °C. (c) Arrhenius curve under a humid atmosphere. (d) DRT analysis of EIS curve. (e) Comparison of the ASR of the SFNbx electrodes with the reported electrode performance under the same conditions.

As shown in **Figure 4.8**, the ORR/WOR performance of three candidate air electrodes based on SFNbx|BZCYYb|SFNbx symmetric cells is evaluated. Initially, the phase compatibility between the electrode powder and the electrolyte material is tested, as depicted in **Figure 4.8a**. After thoroughly mixing and calcining SFNb0.1 and BZCYYb powders at 1100 °C for 2 h, only the characteristic XRD peaks of SFNb0.1 and BZCYYb are observed, indicating that the powders are chemically stable and do not undergo interfacial reactions.

Subsequently, the EIS curves of the three electrodes are tested on symmetrical cells, as shown in **Figure 4.8b**. With the incorporation of Nb, SFNb0.1 exhibits lower R_p compared to SF, indicating that a small amount of Nb incorporation optimizes the electrode activity. However, further increasing the Nb doping to 0.2 results in a decline in electrode performance, as evidenced by a significant increase in R_p. The Arrhenius plots of the three symmetrical cells are shown in **Figure 4.8c**. In the temperature range of 450–700 °C, SFNb0.1 consistently demonstrates the lowest R_p, with the performance enhancement primarily attributed to the optimal balance between proton and oxygen properties. The activation energies (E_a) for the electrode reactions of SF, SFNb0.1, and SFNb0.2 are 1.64 eV, 1.42 eV, and 1.43 eV, respectively, indicating that Nb incorporation reduces the activation energy of the electrode reaction.

To further investigate the mechanism by which Nb incorporation affects performance, DRTTOOLS is used to analyze the EIS curves, where the peak areas represent the impedance of the corresponding electrochemical sub-processes (**Figure 4.8d**). According to literature reports, the low-frequency P1 peak in the 10^{-1}-10^{1} Hz range corresponds to gas diffusion and surface adsorption processes, the mid-frequency P2/P3/P4 peaks in the 10^1-10^4 Hz range correspond to surface exchange and bulk transport processes, and the high-frequency P5 peak above 10^4 Hz corresponds to ionic transport processes[151-152]. The mid-frequency peaks of the three electrodes occupy the largest peak areas, indicating that the surface exchange and bulk transport processes are the rate-determining steps of the electrode reactions. The low- and mid-frequency resistances of SFNb0.2 significantly increase compared to SF, indicating that the gas diffusion/surface adsorption and surface exchange/bulk transport processes are hindered. The reduced surface oxygen vacancies may decrease the surface adsorption performance of O_2/H_2O and hydration, while the reduced bulk oxygen vacancies are detrimental to bulk O^{2-} diffusion. In comparison to other sub-processes, the mid-frequency resistance of SFNb0.1 is significantly lower than that of SF, indicating that the accelerated surface exchange and bulk diffusion processes contribute to the optimized performance of SFNb0.1. This may be related to the superior D_{chem} and k_{chem} of SFNb0.1 under humid conditions.

Additionally, the performance of the SFNbx electrodes is compared with other advanced air electrodes reported in the literature under the same testing conditions (**Figure 4.8e** and **Table 4.2**), showing that SFNb0.1 exhibits excellent performance, even surpassing some advanced Co-based electrodes.

Table 4. 2 The performance comparison of SFNbx air electrodes with that of advanced air electrodes reported in the literature under conditions of 3% H_2O-air at 600 °C.

Air Electrode	Electrolyte	ASR (Ω cm^2)	Ref.
SF	BZCYYb	0.57	This work
SFNb0.1	BZCYYb	0.40	This work
SFNb0.2	BZCYYb	0.88	This work
PNO	BCY91	1.50	[153]
CCO	BCY91	2.20	[154]
CLCO	BCY91	2.20	[154]
LSCF-BCY91	BCY91	1.10	[155]
PSFC-BCY91	BCY91	1.25	[156]
BSCF	BCY91	1.60	[157]
LSCF	BZCYYb	5.12	[158]
BCSF	BCS	1.95	[159]
LSC	BZCY	3.25	[160]
BCFZ	BZCYYb	1.03	[158]
BCFZY0.1	BZCYYb	4.01	[161]

Note: BZCYYb: $BaZr_{0.1}Ce_{0.7}Y_{0.1}Yb_{0.1}O_{3-\delta}$; BCY91: $BaCe_{0.9}Y_{0.1}O_{3-\delta}$; PNO: Pr_2NiO_4; CCO: $Ca_3Co_4O_9$; CLCO: $Ca_{2.7}La_{0.3}Co_4O_9$; LSCF: $La_{0.6}Sr_{0.4}Fe_{0.8}Co_{0.2}O_{3-\delta}$; PSFC: $Pr_{0.58}Sr_{0.4}Fe_{0.8}Co_{0.2}O_{3-\delta}$; BSCF: $Ba_{0.5}Sr_{0.5}Co_{0.8}Fe_{0.2}O_{3-\delta}$; BCSF: $BaCe_{0.4}Sm_{0.2}Fe_{0.4}O_{3-\delta}$; LSC: $La_{0.6}Sr_{0.4}CoO_{3-\delta}$; BCFZ: $BaCo_{0.4}Fe_{0.4}Zr_{0.2}O_{3-\delta}$; BCFZY0.1: $BaCo_{0.4}Fe_{0.4}Zr_{0.1}Y_{0.1}O_{3-\delta}$; BCS: $BaCe_{0.80}Sm_{0.20}O_{3-\delta}$; BZCY: $BaCe_{0.54}Zr_{0.36}Y_{0.1}O_{2.95}$.

Furthermore, the electrochemical performance of the three electrodes under different water vapor pressures is analyzed, as shown in **Figure 4.9**. Compared to a dry atmosphere, the performance of all three electrodes is optimized upon the introduction of 3% water vapor, as indicated by a significant reduction in R_p (**Figures 4.9a-c**). DRT analysis (**Figures 4.9d-f**) shows that the low-frequency and mid-frequency peaks decrease significantly with the introduction of water, indicating that the processes of gas adsorption, surface exchange, and bulk diffusion at the electrode surface are notably optimized. This improvement is mainly due to the hydration reaction of SF-based materials in a humid atmosphere, which leads to the formation of proton defects. Consequently, the reaction sites extend from the original electrode/electrolyte interface to the entire electrode surface and even the electrode bulk. As the water vapor pressure increases from 3 vol.% to 6 vol.%, the performance of the SF electrode declines, indicated by increased low-frequency and mid-frequency impedance. In contrast, the performance of SFNb0.1 and SFNb0.2 continues to improve.

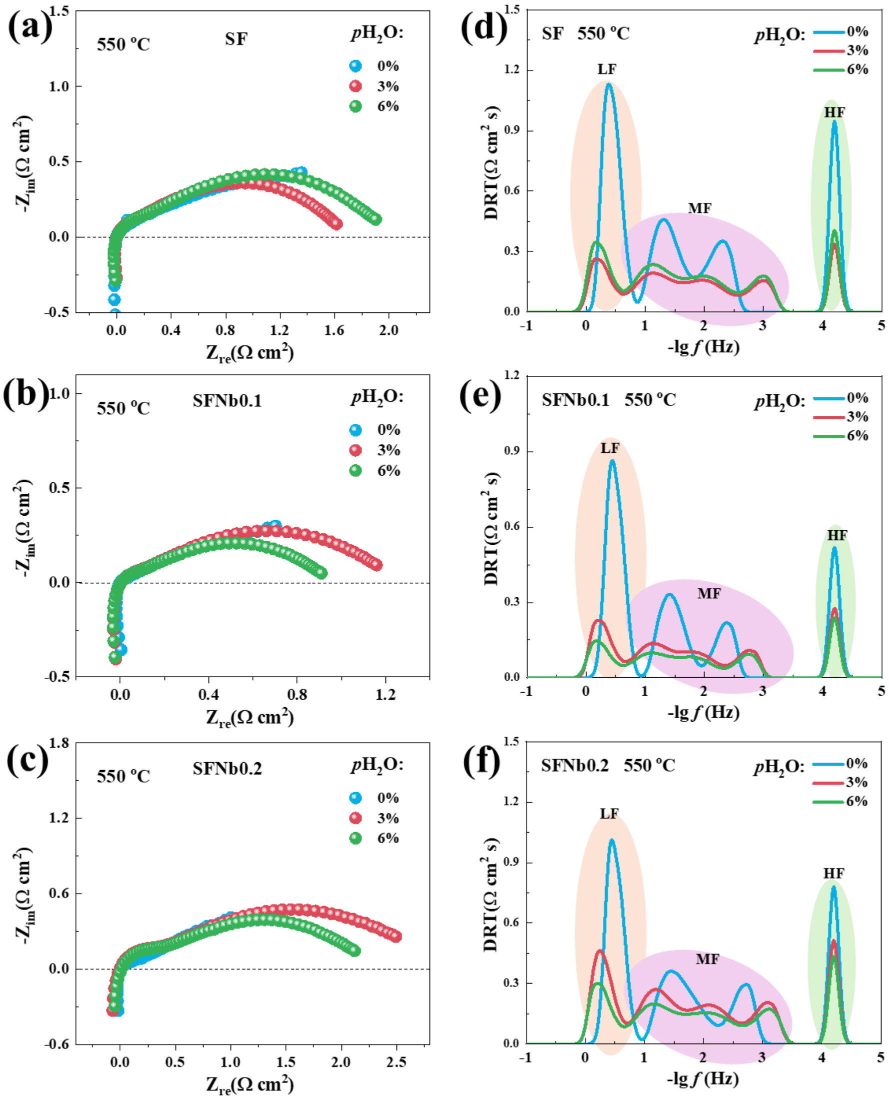

Figure 4. 9 Effect of water pressure on the performance of SFNbx electrode. (a-c) EIS spectra of SFNbx electrodes under different water pressures. (d-f) Corresponding DRT analysis.

To provide a clearer representation of electrode performance, the variation of R_p with steam pressure for SFNbx electrodes at 550 °C is plotted in **Figure 4.10a**. The polarization resistance of the SF electrode initially decreases and then increases with increasing water vapor pressure, achieving optimal performance under 3 vol.% H_2O-air. In contrast, the performance of SFNb0.1 and SFNb0.2 electrodes improves continuously with increasing water vapor pressure, reaching the lowest R_p in a 6 vol.% H_2O-air atmosphere.

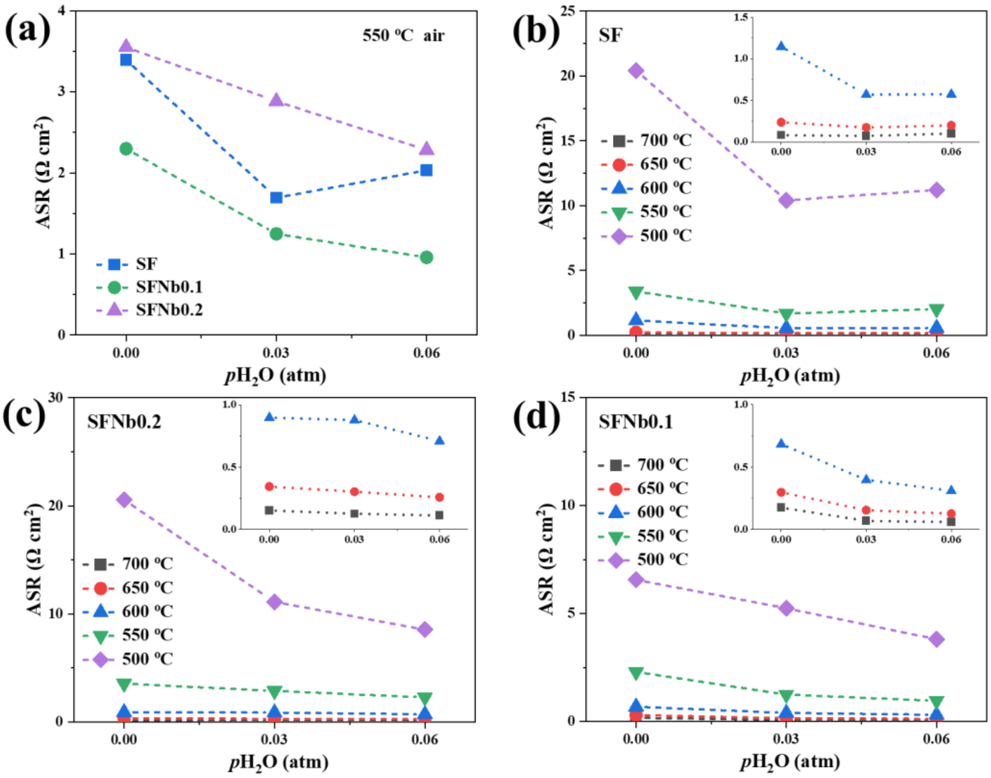

Figure 4. 10 Effect of water vapor pressure on the performance of SFNbx electrodes. (a) R_p of the electrodes under different water vapor pressures at 550 °C. (b–d) Variation of R_p with water vapor pressure for the three electrodes in 500–700 °C.

Additionally, **Figures 4.10b–d** show the variation of polarization resistance with water vapor pressure for the three electrodes in the temperature range of 500–700 °C. Across the testing temperature range, the performance trends of all three electrodes with increasing water vapor pressure are consistent with those observed at 550 °C.

According to the study by Shao et al., high water vapor pressure introduces competitive interference between oxygen and water adsorption on the surface of air electrodes [7]. The increased R_p of SF under higher steam pressure indicates a decline in its ORR/WOR performance, likely due to suppressed oxygen surface exchange and bulk transport. The incorporation of Nb enhances the tolerance of the electrodes to water vapor, adjusts the competition between water and oxygen surface adsorption, and subsequently improves electrode activity.

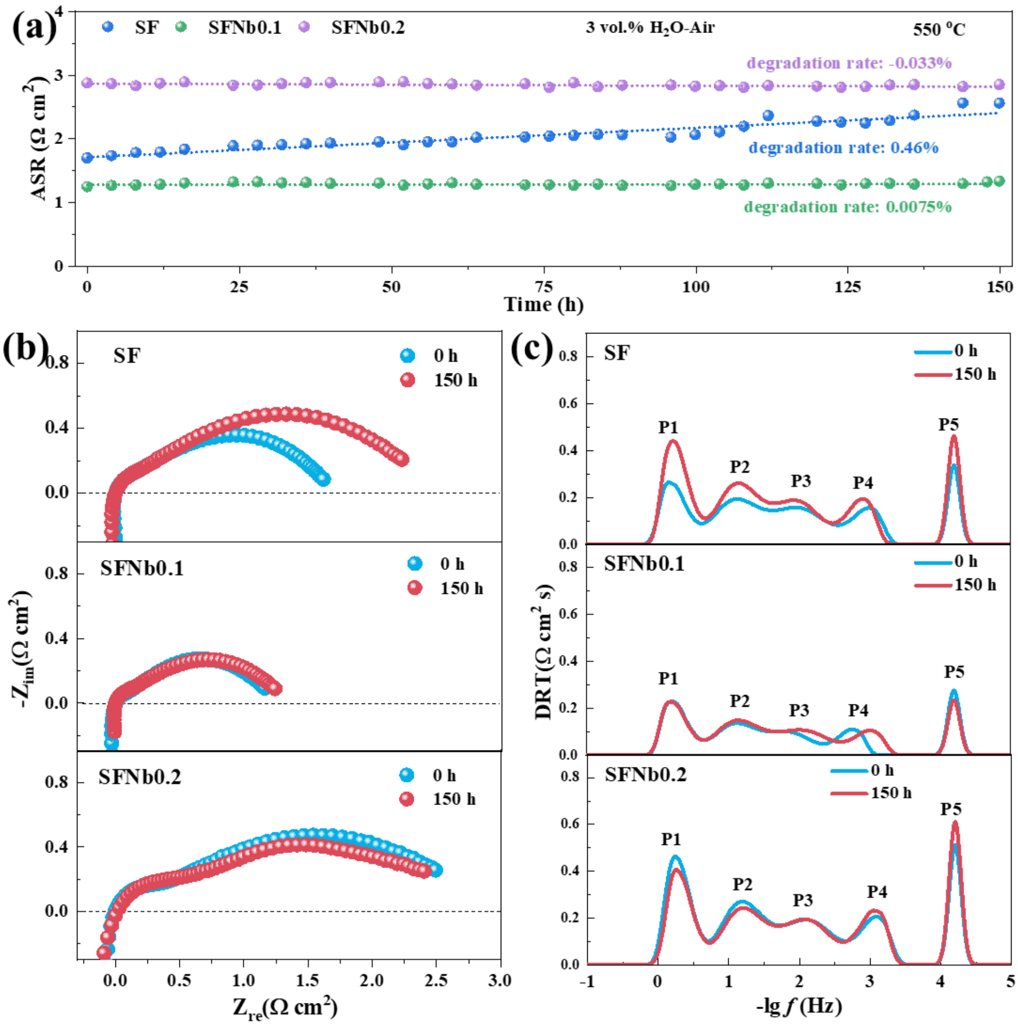

Figure 4. 11 Stability test of symmetrical cells at 3% H_2O-air, 550 °C. (b) EIS curve evolution after the 150-h test. (c) DRT analysis

The performance evolution of the three electrodes in a humid atmosphere over 150 hours is evaluated, as shown in **Figure 4.11a**. The R_p of the SF electrode exhibits a degradation rate of 0.46% Ω cm^2 h^{-1}, while the degradation rates of SFNb0.1 and SFNb0.2 are significantly lower, at 0.0075% Ω cm^2 h^{-1} and -0.033% Ω cm^2 h^{-1}, respectively.

EIS and DRT analyses are conducted to further investigate the mechanisms underlying the performance changes, as illustrated in **Figures 4.11b-c**. The low- and mid-frequency resistances of the SF electrode increase significantly after 150 hours, indicating increased resistance in surface adsorption, surface exchange, and bulk transport processes. In contrast, the sub-process resistances of SFNb0.1 and SFNb0.2 remain unchanged.

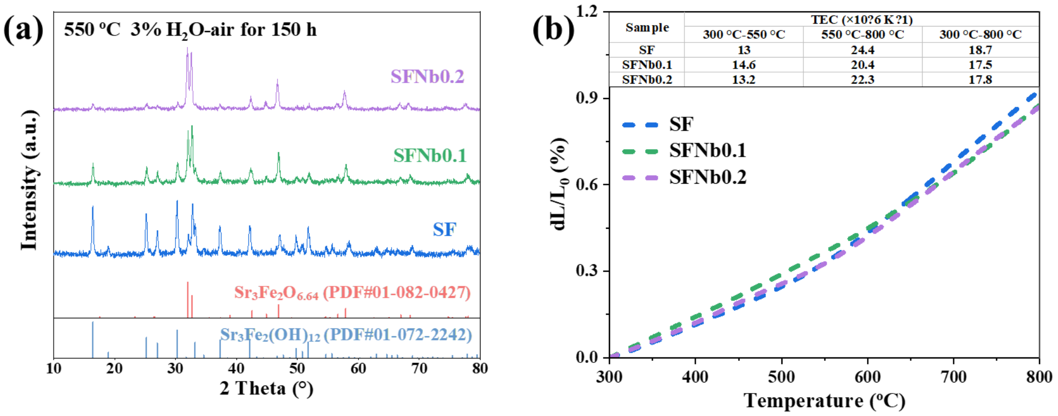

Sample	TEC (×10?6 K?1)		
	300 °C-550 °C	550 °C-800 °C	300 °C-800 °C
SF	13	24.4	18.7
SFNb0.1	14.6	20.4	17.5
SFNb0.2	13.2	22.3	17.8

Figure 4. 12 Structural stability and thermal expansion tests of SFNbx samples. (a) XRD patterns of the samples after 150 hours of treatment in a humid atmosphere, (b) thermal expansion curves in the temperature range of 300–800 °C.

The XRD patterns of SFNbx powders after 150 hours of treatment in a humid atmosphere are tested to investigate the phase structural stability of the samples, as shown in **Figure 4.12(a)**. After treatment, a significant secondary phase appears in the

SF powders, which can be identified as the $Sr_3Fe_2(OH)_{12}$ phase (PDF#01-072-2242). With the introduction of Nb, the intensity of the secorndary phase peaks decreases significantly. The substantially reduced proportion of the secondary phase indicates that Nb incorporation stabilizes the phase structure of the samples under humid conditions, and a stable phase structure is generally a prerequisite for maintaining stable electrode performance.

In addition, the thermal expansion curves of the three samples in the temperature range of 300–800 °C are tested, as shown in **Figure 4.12(b)**. The slopes of the thermal expansion curves for all three samples change around 550 °C. According to the literature, thermal expansion in the 300–550 °C range is typically attributed to anharmonic atomic vibrations, while that in the 550–800 °C range is primarily due to the reduction of Fe^{4+}. The thermal expansion coefficients in the 300–550 °C and 550–800 °C ranges, as well as the average thermal expansion coefficients, are calculated for the SFNbx samples, with results summarized in the table in **Figure 4.12(b)**. The average linear thermal expansion coefficients of SF, SFNb0.1, and SFNb0.2 are 18.7, 17.5, and $17.8\times10^{-6}\ K^{-1}$, respectively. The introduction of Nb reduces the thermal expansion coefficient of the material, which helps to mitigate thermal mismatch between the electrode and the electrolyte.

4.6 Single Cell Application

The excellent ORR and WOR activity of the SFNb0.1 air electrode is validated in the RePCC. **Figure 4.13a** shows the power density curves of the single cell with SNb0.1 as the air electrode tested at 450-650 °C. When H_2 is used as the fuel gas and humidified air as the oxidant, the maximum power densities of the single cell at 650, 600, 550, 500, and 450 °C are 576, 442, 302, 188, and 105 mWcm^{-2}, respectively, which are significantly higher than those of the cell with the SF air electrode at 468, 319, 214, 144, and 85 mWcm^{-2} (as shown in **Figure 4.13b**). Given that the electrolyte and fuel electrode compositions of both single cells are the same, with the only difference being the composition of the air electrode materials, the performance enhancement of the single cell with the SFNb0.1 air electrode is primarily attributed to the modification of the SFNb0.1 air electrode.

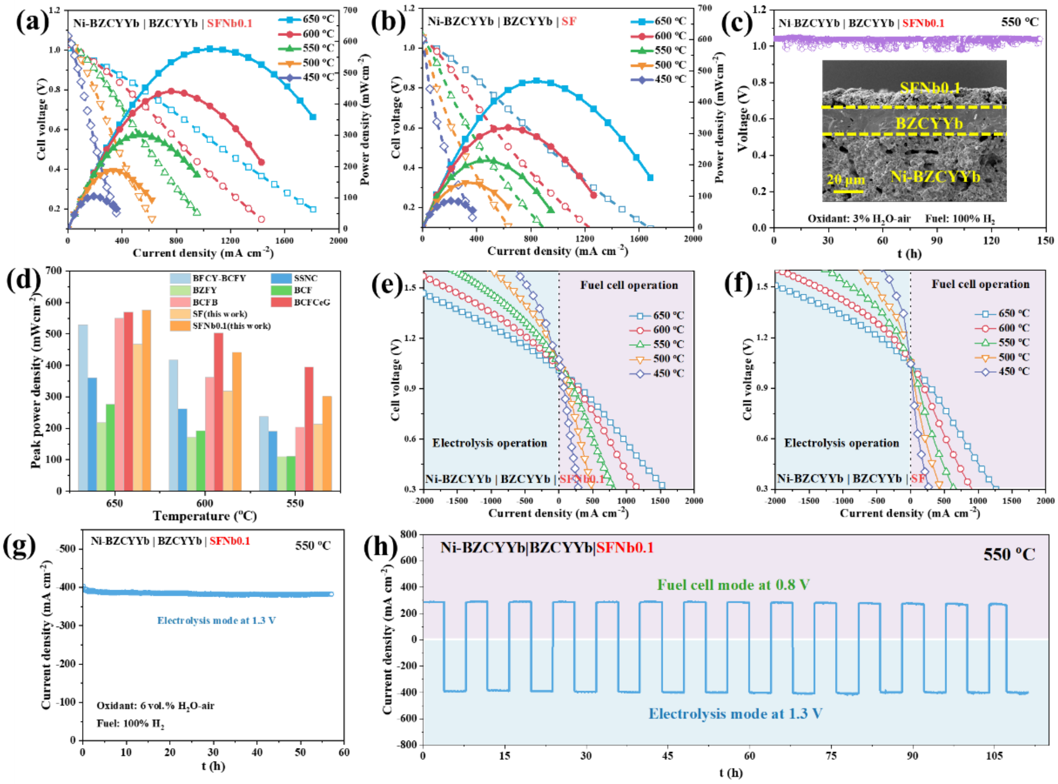

Figure 4. 13 The electrochemical performance of the single cell. The single cell power density curves: (a) SFNb0.1 air electrode, (b) SF air electrode. (c) The operational stability of the single cell at 550 °C, with the inset showing the cross-sectional SEM of the SFNb0.1-based single cell after testing. (d) The maximum power density compared to the performance reported in the literature. The polarization curve in the 0.3-1.6V range: (e) SFNb0.1 electrode, (f) SF electrode. (g) The electrolysis stability of the cell under 1.3 V. (h) The operational stability of the cell in the reversible fuel cell-electrolysis cell mode for nearly 112 hours.

Figure 4.13c demonstrates the stability of the single cell operated for nearly 150 hours, with the open circuit voltage remaining around 1.04 V, indicating good sealing and operational stability during cell operation.

Table 4. 3 Comparison of the performance of single cells with SFNb0.1 electrodes to previously reported single cell performances

Air electrode	Electrolyte	PPD (mW cm^{-2})					Ref.
		650 °C	600 °C	550 °C	500 °C	450 °C	
BFCY-BCFY	BZCY (15 μm)	530	417	237			[162]
SSNC	BZCY (46 μm)	361	262	190	141		[163]
BZFY	BZCY (32 μm)	218	171	109			[68]
BCF	BZCY (25μm)	276	192	111			[164]
BCFB	BZCY (25 μm)	551	362	203			[165]
BCFCeG	BZCYYb (30 μm)	570	504	395			[166]
SF	BZCYYb (20 μm)	468	319	214	144	85	This work
SFNb0.1	BZCYYb (20 μm)	576	442	302	188	105	This work

Note: BFCY: $BaFe_{0.8}Ce_{0.1}Y_{0.1}O_{3-\delta}$; BCFY: $BaCe_{0.8}Fe_{0.1}Y_{0.1}O_{3-\delta}$; SSNC: $SrSc_{0.175}Nb_{0.025}Co_{0.8}O_{3-\delta}$; BZFY: $BaZr_{0.2}Fe_{0.6}Y_{0.2}O_{3-\delta}$; BCFB: $BaCe_{0.5}Fe_{0.3}Bi_{0.2}O_{3-\delta}$; BCF: $BaCe_{0.5}Fe_{0.5}O_{3-\delta}$; BCFCeG: $BaCo_{0.4}Fe_{0.4}Ce_{0.1}Gd_{0.1}O_{3-\delta}$; BZCYYb: $BaZr_{0.1}Ce_{0.7}Y_{0.1}Yb_{0.1}O_{3-\delta}$; BZCY: $BaZr_{0.1}Ce_{0.7}Y_{0.2}O_{3-\delta}$.

Additionally, the SEM image of the SFNb0.1-based single cell after testing, shown in the inset of **Figure 4.13c**, reveals good contact between the porous electrode and the dense BZCYYb electrolyte (approximately 20 μm). The performance of the SFNb0.1-based single cell is also compared with reported single cells under the same test conditions, as shown in **Figure 4.13d** and **Table 4.3**. The SFNb0.1-based single cell exhibits leading performance, demonstrating the high activity of the SFNb0.1 air electrode. Notably, the cell electrolyte thickness in this study is 20 μm, whereas the electrolyte thickness in high-performance cells is typically much less than 20 μm, indicating that the performance of the single cell with the SFNb0.1 air electrode can be further optimized by improving the electrolyte configuration.

Further testing of the cell's polarization curves in FC and EC modes is conducted to investigate the cell's performance in electrolysis mode (**Figure 4.13e**). At 1.3V, the cell with the SFNb0.1 air electrode shows current densities of 1135, 793, 512, and 302 $mAcm^{-2}$ at 650, 600, 550, and 500 °C, respectively, which are significantly higher than those of the cell with the SF air electrode at 842, 552, 336, and 187 $mAcm^{-2}$ (**Figure 4.13f**). Furthermore, the 57-hour electrolysis stability test results show almost no degradation in the cell's electrochemical performance, demonstrating good operational stability in electrolysis mode. Finally, shown in **Figure 4.13g**, in a simulated reversible mode operation with renewable energy, the cell with the SFNb0.1 air electrode operates stably during dynamic cycling for 14 cycles (approximately 112 hours) in both electrolysis mode (under 1.3 V operation) and fuel cell mode (under 0.8 V operation), confirming the high stability of the SFNb0.1 air electrode for use in RePCC.

4.7 Conclusion

In this study, SFNbx materials with an RP phase structure were successfully synthesized using the sol-gel method. By adjusting the incorporation of Nb^{5+} ions, the surface and bulk oxygen vacancies of the materials are controlled, improving the competitive adsorption of oxygen and water on the surface. Moreover, the introduction of Nb enhances the structural stability and improved the thermal expansion coefficient of the material. The moderately doped SFNb0.1 material exhibits superior ORR/WOR performance under humid conditions, with lower polarization resistance and reaction activation energy. The RePCC based on the SFNb0.1 air electrode achieves a maximum power density of 576 mW cm^{-2} at 650 ^{o}C and a current density of 1.14 A cm^{-2} at 1.3 V, significantly outperforming the undoped SF electrode, highlighting the effectiveness of Nb doping in enhancing electrochemical performance. The RePCC with the SFNb0.1 air electrode demonstrates competitive electrochemical performance and excellent durability during a 112-hour test. This study underscores the importance of regulating oxygen vacancies to balance proton and oxygen properties in SF-based electrodes, providing new insights and approaches for developing efficient and stable electrode materials.

CHAPTER 5 Rational Design of Ruddlesden-Popper Perovskite Ferrites as Air Electrode for Highly Active and Durable Reversible Protonic Ceramic Cells

5.1 Introduction

In the previous chapter, we introduced Nb into the Fe-based RP-type perovskite $Sr_3Fe_2O_{7-\delta}$ (SF) to regulate the material's oxygen vacancies and metal-oxygen bond strength. The resulting $Sr_3Fe_{1.9}Nb_{0.1}O_{7-\delta}$ (SFNb0.1) air electrode, with an improved balance of proton-oxygen properties, demonstrates excellent electrochemical activity and stability, highlighting the significant potential of SF-based RP perovskite materials as RePCC air electrodes.

However, under RePCC conditions, SF-based perovskite materials are prone to forming the $Sr_3Fe_2(OH)_{12}$ (SFH) phase, which disrupts the primary SF phase structure [167]. Although Nb doping has significantly reduced the proportion of secondary phases in SFNb0.1, the remaining fraction of secondary phases is still dinstict and may lead to a decline in cell stability during extended operation. Therefore, it is essential to develop highly active SF-based air electrode materials with enhanced phase structure stability.

Doping high oxidation state elements (e.g., Ti^{4+}, Zr^{4+}, and Nb^{5+}) is a common strategy to improve material durability [168-170]. Among them, Nb^{5+}, due to its higher oxidation state and stronger Nb-O bond strength, is considered an ideal dopant for enhancing material stability [171-172]. Notably, in previous studies, $SFNb_{0.2}$ with a high Nb doping concentration demonstrated excellent phase structure stability after 150 hours of humid treatment.

However, high-valence doping strategies may negatively impact electrochemical performance, as the introduction of high-valence elements reduces oxygen vacancies in the material, which are critical for oxygen ion transport and hydration reactions [144]. For example, $Sr_3Fe_{1.8}Nb_{0.2}O_{7-\delta}$ (SFNb0.2) exhibits inferior hydration properties and oxygen surface exchange/transport characteristics in humid atmospheres compared to SF, primarily due to the reduced surface and bulk oxygen vacancy concentrations. Introducing A-site vacancies alongside high-valence element doping is a common strategy to increase oxygen vacancy concentration in perovskite materials.

Building on the findings from the previous study, this research proposes a simple A/B-site co-doping strategy to design and develop stable and efficient SF-based perovskite air electrodes for RePCC applications. In this study, a series of $Sr_{3-0.1x}Fe_{1.8}Nb_{0.2}O_{7-\delta}$ (Dx-SFN) materials are synthesized by introducing varying degrees of Sr deficiency into SFNb0.2. Nb doping in SF stabilizes its crystal structure under RePCC conditions, suppresses excessive SFH phase formation, and ensures the stability of the primary SF structure. Additionally, the introduction of Sr deficiency increases oxygen vacancy concentrations, thereby enhancing oxygen transport properties. This work explores the optimal Sr deficiency level to achieve air electrode materials for RePCCs with both enhanced performance and durability.

5.2 Material Synthesis

The Dx-SFN ($Sr_{3-0.1x}Fe_{1.8}Nb_{0.2}O_{7-\delta}$, x=0, 1, 2, 4, 6), SF, and BZCYYb materials were prepared by the sol-gel method [89]. For Dx-SFN materials, $Sr(NO_3)_2$ (AR, ≥99.5%),

$Fe(NO_3)_3\cdot9H_2O$ (AR, ≥98.5%), $C_{10}H_5NbO_{20}$ (AR, ≥98%) as the chemical reagents were stoichiometrically dissolved in deionized water on a magnetic heating stirrer at 80 °C until gel formation occurred. The citric acid (AR, ≥99.5%) and EDTA (AR, ≥99.5%) were added as complexing agents and ammonia water (25-28%) was employed to make the solution neutral or slightly alkaline. Subsequently, the gel was heated in the oven at 180 °C for 10 h to obtain the precursor, which was then calcined at 1100 °C for 10 h to obtain the initial Dx-SFN powders.

5.3 Material Composition And Structure

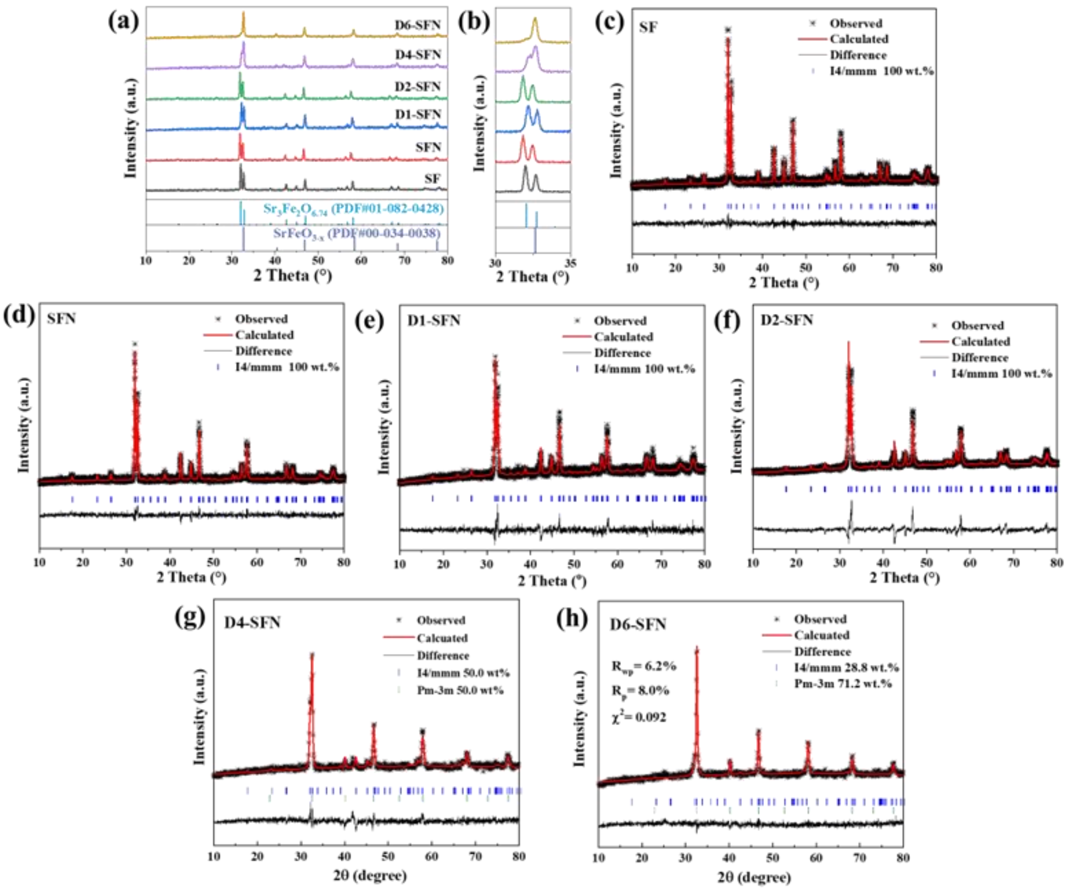

Figure 5. 1 Phase structure of Dx-SFN samples. (a-b) XRD patterns. (c-h) XRD refinement results.

To illustrate the effect of A-site cation defects on material properties, five perovskite precursors with varying A-site Sr deficiency levels, Dx-SFN (x = 0, 1, 2, 4, 6), and the initial SF material are prepared. Their XRD patterns are shown in **Figures 5.1a-b**. When the Sr deficiency content is below 0.2 (x ≤ 2), the samples exhibit the RP-type $Sr_3Fe_2O_{7-\delta}$ layered perovskite phase (PDF#01-082-0427), with no impurities detected. However, when the Sr deficiency exceeds 0.2, a cubic perovskite phase, $SrFeO_{3-\delta}$ (PDF#00-034-0038), is observed in addition to the main phase.

Table 5. 1 Lattice parameters of Dx-SFN powders obtained by XRD Rietveld refinement

Lattice parameter	SF	SFN	D1-SFN	D2-SFN	D4-SFN	D6-SFN
R_p (%)	7.47	9.88	11.5	6.09	10.1	6.20
R_{wp} (%)	9.53	12.60	14.6	8.46	13.1	8.0
χ^2	1.10	1.16	2.44	3.66	2.04	0.92
Phase 1: I4/mmm						
a/b (Å)	3.86634	3.88744	3.89582	3.87987	3.88879	3.89178
c (Å)	20.16277	20.21685	20.22654	20.10515	20.04748	20.06201
Percentage (wt. %)	100.0	100.0	100.0	100.0	50.0	71.2
Phase 2: Pm-3m						
a/b/c (Å)	-	-	-	-	3.89654	3.88568
Percentage (wt. %)	0	0	0	0	50.0	28.8

The XRD refinement patterns (**Figures 5.1c-h**) reveal that for x ≤ 2, the Dx-SFN samples display a pure tetragonal RP phase. In contrast, at x = 4, the D4-SFN sample contains 50 wt.% of the I4/mmm tetragonal phase and 50 wt.% of the Pm$\bar{3}$m cubic phase. For x = 6, the D6-SFN sample consists of 28.8 wt.% of the I4/mmm tetragonal phase and 71.2 wt.% of the Pm$\bar{3}$m cubic main phase. It is well known that A-site elements with larger ionic radii generally form the backbone of perovskite materials [28]. When the Sr deficiency becomes excessive (0.1x ≥ 0.4), the crystal structure destabilizes, leading to a phase transition. Subsequent characterizations focus on the effects of A-site deficiency content in materials with a stable RP phase structure.

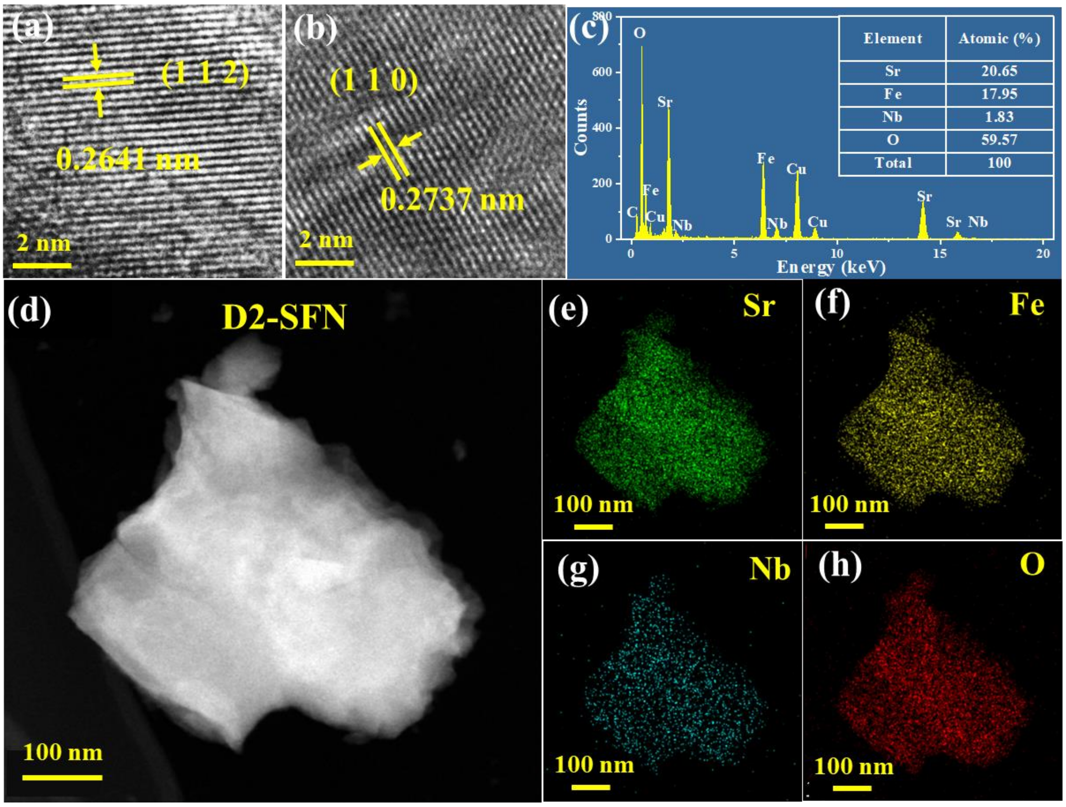

Element	Atomic (%)
Sr	20.65
Fe	17.95
Nb	1.83
O	59.57
Total	100

Figure 5. 2 Micro-morphology of D2-SFN compositions. (a-b) HRTEM verifying crystallinity. (c) EDX confirming elemental composition. (d-h) STEM-EDX mapping demonstrating uniform element distribution.

The microstructure of the samples, represented by D2-SFN, is analyzed using TEM. HR-TEM confirms the crystal structure by measuring interplanar spacings of 0.2641 nm and 0.2737 nm, corresponding to the (112) and (110) crystal planes of RP-type perovskite, respectively (**Figures 5.2a-b**). EDX verifies the expected elemental composition (**Figure 5.2c**). Since EDX is a semi-quantitative method, further elemental composition analysis of the fresh D2-SFN sample is conducted using ICP-OES. The results indicate that the proportions of Sr, Fe, and Nb in the total cation content are 50.63%, 20.04%, and 4.00%, respectively, closely matching the nominal values of

51.49%, 21.10%, and 3.90%, with only minor deviations observed.

STEM reveals that the D2-SFN sample exhibits a uniform nanoparticle morphology with particle sizes ranging from approximately 200–300 nm (**Figure 5.2d**). EDX mapping further confirms the homogeneous substitution of Nb within the parent D2-SFN lattice (**Figures 5.2e-h**).

5.4 Electrochemical Performance of Symmetrical Cells

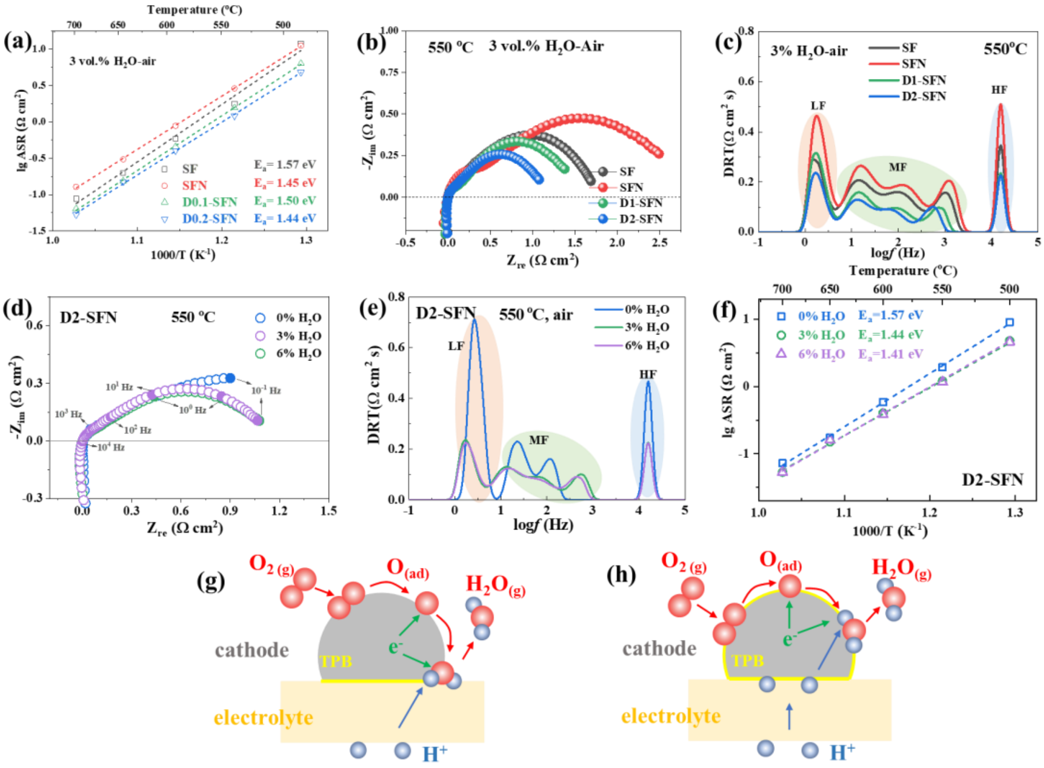

Figure 5. 3 Electrochemical performance and reaction kinetics of the Dx-SFN electrodes. (a) Arrhenius curves in 3 vol.% H_2O-air. (b) EIS curves and (c) DRT curves in 3 vol.% H_2O-air. (d) Impact of pH_2O on EIS and (e) DRT of D2-SFN electrode. (f) Arrhenius plots of the D2-SFN electrode under different pH_2O.(g-h) Schematic diagram of the ORR process: (g) in dry air, (h) in humid air.

To evaluate the effect of A-site defect content on the ORR/WOR reactions of the electrode, the Arrhenius curves of Dx-SFN electrodes is presented in the temperature range of 500–700 °C under standard operating conditions (3 vol.% H_2O-air), as shown in **Figure 5.3a**. The incorporation of Nb reduces the electrochemical activity of the SF electrode, as evidenced by an increase in R_p. Introducing Sr defects significantly decreases the polarization resistance of the electrodes, and higher Sr defect content leads to superior electrode performance. The D2-SFN electrode exhibits the best ORR/WOR performance across the entire temperature range. **Figure 5.3b** presents the EIS curves of the four electrodes at 550 °C in humidified air. At 550 °C, the ASR values for SF, SFN, D1-SFN, and D2-SFN are 1.781, 2.885, 1.558, and 1.209 $\Omega \cdot cm^2$, respectively.

Furthermore, DRT is employed to further separate the electrode reaction processes (**Figure 5.3c**) [173-174]. Typically, low-frequency (LF, 10^{-1}-10^1 Hz) peaks correspond to gas diffusion or surface adsorption/desorption steps; mid-frequency (MF, 10^1-10^4 Hz) peaks relate to surface oxygen exchange and/or bulk diffusion processes; and high-frequency (HF, 10^4-10^5 Hz) peaks represent charge transfer reactions [173-174]. The peak area within a specific frequency range reflects the R_p of the corresponding electrochemical sub-process. Nb incorporation negatively impacts both surface mass transfer and bulk diffusion processes. The subsequent introduction of Sr defects not only eliminates the adverse effects of Nb doping on electrode reactions but also significantly reduces the resistance of all electrochemical sub-processes.

The EIS curves under different vapor pressures (**Figure 5.3d**) are used to further differentiate the ORR/WOR processes of the D2-SFN air electrode. Under varying vapor pressures, the MF and LF peak areas constitute the majority of the DRT curve (**Figure 5.3e**), indicating that gas diffusion, surface exchange, and bulk diffusion resistances are the primary components of R_p. After the introduction of water vapor, MF and LF resistances decrease significantly, suggesting that water vapor markedly enhances the water diffusion, surface mass transfer, and bulk ion transport properties of the electrode [175]. The electrode reaction activation energy (E_a), as shown in **Figure 5.3f**, is significantly optimized due to the generation of proton defects by hydration, effectively improving the bulk proton conductivity of the materials.

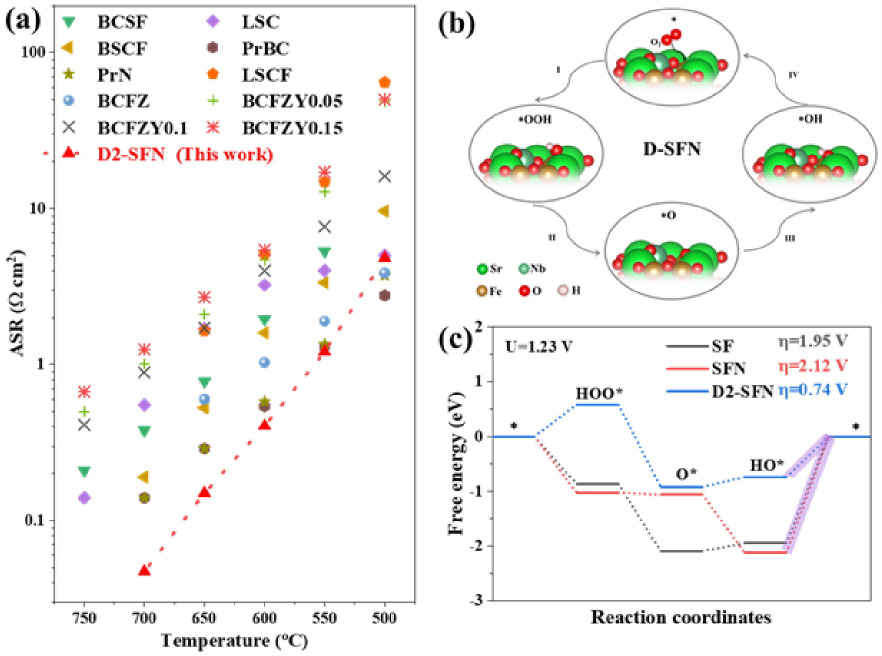

Figure 5. 4 (a) Performance comparison of the D2-SFN electrode with reported electrodes in humid air. (b) Optimized atomic structures of the main ORR processes. (c) Free energy diagram of the ORR reaction for Dx-SFN.

Unlike the ORR in SOFC mode and WOR in SOEC mode at the air electrode of conventional solid oxide cells (SOC), the RePCC air electrode performs more complex ORR in PCFC mode and WOR in PCEC mode due to the involvement of water vapor [80]. To illustrate, **Figure 5.3g** provides a schematic of the ORR occurring at the air electrode in PCFC mode, with the reverse process being WOR. The introduction of water vapor promotes the hydration reaction between surface oxygen vacancies and water molecules, generating proton defects. This expansion of the three-phase boundary from the original electrode-electrolyte interface under dry air conditions (**Figure 5.3h**) to encompass the entire air electrode surface (**Figure 5.3g**) plays a critical role in enhancing ORR/WOR kinetics [39, 176].

To provide a more objective evaluation of the performance of the D2-SFN electrode, **Figure 5.4a** and **Table 5.2** compare the ASR of D2-SFN with that of high-performance air electrodes reported in the literature. The ASR of D2-SFN is even significantly lower than many Co-based air electrodes, demonstrating outstanding electrocatalytic performance.

Table 5. 2 Performance comparison of D2-SFN with reported air electrodes in 3% H_2O-air

Air electrode	ASR (Ω cm^2)						Ref.
	750 °C	700 °C	650 °C	600 °C	550 °C	500 °C	
D2-SFN		0.047	0.15	0.404	1.209	4.81	This work
$BaCe_{0.4}Sm_{0.2}Fe0.4O_{3-\delta}$ (BCSF)	0.21	0.38	0.78	1.95	5.32		159
$La_{0.6}Sr_{0.4}CoO_{3-\delta}$ (LSC)	0.14	0.55	1.7	3.25	4.00	5.00	160
$Ba_{0.5}Sr_{0.5}Co_{0.8}Fe_{0.2}O_{3-\delta}$ (BSCF)		0.19	0.53	1.60	3.36	9.66	157
$PrBaCo_2O_{5+\delta}$ (PrBC)		0.14	0.29	0.54	1.3	2.78	157
$Pr_2NiO_{4+\delta}$ (PrN)		0.14	0.29	0.58	1.35	3.74	157
$La_{0.6}Sr_{0.4}Fe_{0.8}Co_{0.2}O_{3-\delta}$ (LSCF)			1.65	5.12	14.85	64.47	158
$BaCo_{0.4}Fe_{0.4}Zr_{0.2}O_{3-\delta}$ (BCFZ)			0.6	1.03	1.90	3.87	158
$BaCo_{0.4}Fe_{0.4}Zr_{0.15}Y_{0.05}O_3$ (BCFZY0.05)	0.50	1.01	2.10	4.67	12.87	48.63	161
$BaCo_{0.4}Fe_{0.4}Zr_{0.1}Y_{0.1}O_3$ (BCFZY0.1)	0.41	0.89	1.72	4.01	7.69	16.12	161
$BaCo_{0.4}Fe_{0.4}Zr_{0.05}Y_{0.15}O_3$ (BCFZY0.15)	0.67	1.25	2.71	5.43	17.16	50.10	161

Additionally, to further elucidate the mechanism behind the superior ORR performance of D2-SFN, density functional theory (DFT) calculations were conducted. According to the literature, the ORR process on the electrode surface follows a four-electron mechanism, which can be represented by Equations 5.1-5.4 [139-140] :

I $$* + O_2 + H^+ + e^- \rightarrow * OOH \tag{5.1}$$

II $$* OOH + H^+ + e^- \rightarrow * O + H_2O \tag{5.2}$$

III $$* O + H^+ + e^- \rightarrow * OH \tag{5.3}$$

IV $$* OH + H^+ + e^- \rightarrow H_2O \tag{5.4}$$

Figure 5.4b presents the intermediates in the ORR reaction sub-steps for the D2-SFN material, optimized via DFT calculations, where * denotes the active sites on the air electrode. The reaction starts from *, proceeds through *OOH, *O, *OH, and returns to *. The ORR reaction-free energies on the surfaces of SF, Nb-substituted SFN, and A-site-deficient D2-SFN are depicted in **Figure 5.4c**. The ORR on the air electrode surface comprises four steps. According to the ORR reaction barrier, it is evident that the rate-determining step for SF, SFN, and D2-SFN electrodes is located at the H_2O formation step. For SF, the overpotential (η) is 1.95 V, for SFN, the overpotential is 2.12 V, and D2-SFN exhibits a low η of 0.74 V, which is favorable for the rapid reaction kinetics of the air electrode.

5.5 Physicochemical Properties

For the air electrode of RePCC, the excellent electronic conductivity helps to realize the electronic conducting path and provides the necessary conditions for the electrochemical reaction to proceed [177]. Herein, the electronic conductivity of Dx-SFN materials was investigated using the DC four-probe method within a temperature range of 250-750 °C (**Figure 5.5a**).

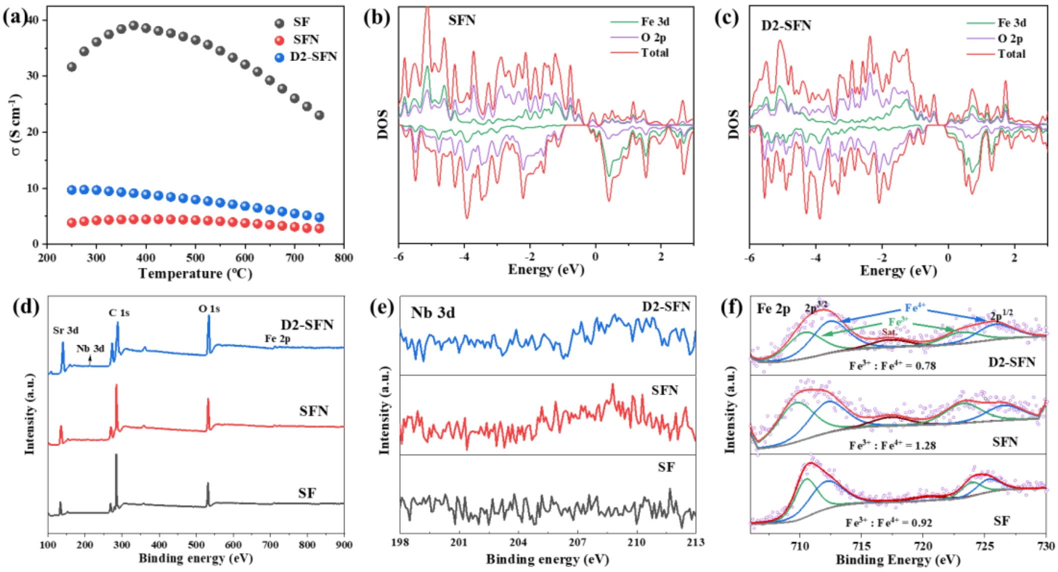

Figure 5. 5 (a) Conductivity curves of Dx-SFN samples. (b-c) Density of state (DOS) calculation of SFN and D2-SFN. (d-f) XPS spectra of Dx-SFN samples

The electrical conductivity profile of SF material exhibits remarkable temperature-dependent behavior, initially increasing with temperature likely due to thermal excitation of charge carriers, followed by a noticeable decline around 400 °C. This non-linear behavior indicates a transition from semiconducting to metallic characteristics, which is due to the lattice oxygen loss at elevated temperatures according to the following defect reaction [178]:

$$2O_O^{\times} + 4h^{\cdot} \rightarrow O_2 + 2V_O^{\cdot\cdot} \tag{5.5}$$

As temperature rises, the reduced Fe facilitates the escape of lattice oxygen, forming oxygen vacancy ($V_O^{\cdot\cdot}$) and releasing O_2. Concurrently, the electron holes ($h^{\cdot}$) were consumed, causing the decreased conductivity. Incorporating Nb led to a substantial reduction in electrical conductivity compared to the pristine SF material.

Over 250-750°C, the conductivity of SFN was only 2.82 to 4.46 S cm^{-1}, much lower than the 23.04 to 39.06 S cm^{-1} range exhibited by SF. This considerable decrease suggests that Nb^{5+} ions inhibit electron mobility in the material [179].

However, combining Nb doping and A-site deficiency in D2-SFN notably enhanced its electrical conductivity compared to SFN, doubling it to 4.79 to 9.73 S cm^{-1} over 250-750 °C. This indicates that introducing Sr vacancies can compensate for the reduced conductivity induced by Nb doping. To comprehend the mechanisms contributing to the enhanced conductivity in D2-SFN, an exploration of the electronic structures of SFN and D2-SFN was undertaken utilizing density of states (DOS) plots. After calibration, 0 eV corresponds to the Fermi level (E_f). As depicted in **Figures 5.5b-c**, the conduction band near the Fermi level is predominantly shaped by Fe 3d orbitals, while the valence band primarily originates from O 2p orbitals. This underscores the vital role of Fe-O interactions in influencing the electronic conductivity of the material. The broadening of unoccupied states around the valence band in D2-SFN implies an augmentation in charge transfer [180-181]. Introducing Sr defects leads to an increase in the Fe valence states, resulting in an amplified overlap of Fe 3d and O 2p orbitals near the Fermi level. This indicates a reinforcement of Fe-O covalency, favorably impacting electron conduction in the material [182-183]. Nonetheless, the conductivity remains inferior to that of pristine SF, highlighting the intricate interplay between doping and deficiency in influencing material properties. However, when the air electrode meets the electronic conductivity of 1 Scm^{-1}, it is enough to provide the required electron transport path for electrochemical reactions [31-32]. Therefore, the electronic conductivities of the above three electrode materials can meet the needs of high-performance air electrodes.

In addition to sufficient electronic conductivity, an ideal RePCC air electrode should also present high O^{2-}/H^+ conductivity and surface exchange performance. These properties are usually related to the B-site transition metal oxidation state, oxygen vacancy concentration, and material surface chemical properties [175]. Therefore, XPS was introduced to get information about surface chemistry and oxidation states in SF, SFN, and D2-SFN (**Figure 5.5d**). The Nb 3d peaks observed around 209 eV in the SFN and D2-SFN survey scans (**Figure 5.5e**) confirm the successful doping of Nb into the parent SF material. Deconvoluted high-resolution XPS spectra of Fe 2p reveal a mixed Fe^{3+}/Fe^{4+} valence state in all samples (**Figure 5.5f**) [184-185]. Compared with SF, the Fe valence state of SFN is significantly reduced, while the Fe valence state of D2-SFN is slightly increased. Relative Fe^{3+} and Fe^{4+} percentages were adopted to estimate δ of the surface, presented in Table S5. Nb doping induces a decrease in the δ from 0.48 in SF to 0.41 in SFN, indicating Nb incorporation reduces surface oxygen vacancies. However, A-site deficiency in D2-SFN marginally increases δ to 0.49 and is even slightly higher than that of SF.

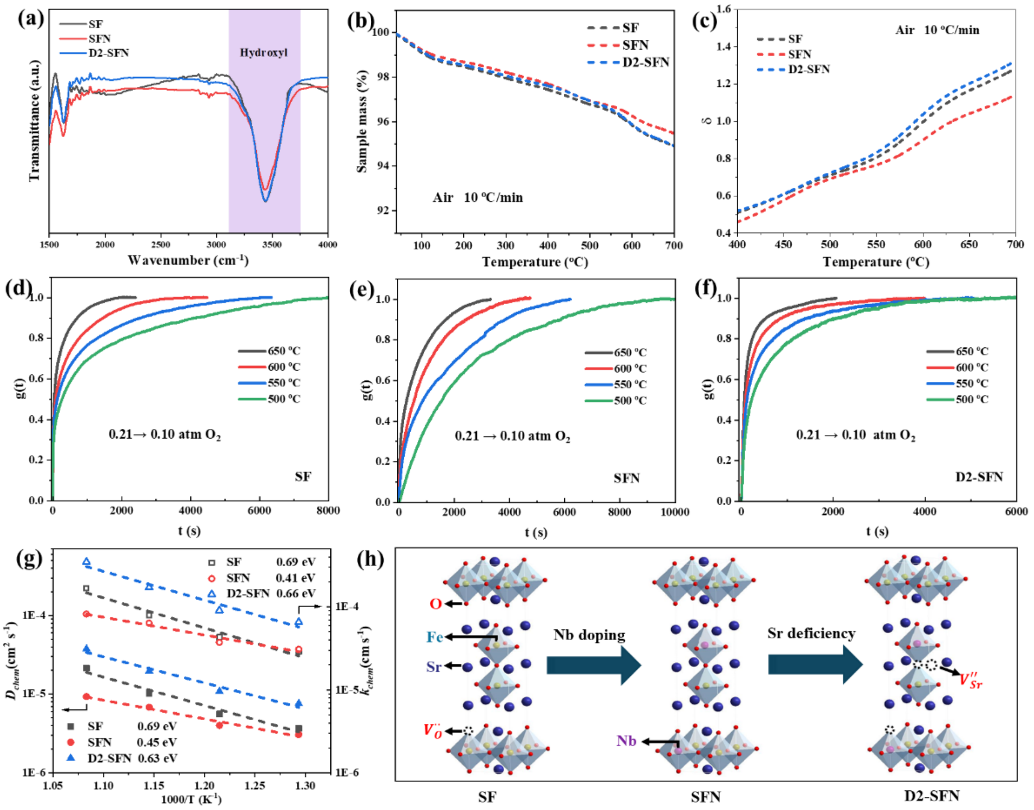

Figure 5. 6 Impact of Nb doping and Sr deficiency on Dx-SFN properties. (a) FT-IR spectra showing the hydration properties. (b) TG curves during dry air from room temperature to 700 °C. (c) Oxygen non-stoichiometry (δ) determination via TG and iodometry test. (d-f) ECR curves of Dx-SFN samples during 500-650 °C. (g) Oxygen surface exchange coefficient (k_{chem}) and D_{chem} from ECR fitting. (h) Schematic diagram of the dual modification strategy.

It is generally accepted that the air electrode of RePCC, in a humid atmosphere, undergoes hydration reactions by the combination of oxygen vacancies on the electrode surface with steam, resulting in the generation of proton defects [186-187], as indicated by the following equation:

$$H_2O + O_O^{\times} + V_O^{\cdot\cdot} \rightarrow 2OH_O^{\cdot} \qquad (5.6)$$

Therefore, the surface oxygen vacancy content is generally indicative of the material's hydration performance to some extent. It is anticipated that D2-SFN, possessing a higher concentration of oxygen vacancies due to Sr deficiency, would exhibit superior hydration performance compared to SFN. FTIR testing was employed to ascertain the hydration characteristics of SFN and D2-SFN samples. As shown in **Figure 5.6a**, both samples revealed infrared absorption peaks corresponding to $OH_O^{\cdot}$ in the range of 3200 to 3700 cm^{-1} after complete hydration (3% H_2O-air for 150 h). Similar phenomena have been observed in other perovskite air electrode materials, such as $BaCo_{0.7}Fe_{0.2}Zr_{0.1}O_{3-\delta}$ [188] and $BaCo_{0.7}Ce_{0.24}Y_{0.06}O_{3-\delta}$ [189]. The $OH_O^{\cdot}$ absorption peak in D2-SFN is more pronounced than in SFN, indicating enhanced hydration capabilities.

Considering that lattice oxygen also participates in the ORR/WOR reaction of RePCC, excellent bulk oxygen migration properties are also significant to the ORR/WOR activity of the material [190-191]. The bulk oxygen vacancy content of the materials was determined through the iodometric method. The average oxygen vacancy contents of SF, SFN, and D2-SFN are marginally higher than the surface oxygen vacancy contents, measuring 0.51, 0.46, and 0.52, respectively. Discrepancies between XPS and iodometric results could stem from variations in the valence state of the Fe element between the bulk and surface regions of the materials [192]. Compared with Fe ions in the bulk phase, Fe ions on the surface are more fully in contact with air and are more easily oxidized [193].

In addition, the lattice oxygen activity of the materials at high temperatures was investigated based on thermogravimetric analysis (TG). Shown in **Figure 5.6b**, the pronounced mass loss observed above ~400 °C in all samples has been attributed to the thermal reduction of Fe and subsequent release of lattice oxygen [80, 194], which confirms the change of the conductivity in **Figure 5.6a**.

Since RePCCs usually operate at intermediate temperatures of 400-700 °C, integrating iodometry and TG results yielded the most representative oxygen vacancy content of the air electrode material in the operational state. the oxygen vacancy evolution of SF, SFN, and D2-SFN in the corresponding operating temperature ranges is depicted in **Figure 5.6c**. Compared to SF, SFN has a lower δ value at 400-700 °C. For example, at 550 °C, the δ value for SF is 0.81, whereas for SFN, it is only 0.77. Considering that the bond strength of the Nb-O bond is significantly higher than that of the Fe-O bond, the lattice oxygen combined with Nb is more stable than that combined with Fe [195-196]. Therefore, after doping Nb, the overall activity of lattice oxygen in the bulk phase is weakened, O^{2-} ions are less likely to escape from the lattice when the temperature increases and the oxygen vacancy concentration decreases. D2-SFN has the highest δ value of 1.32 at 700 °C, which may be related to the increased lattice oxygen activity near the Sr defects.

To further evaluate the oxygen surface exchange and bulk diffusion properties of the electrode material in a real environment, the chemical bulk diffusion and surface exchange kinetics of the material when the oxygen partial pressure changes were tested through ECR experiments (**Figures 5.6d-f**). The experimental process has been given in detail in the experimental section. The Arrhenius curves of k_{chem}, and D_{chem} of the three materials at 500-650°C were plotted in **Figure 5.6g**. Compared with SF, SFN exhibits lower D_{chem} and k_{chem} values between 500-650°C, indicating that niobium doping may adversely affect bulk and surface oxygen transport [197]. The introduction of A-site defects in SFN can significantly improve the oxygen transport properties of the material. Compared to SFN, the D_{chem}, and k_{chem} of D2-SFN increased by 1.9 times and

1.7 times respectively, at 600°C. The oxygen vacancies introduced by Sr defects and the improved lattice oxygen activity effectively improve the bulk diffusion and surface exchange kinetics of SFN [198]. These ECR results highlight the efficacy of A-site vacancies in enhancing the oxygen transport capability of niobium-doped Dx-SFN compositions. The D2-SFN material possesses a higher concentration of surface and bulk oxygen vacancies and exhibits optimal surface exchange and bulk diffusion rates, which are critical properties for the ORR/WOR reactions. Consequently, D2-SFN demonstrates the most significant enhancement in electrode performance.

Based on the above discussion, the mechanism by which niobium and strontium defects manipulate material properties can be represented by the schematic diagram in **Figure 5.6h** and the following Kröger-Vink notation:

Nb doping:

$$Nb_2O_5 + V_O^{\cdot\cdot} + 2Fe_{Fe}^{\times} \rightarrow 2Nb_{Fe}^{\cdot} + O_O^{\times} + 2O_2 \tag{5.7}$$

A-site deficiency:

$$Sr_{Sr}^{\times} + O_O^{\times} \rightarrow V_{Sr}^{\prime\prime} + V_O^{\cdot\cdot} + SrO \tag{5.8}$$

$$2Fe_{Fe}^{\times} + Sr_{Sr}^{\times} + \frac{1}{2}O_2 \rightarrow V_{Sr}^{\prime\prime} + 2Fe_{Fe}^{\cdot} + SrO \tag{5.9}$$

Nb^{5+} substitution on Fe sites consumes oxygen vacancies ($V_O^{\cdot\cdot}$) for charge compensation (Equation 5.7). Introducing Sr deficiency regenerates vacancies and partially elevates Fe valence via Equations 5.8-5.9. Thereby, A-site vacancies counterbalance the Nb-induced vacancy reduction, modulating bulk transport and surface reactivity.

5.6 Stability Analysis of Symmetrical Cells

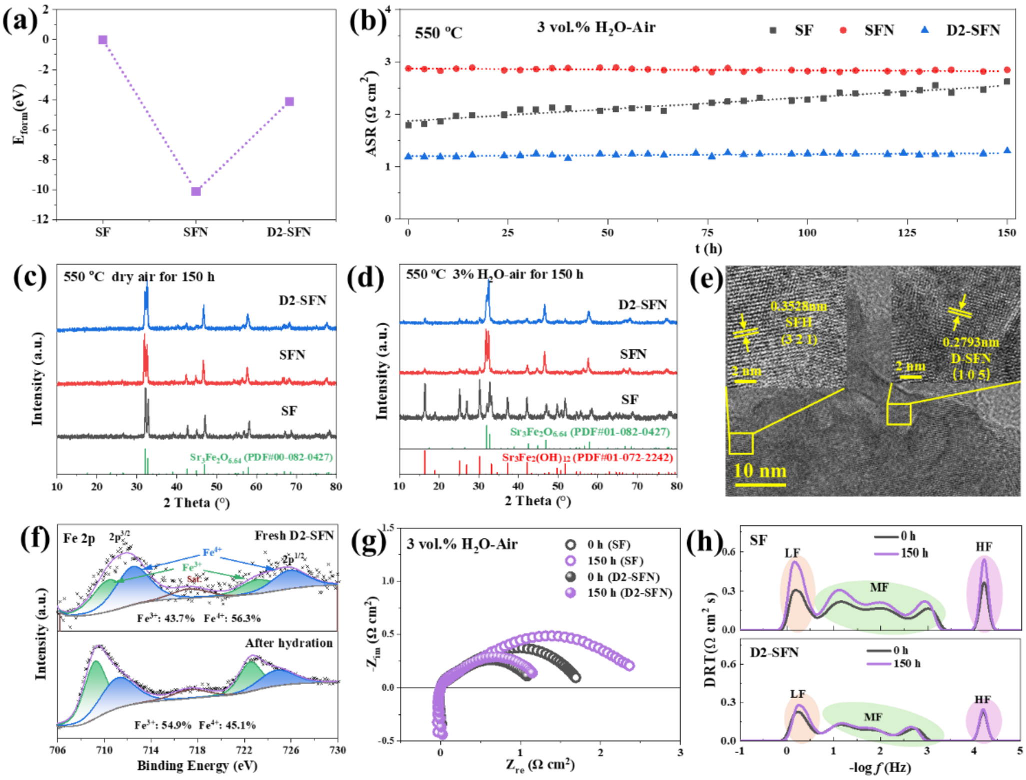

Figure 5. 7 Stability assessments of Dx-SFN electrodes. (a) Perovskite formation energy (E_{form}) of Dx-SFN. (b) ASR evolution during humid air symmetrical cell testing. (c) powder XRD processed in dry air. (d) powder XRD processed in the humid air. (e) TEM of D2-SFN powders treated in the humid air for 150 h. (f) Fe 2p XPS spectra of D2-SFN before and after hydration for 150 h. (g) EIS evolution of SF and D2-SFN electrode. (h) DRT analysis of EIS curves.

Long-term R_p tests were performed on symmetrical cells to further evaluate the stability of the D2-SFN electrode material. To facilitate the explanation of the effects of Sr defects and Nb doping, the stability of SF and SFN materials was also checked. The formation energies of the three materials were initially calculated (**Figure 5.7a**) and the calculation details can be found in the supporting information. Both SFN and D2-SFN exhibited lower E_{form} than SF, indicating that the incorporation of Nb into the Fe site enhances the stability of the perovskite. The EIS tests were then conducted in

3% H_2O-air at 550 °C for 150 h, as shown in **Figure 5.7b**. SF electrode exhibited continuously increasing ASR indicating performance degradation over time, while Nb-doped SFN and D2-SFN demonstrated negligible ASR changes, highlighting remarkably stable operation. This result confirms the variation in E_{form}, signifying that the introduction of Nb enhances the stability of the material.

To probe the origin of the performance divergence during long-term tests, the phase structure of the three materials in the air was analyzed. First, Dx-SFN powders were treated at 550 °C for 150 h in dry air to explore the phase structure evolution of the powders treated under dry air. As shown in **Figure 5.7c**, all materials maintain the initial phase structure, indicating that SF-based materials can maintain long-term phase structure stability in dry air. Phase stability was further explored under humid air for 150 h (**Figure 5.7d**). SF material underwent significant phase decomposition, forming a large amount of $Sr_3Fe_2(OH)_{12}$ (PDF#01-072-2242), which can be attributed to the extensive hydration-induced decomposition that SF underwent [199-200]. The flexible $(SrO)_2$ layers enable water incorporation, disrupting the parent lattice [201-203]. In contrast, only a small amount of the second phase appears in niobium-doped SFN and D2-SFN, confirming their excellent structural stability.

The D2-SFN powder, subjected to prolonged wet treatment, was collected for TEM analysis. As depicted in **Figure 5.7e**, the surface of the particles reveals the (115) crystal plane spacing of the D2-SFN phase and the (111) crystal plane spacing of the SFH phase. This suggests that the SFH phase forms on the surface of D2-SFN after prolonged treatment, consistent with the results in **Figure 5.7d**. Additionally, a comparison of the Fe 2p XPS spectra of D2-SFN before and after wet treatment (**Figure 5.7f**) demonstrates an increase in Fe^{3+} and a decrease in Fe^{4+}, resulting in a decrease in the average oxidation state of Fe from +3.56 to +3.45. According to the literature, in the SFH phase, Fe ions coordinate directly with OH-, exhibiting a +3-oxidation state [201]. The reduction in the average oxidation state of Fe after hydration also indirectly confirms the formation of the SFH phase.

EIS and DRT analysis (**Figures 5.7g-h**) of the deteriorating SF electrode over time provides further evidence of continuously increasing LF and MF peak resistances. Since these revelations correlate to surface and bulk processes, excessive hydration likely hinders oxygen exchange and diffusion by occupying lattice oxygen sites and vacancies [7]. While initially enhancing performance, unrestrained hydration can thus degrade long-term stability. In contrast, Nb-doped D2-SFN maintains high activity alongside exceptional steam stability by stabilizing the lattice oxygen to prevent undesirable hydroxide formation. Ultimately, elucidating the intricate effects of composition and hydration on long-term RePCC electrode performance provides invaluable guidance for designing highly stable and active air electrode materials.

The chemical compatibility of electrode candidate materials with electrolyte components is critical for long-term stable cell operation. Therefore, before the electrochemical test, the chemical compatibility of SF-based materials and BZCYYb electrolytes was examined. D2-SFN and BZCYYb were mixed and co-fired at 1050 °C for 2 h. The powder XRD results (**Figure 5.8a**) confirmed the absence of any new phases, indicating excellent compatibility. Except for the chemical compatibility, the thermal compatibility between the air electrode and electrolyte material is crucial for the practical application of a single cell. Mismatched TEC between electrolyte and electrode can induce residual stresses, leading to interfacial delamination [204].

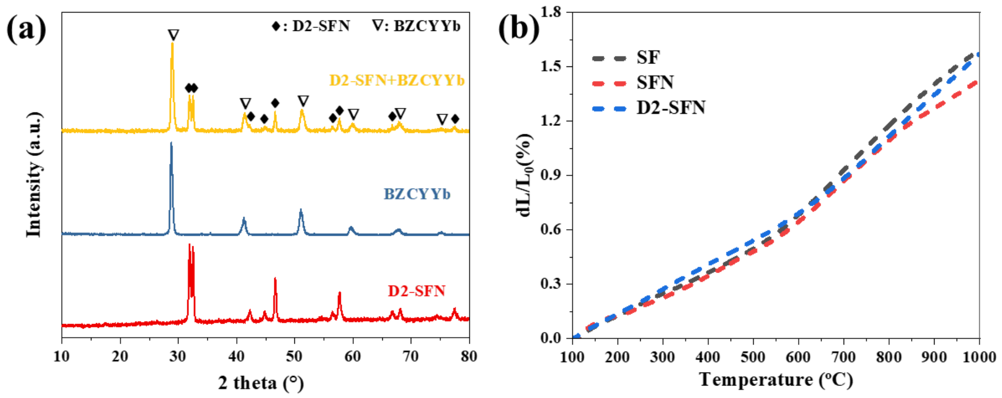

Figure 5. 8 Thermal and chemical compatibility of electrodes and electrolytes. (a) XRD patterns of the mixed powders of D2-SFN and BZCYYb. (b) Thermal expansion tests of Dx-SFN samples.

The thermal expansion behavior of the materials in the range of 30-800 °C under an air atmosphere was examined using thermal expansion tests, as shown in **Figure 5.8b**. The average TEC values for SF, SFN, and D2-SFN from room temperature to 800 °C were $18.3\cdot10^{-6}$ K^{-1}, $16.5\cdot10^{-6}$ K^{-1}, and $17.1\cdot10^{-6}$ K^{-1}, respectively, significantly lower than the thermal expansion coefficient of some typical Co-based air electrodes [205-206]. Despite Sr defects causing unit cell contraction, aiding in the improvement of the thermal expansion coefficient to some extent, the material's high-temperature expansion behavior is primarily attributed to the reduction of B-site elements and lattice oxygen loss [207-208]. At elevated temperatures, the thermal expansion coefficient of D2-SFN is slightly higher than SFN, possibly due to the greater reduction of Fe^{4+} in D2-SFN at high temperatures, as evidenced by TG and XPS results. However, it should be noted that SFN and D2-SFN exhibit very close TEC within the operational temperature range (500-750 °C), highlighting the beneficial impact of Nb incorporation. Considering the relatively low average TEC of BZCYYb ($9.5\cdot10^{-6}$ K^{-1}) [209], the introduction of Nb can decrease the thermal expansion coefficient of the SF-based air electrode, enhancing the long-term thermal compatibility with BZCYYb electrolyte during operation.

5.7 Performance and Durability of RePCCs

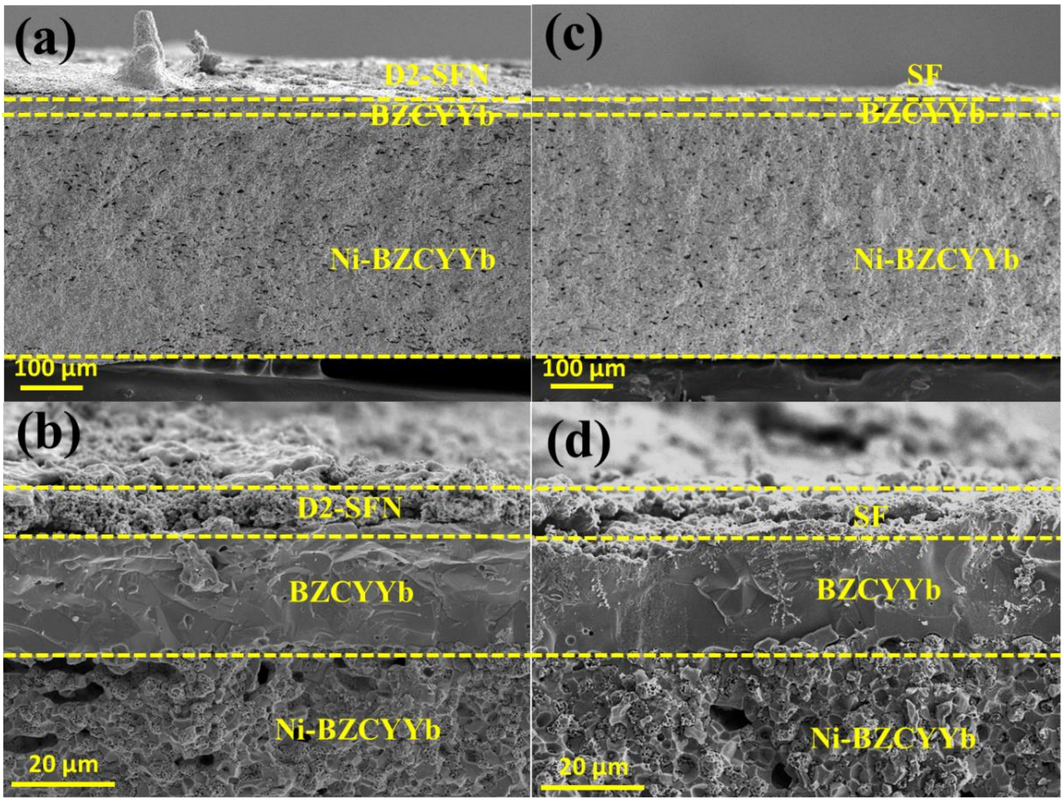

Figure 5. 9 Cross-section SEM of the single cell after test. (a-b) Single cell with D2-SFN air electrode. (c-d) Single cell with SF air electrode.

To evaluate the promising D2-SFN air electrode candidate material in a practical RePCC device, a Ni-BZCYYb fuel electrode-supported single cell was fabricated comprising a ~23 μm electrolyte and ~10 μm D2-SFN air electrode (**Figures 5.9a-b**). A single cell with the same configuration using SF as the air electrode was also prepared, which has the same electrolyte thickness as the single cell with the D2-SFN air electrode (**Figures 5.9c-d**).

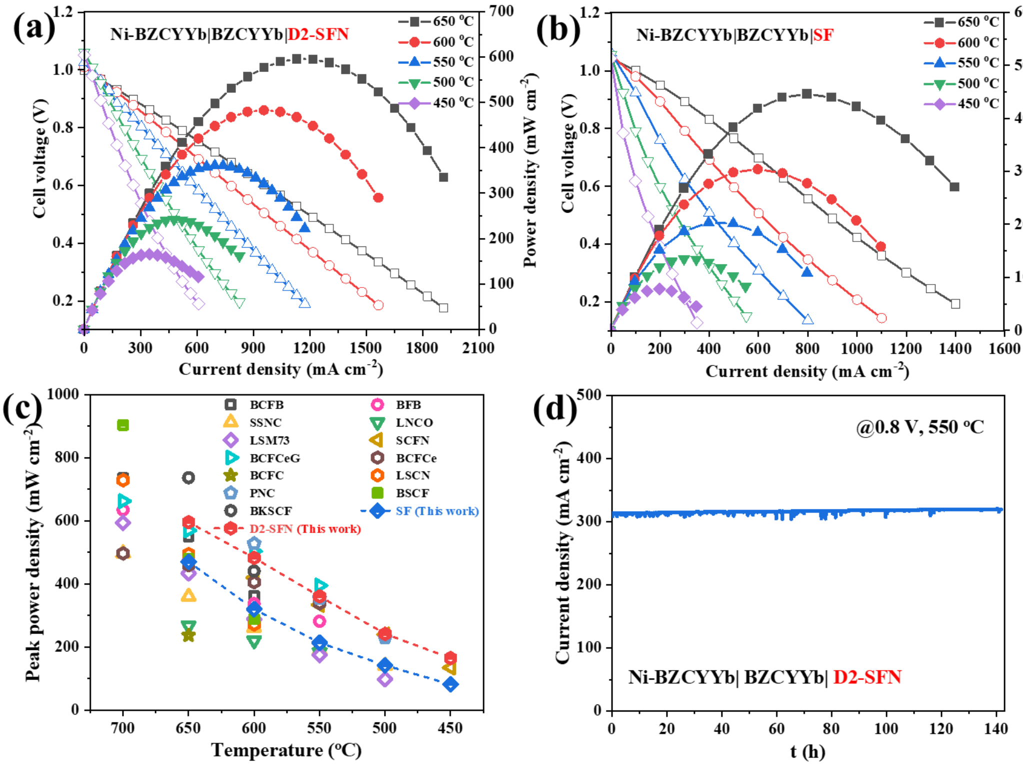

Figure 5. 10 Electrochemical performance of the single cells. (a-b) Fuel cell power density curves under H_2/ humidified air. (c) Benchmarking peak power density against recently reported high-performance PCFCs. (d) Long-term stability of D2-SFN-based cell under PCFC mode (at 0.8 V).

Fuel cell (PCFC) *i-V-P* curves (**Figure 5.10a**) exhibit exceptional peak power densities (PPD) of 596, 483, 361, 242, and 165 mW cm^{-2} from 650 to 450 °C, respectively, using H_2-humidified air feeds. This significantly outperforms the same configuration of a single cell with an SF air electrode (**Figure 5.10b**), directly confirming the optimized ORR electrocatalytic performance of the D2-SFN air electrode. The PPDs surpass numerous reported PCFCs employing advanced air electrodes (**Figure 5.10c**, **Table 5.3**), and the cell operates stably for approximately 142 h under 0.8 V (**Figure 5.10d**), highlighting the potential of D2-SFN for air electrodes in PCFCs.

Table 5. 3 Performance comparison of reported PCFC under fuel/oxidizing atmosphere of H_2/3% H_2O-air

Air electrode	Electrolyte (Thickness)	Peak power density (mW cm^{-2})						Ref.
		700 °C	650 °C	600 °C	550 °C	500 °C	450 °C	
$BaCe_{0.5}Fe_{0.3}Bi_{0.2}O_{3-\delta}$ (BCFB)	$BaZr_{0.1}Ce_{0.7}Y_{0.2}O_{3-\delta}$ (25 μm)	736	551	362	203			210
$BaFe_{0.9}Bi_{0.1}O_{3-\delta}$ (BFB)	$BaZr_{0.1}Ce_{0.7}Y_{0.2}O_{3-\delta}$ (14 μm)	635	479	338	282			211
$SrSc_{0.175}Nb_{0.025}Co_{0.8}O_{3-\delta}$ (SSNC)	$BaZr_{0.1}Ce_{0.7}Y_{0.2}O_{3-\delta}$ (46 μm)	498	361	262	190	141		163
$LiNi_{0.8}Co_{0.2}O_2$ (LNCO)	$BaZr_{0.1}Ce_{0.7}Y_{0.2}O_{3-\delta}$ (24 μm)		268	221	184			212
$La_{0.7}Sr_{0.3}MnO_{3-\delta}$ (C-LSM73)	BZCY442 (7 μm)	594	434	289	175	98		213
$Sr_{0.9}Ce_{0.1}Fe_{0.8}Ni_{0.2}O_{3-\delta}$ (SCFN)	BZCYYb1711 (26 μm)			420	334	240	135	9
$BaCo_{0.4}Fe_{0.4}Ce_{0.1}Gd_{0.1}O_{3-\delta}$ (BCFCeG)	BZCYYb1711 (30 μm)	663	570	504	395			166
$BaCo_{0.4}Fe_{0.5}Ce_{0.1}$ (BCFCe)	BZCYYb1711 (30 μm)	497	460	406	339			166
$BaCe_{0.4}Fe_{0.4}Co_{0.2}O_{3-\delta}$ (BCFC)	BZCYYb1711 (~70 μm)	335	287	237				214
$La_{1.6}Sr_{0.4}Cu_{0.6}Ni_{0.4}O_{4+\delta}$ (LSCN)	BZCYYb1711 (10 μm)	729	495	272				215
PrNi0.5Co0.5 O3-δ(PNC)	BZCYYb4411 (~10 μm)			528	354	230		216
$Ba_{0.5}Sr_{0.5}Co_{0.8}Fe_{0.2}O_{3-\delta}$ (BSCF)	BZCY172 (10 μm)	904	480	289				186
$Ba_{0.4}K_{0.1}Sr_{0.5}Co_{0.8}Fe_{0.2}O_{3-\delta}$ (BKSCF)	BZCY172 (10 μm)	1275	737	441				186
SF	BZCYYb1711 (23 μm)		470	320	214	142	82	This work
D2-SFN	BZCYYb1711 (23 μm)		596	483	361	242	165	This work

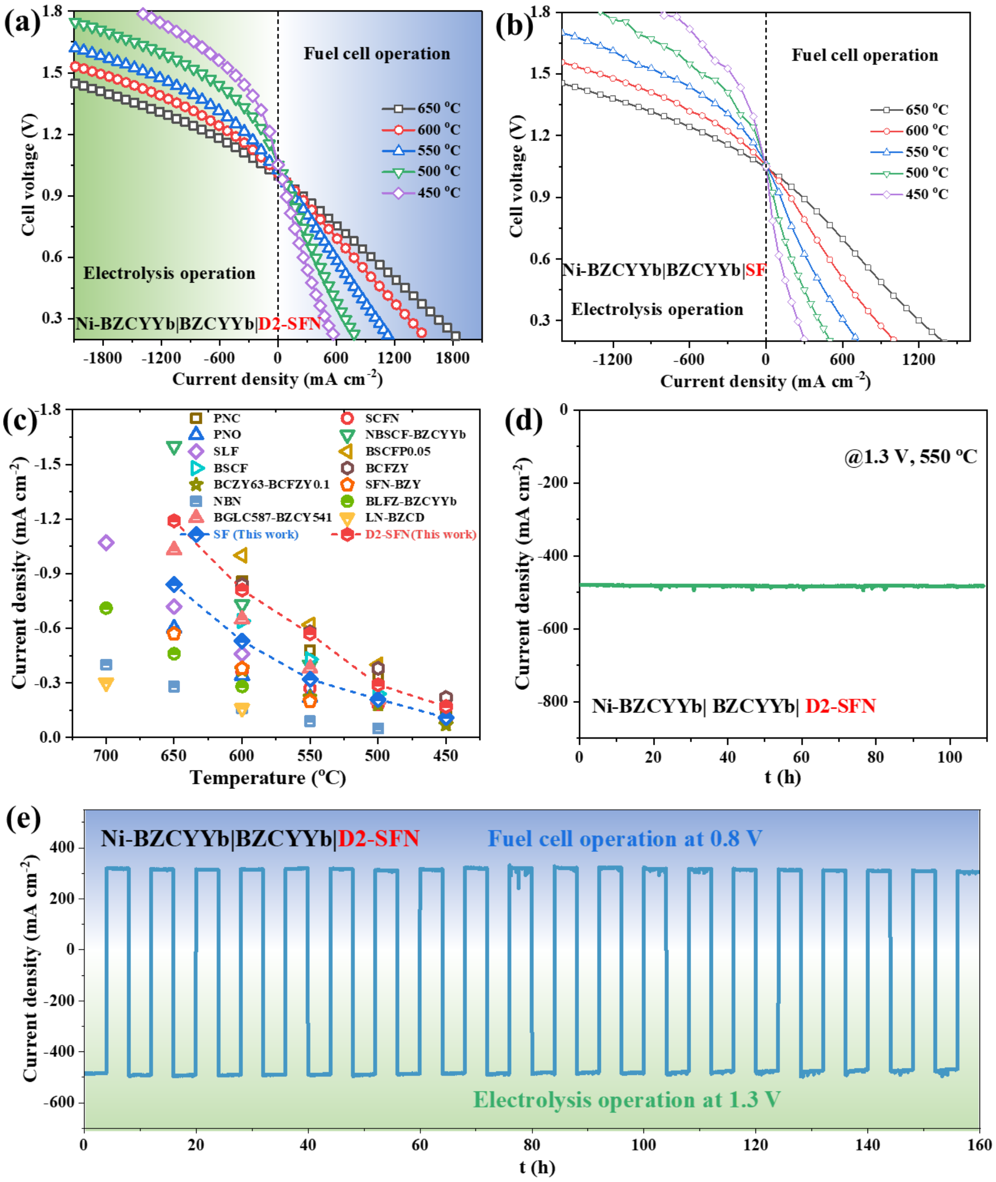

Figure 5. 11 (a-b) Polarization curves exhibiting high current density under H_2/humidified air. (c) Benchmarking electrolysis performance against state-of-the-art PCECs at 1.3 V. (d) Durability under PCEC mode (at 1.3 V). (e) Outstanding cycle stability over 160 hours with 23 reversal cycles between fuel cell (0.8 V) and electrolysis (1.3 V) modes

Besides, RePCCs can not only work in PCFC mode, but also PCEC mode, so it is vital to investigate the performance of the D2-SFN air electrode candidate in electrolysis mode (PCEC). Under electrolysis mode at 1.3 V (**Figure 5.11a**), high current densities of -0.17 to -1.19 A cm^{-2} were achieved from 450 to 650 °C, exhibiting much higher current densities than electrolysis cell with SF air electrode (**Figure 5.11b**). The performance is even comparable to cells with top-tier air electrodes (**Figure 5.11c**, **Table 5.4**). Excellent 109-h stability at 1.3 V (**Figure 5.11d**) demonstrates negligible degradation. The *i-V* curve and electrolysis stability test prove the excellent WOR activity and durability of the D2-SFN air electrode.

Table 5. 4 Performance comparison of reported proton-conducting electrolysis cells at an applied voltage of 1.3 V

Air electrode	Fuel/ Oxidant	Electrolyte	Current density @1.3 V (A cm^{-2})						Ref.
			700 °C	650 °C	600 °C	550 °C	500 °C	450 °C	
$PrNi_{0.5}Co_{0.5}O_{3-\delta}$ (PNC)	Dry H_2 /10 % H_2O-air	BZCYYb (~10 μm)			-0.86	-0.48	-0.34	-0.12	216
$Sr_{0.9}Ce_{0.1}Fe_{0.8}Ni_{0.2}O_{3-\delta}$ (SCFN)	Dry H_2/3 % H_2O-air	BZCYYb (26 μm)			-0.36	0.27	0.18	0.09	9
$Pr_2NiO_{4+\delta}$ (PNO)	Dry H_2/40 % H_2O-air	$BaZr_{0.2}Ce_{0.6}Y_{0.2}O_{3-\delta}$ (20 μm)		-0.60	-0.34	-0.22			217
$NdBa_{0.5}Sr_{0.5}Co_{1.5}Fe_{0.5}O_{5+\delta}$ (NBSCF-BZCYYb)	90%H_2-10%H_2O/10 % H_2O-air	BZCYYb (20 μm)	-2.46	-1.60	-0.73	-0.40			218
$Sr_{2.8}La_{0.2}Fe_2O_{7-\delta}$ (SLF)	3%H_2O-H_2/20 % H_2O-air	BZCY (20 μm)	-1.07	-0.72	-0.46				219

$BaCe_{0\cdot6}Zr_{0\cdot3}Y_{0\cdot1}O_{3-\delta}$ (BCZY63)-$BaCo_{0.4}Fe_{0.4}Zr_{0.1}Y_{0-1}O_{3-\delta}$ (BCFZY0.1)	3%H_2O-H_2/12%H_2O-air	$BaCe_{0.7}Zr_{0.1}Y_{0.1}Sm_{0.1}O_{3-\delta}$ (25 µm)			-0.37	-0.22	-0.18	-0.07	220
$La_2NiO_{4+\delta}$ (LN)-$BaCe_{0.5}Zr_{0.3}Dy_{0.2}O_{3-\delta}$ (BCZD)	3%H_2O-H_2/3%H_2O-air	$BaCe_{0.5}Zr_{0.3}Dy_{0.2}O_{3-\delta}$ (30 µm)	-0.30		-0.16				221
$Ba_{0.5}Sr_{0.5}(Co_{0.8}Fe_{0.2})_{0.95}P_{0.05}O_{3-\delta}$ (BSCFP0.05)	H_2/3%H_2O-air	BZCYYb (~10 µm)			-1	-0.62	-0.4		222
$Ba_{0.5}Sr_{0.5}Co_{0.8}Fe_{0.2}O_{3-\delta}$ (BSCF)	H_2/3%H_2O-air	BZCYYb (~10 µm)			-0.64	-0.43	-0.24		222
$BaCo_{0.4}Fe_{0.4}Zr_{0.1}Y_{0.1}O_{3-\delta}$ (BCFZY)	H_2/10%H_2O-air	BZCYYb (~15 µm)			-0.84	-0.58	-0.38	-0.22	24
$Ba_{0.5}Gd_{0.8}La_{0.7}Co_2O_{6-\delta}$-$BaZr_{0.5}Ce_{0.4}Y_{0.1}O_{3-\delta}$ (BGLC587-BZCY541)	20% H_2-80% N_2/30%H_2O-air	BZCY541 (~12 µm)		-1.03	-0.65	-0.38	-0.21		223
$Ba_{0.95}La_{0.05}Fe_{0.8}Zn_{0.2}O_{3-\delta}$ (BLFZ)-BZCYYb	3%H_2O-H_2/10%H_2O-air	BZCYYb (10 µm)	-0.71	-0.46	-0.28				224
$Sr_2Fe_{1.5}Mo_{0.5}O_{6-\delta}$ (SFM)-$BaZrO_3$ (BZ	H_2/3%H_2O-air	BZY (18 µm)		-0.57	-0.38	-0.20			225

Y)									
$Nd_{1.95}Ba_{0.05}NiO_{4+\delta}$ (NBN)	3% H_2O-H_2/3% H_2O-air	$BaCe_{0.5}Zr_{0.3}Dy_{0.2}O_{3-\delta}$ (15 μm)	-0.4	-0.28	-0.16	-0.09	-0.09	-0.05	[226]
SF	H_2/3% H_2O-air	BZCYYb (23 μm)		-0.83	-0.52	-0.29	-0.19	-0.11	This work
D2-SFN	H_2/3% H_2O-air	BZCYYb (23 μm)		-1.19	-0.81	-0.57	-0.29	-0.17	This work

In addition, considering the working scenario of RePCCs combined with renewable energy, it is critical to examine the reversibility of the D2-SFN air electrode, because the cell needs to switch between PCFC and PCEC modes intermittently [227]. The cell underwent alternating cycles of operation in PCFC mode (at 0.8 V) and PCEC mode (at 1.3 V) for 4 h each, totaling 20 cycles and lasting 160 h (**Figure 5.11e**). Despite repeated oxidation and reduction, only slight performance loss occurred in the D2-SFN air electrode, verifying the excellent stability of the electrode and cell reversibility.

By extensively evaluating the optimized D2-SFN air electrode material in a single-cell configuration, this work substantiates its high activity for ORR/WOR electrocatalysis along with excellent stability for practical RePCC devices. The exceptional outputs highlight the efficacy of the co-substitution approach in developing optimized electrode materials.

5.8 Conclusion

This study presents a simple A/B-sites co-substitution strategy for developing RP-type ferrite RePCC air electrodes with enhanced stability and activity. By introducing A-site Sr deficiency and Nb doping into the RP-type SF air electrode, a rationally designed D2-SFN composition is achieved. The incorporation of Nb improves structural stability but reduces oxygen vacancies and transport capabilities. Appropriate compensation of A-site deficiencies restores critical oxygen vacancies, thereby facilitating surface reactions and bulk diffusion, optimizing electrocatalytic activity and durability. Symmetrical cell studies confirm the remarkable performance of D2-SFN with negligible degradation during 150 hours of operation in humid air. In single-cell tests, the D2-SFN-based cell achieves an impressive peak power density (PPD) of 596 mW cm^{-2} in fuel cell mode at 650 °C, along with a substantial current density of -1.19 A cm^{-2} at 1.3 V in electrolysis mode using hydrogen and humidified air feeds. Additionally, the material demonstrates exceptional stability over 160 hours and 20 cycles during fuel cell-electrolysis cycling. This study establishes guiding principles for tailored oxygen vacancy engineering through integrated doping and deficiency modification, providing critical insights into balancing activity and stability in high-performance RePCC air electrodes.

CHAPTER 6 Multiphase Self-Assembled High-Efficiency Air Electrode for Reversible Protonic Ceramic Cell Application

6.1 Introduction

In the previous two chapters, two highly promising RP-type Fe-based air electrode materials were developed by balancing proton-oxygen-related properties and synergistically enhancing oxygen vacancy concentration and structural stability. However, the performance of RP-type air electrodes still falls short of state-of-the-art RePCC air electrodes. For example, advanced Fe-based cubic perovskite air electrode materials such as $Sr_{0.95}Ta_{0.1}Fe_{0.9}O_{3-\delta}$ [228], $Ba_{0.875}Fe_{0.875}Zr_{0.125}O_{3-\delta}$ [144], $Ba_{0.9}Sr_{0.05}La_{0.05}Fe_{0.8}Zn_{0.1}Y_{0.1}O_{3}$ [229], and $BaCe_{0.16}Y_{0.04}Fe_{0.8}O_{3-\delta}$ [227] achieve peak power densities exceeding 700 mW cm^{-2} at 650 °C in RePCCs. In contrast, single cells using $Sr_{3}Fe_{1.9}Nb_{0.1}O_{7-\delta}$ (SFNb0.1), $Sr_{2.8}Fe_{1.8}Nb_{0.2}O_{7-\delta}$ (D2-SFN), or other RP-type layered perovskites, such as $Nd_{1.4}Sr_{0.6}Ni_{0.9}Cu_{0.1}O_{4+\delta}$ [230], exhibit peak power densities below 0.6 W cm^{-2} under similar conditions.

Besides, although RP-type air electrodes exhibit interesting properties such as excellent hydration capability, their phase stability in humid atmospheres remains a concern. For practical applications, RePCCs are expected to have a minimum operational lifetime of 40,000 hours [28]. One of the key strategies for further development of practical RePCC air electrodes is to leverage the advantages of SF-based RP perovskite materials while maintaining the stability of the parent air electrode material.

An effective approach involves fabricating composite electrodes by mechanically mixing SF-based RP-type layered perovskites with stable secondary phase materials. Such composite air electrodes leverage the complementary properties of different conductive materials, increasing active surface sites and enhancing reaction activity. For instance, composite air electrodes prepared by mixing proton conductors like $BaCe_{0.7}Zr_{0.1}Y_{0.2}O_{3-\delta}$ [231] with traditional oxygen ion-electron conductors (MIEC) exhibit triple conduction of protons, oxygen ions, and electrons. However, physical composite materials have significant drawbacks, such as uneven mixing and weak phase connectivity, resulting in insufficient reaction activity and limited gas diffusion within the electrode [9].

The one-pot synthesis method has emerged as an attractive strategy for fabricating composite air electrodes [232]. Unlike physical mixing, this method enables in situ formation of composite materials with heterogeneous structures, effectively tuning material composition and microstructure to enhance oxygen adsorption capacity and electrochemical activity. For instance, TIEC air electrode materials based on $BaCo_{0.7}(Ce_{0.8}Y_{0.2})_{0.3}O_{3-\delta}$ form multiple conductive phases through self-assembly, demonstrating excellent performance [80]. Additionally, self-assembled nanocomposite electrodes exhibit lower polarization resistance (R_p) and superior operational stability compared to traditional mixed air electrodes, making them promising candidates for future PCFC air electrodes [233].

In this study, a series of highly active multiphase nanocomposite materials based on nominal $SrFe_{0.9-x}Nb_{0.1}Ni_xO_{3-\delta}$ (SFNNix, x=0, 0.1, 0.2, 0.3) were synthesized using a self-assembly method as candidate air electrodes for intermediate-temperature RePCCs. During high-temperature calcination, the composite material self-assembles into a mixed oxygen ion/electron-conducting cubic perovskite phase $SrFe_{1-m-n}Nb_mNi_nO_{3-\delta}$, a secondary RP layered perovskite phase $Sr_3Fe_{2-w-z}Nb_wNi_zO_{3-\delta}$, and a NiO phase. By controlling the Ni doping level, the phase proportion of the self-assembled materials can be tailored, enabling manipulation of air electrode performance.

Under RePCC operating conditions, the cubic perovskite phase primarily conducts oxygen ions and electrons, maintaining structural stability and providing major ORR/WOR reaction sites. The RP phase exhibits excellent hydration properties, forming proton defects and facilitating proton conduction, thus expanding the active reaction sites within the electrode. The NiO ionic conducting phase further promotes oxygen adsorption and dissociation on the electrode surface. The nanoscale intimate contact between phases provides abundant electrochemical reaction sites, while the complementary properties of each phase endow the composite material with superior electrochemical performance required for RePCC air electrodes.

6.2 Material Synthesis

SFNNix (x=0, 0.1, 0.2, 0.3) is prepared using the sol-gel method. Stoichiometric amounts of $Sr(NO_3)_2$, $Fe(NO_3)_3 \cdot 9H_2O$, $C_{10}H_5NbO_{20}$, and $Ni(NO_3)_2 \cdot 6H_2O$ are dissolved in deionized water along with citric acid and EDTA. Ammonia solution is then added to adjust the pH to slightly alkaline. The solution is heated to evaporate the solvent until a gel forms, which is subsequently transferred to an oven and treated at 180 °C for 10 hours to obtain the precursor. The collected powder is then calcined at 950 °C for 5 hours to obtain the initial SFNNix powder.

6.3 Phase Composition and Morphology

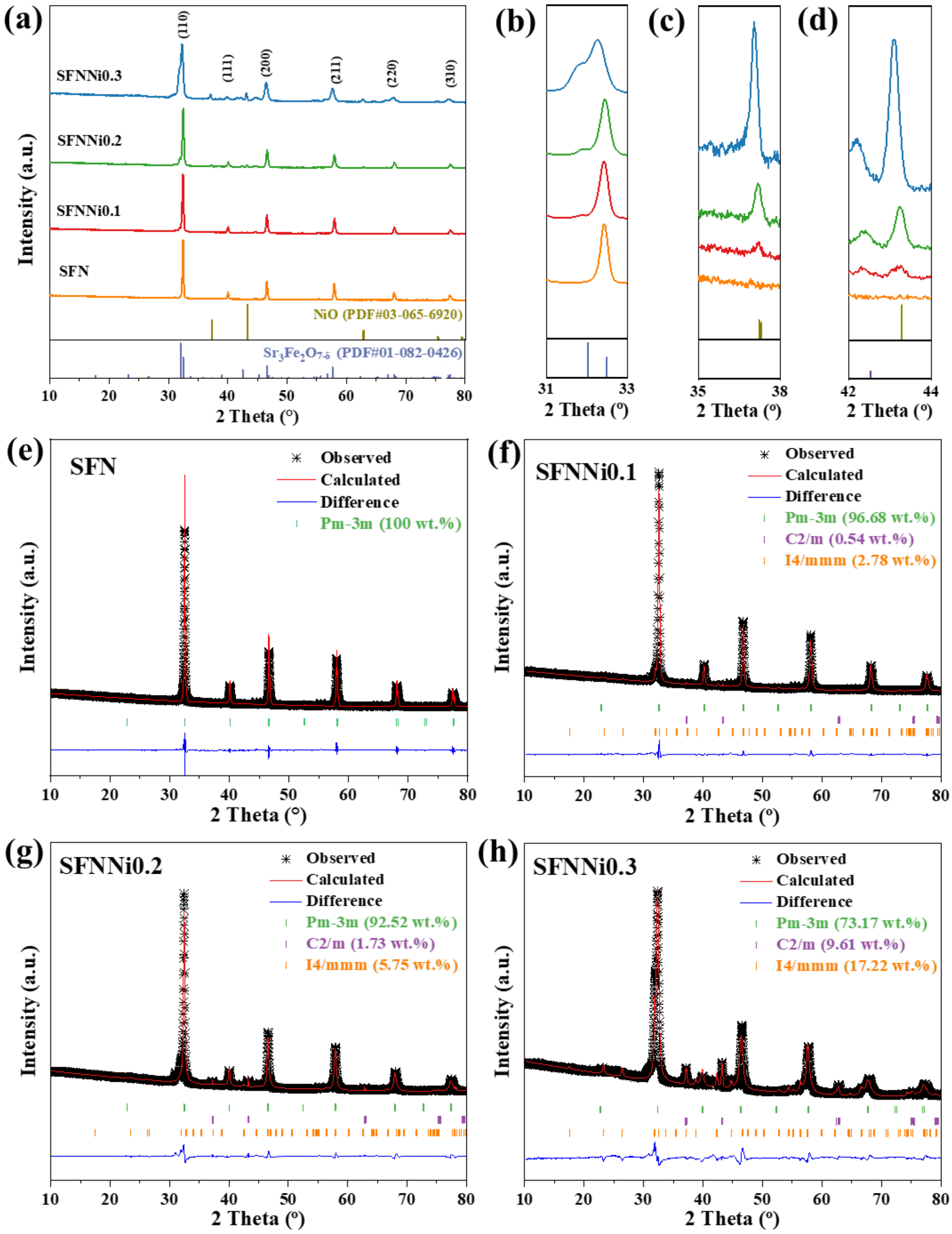

Figure 6. 1 Phase composition of SFNNix (x=0, 0.1, 0.2, 0.3) materials. (a-d) XRD and partial enlargement of fresh samples. (e-h) Refined XRD patterns of materials.

As shown in **Figure 6.1a**, four powders, namely SFN, SFNNi0.1, SFNNi0.2, and

SFNNi0.3, are synthesized using a one-pot method. The fresh samples primarily exhibit a cubic perovskite phase with a Pm-3m space group (PDF#00-034-0638). With the introduction of Ni, secondary phases are observed in the materials and identified as the C2/m monoclinic NiO phase (PDF#03-065-6920) and the I4/mmm tetragonal Ruddlesden-Popper (RP) perovskite phase (PDF#01-082-0426). As the Ni doping level increases, the peak intensities of the NiO and RP phases gradually increase (**Figures 6.1b-d**).

Table 6. 1 The XRD refinement results of SFNNix materials.

Lattice parameter	SFN	SFNNi0.1	SFNNi0.2	SFNNi0.3
R_p	4.87	4.30	5.79	6.52
R_{wp}	7.80	5.90	9.04	9.06
χ^2	0.035	0.0245	0.0623	0.107
Phase 1: Pm-3m				
a/b/c (Å)	3.892627	3.88697	3.89972	3.91546
Percentage (wt. %)	100	96.68	92.52	73.17
Phase 2: C2/m				
a (Å)	-	5.11442	5.11398	5.12596
b (Å)	-	2.95804	2.95819	2.97031
c (Å)	-	2.95366	2.95220	2.95507
Percentage (wt. %)	0	0.54	1.73	9.61
Phase 3: I4/mmm				
a/b (Å)	-	3.87876	3.86391	3.89603
c (Å)	-	20.17484	20.32502	20.24994
Percentage (wt. %)	0	2.78	5.75	17.22

Refinement of the XRD patterns for the four materials (**Figures 6.1d-g** and **Table 6.1**) reveals the weight fractions of different phases. The undoped SFN sample exhibits 100 wt.% of the cubic perovskite phase. With the incorporation of Ni, SFNNi0.1 contains 0.54 wt.% of the NiO phase and 2.78 wt.% of the RP phase, indicating that Ni is not fully incorporated into the primary lattice and partially segregates as oxides. The segregation of NiO results in a deficiency of B-site cations in the bulk material. When the defect concentration exceeds the solubility limit of the lattice, part of the cubic perovskite phase transforms into the RP phase [234]. Higher Ni doping notably increases the NiO and RP phase contents, reaching 1.73 wt.% and 5.75 wt.% in SFNNi0.2, and 9.61 wt.% and 17.22 wt.% in SFNNi0.3, respectively.

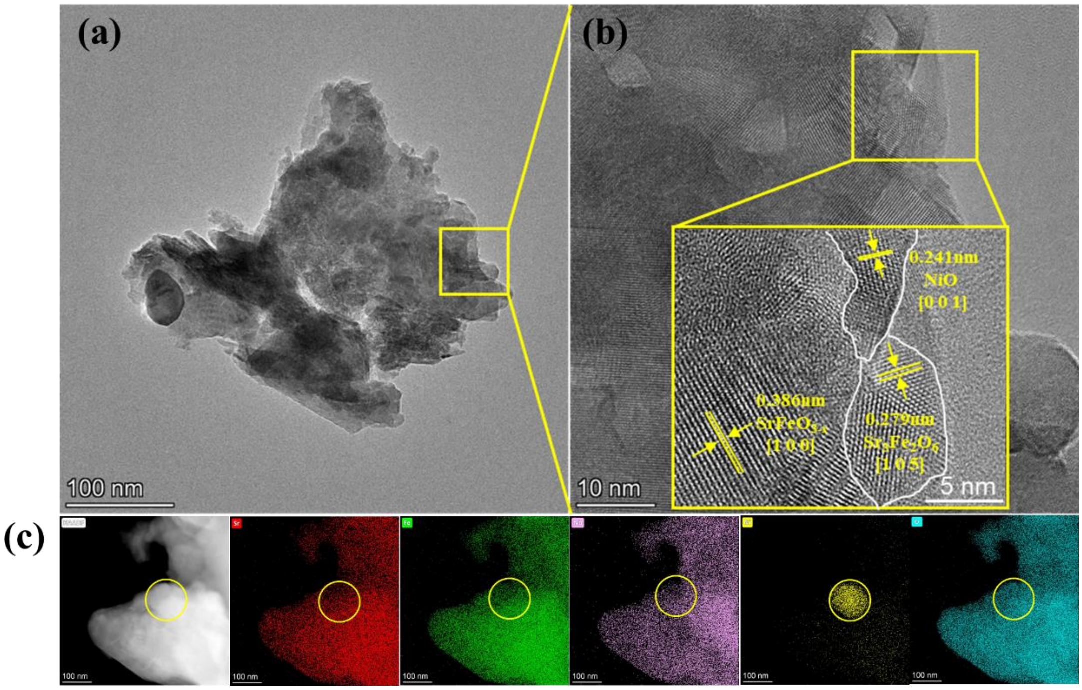

Figure 6. 2 Micro-morphology of SFNNi00.2. (a-b) TEM images, (c) HAADF-EDX mapping.

The microstructure of the material is analyzed. Taking SFNNi0.2 as an example, TEM images reveal that the particle diameter of SFNNi0.2 is approximately 100 nm (**Figure 6.2a**). In the high-magnification TEM inset (**Figure 6.2b**), the edges of the SFNNi0.2 sample exhibit distinct lattice fringes. Near the surface, lattice fringes of 0.241 nm and 0.279 nm correspond to the [001] crystal plane of the NiO phase and the [105] crystal plane of the $Sr_3Fe_2O_{7-\delta}$ phase, respectively, while the 0.386 nm fringe in the bulk phase corresponds to the [100] crystal plane of the $SrFeO_{3-\delta}$ phase. This indicates the presence of NiO and RP phases on the surface of SFNNi0.2. The elemental distribution on the surface of the SFNNi0.2 sample is analyzed using HAADF-EDX mapping to identify phase composition and distribution, as shown in **Figure 6.2c**. Sr, Fe, Nb, and O elements are uniformly distributed in the bulk phase of SFNNi0.2, while Ni is aggregated in particulate form, further confirming the presence of the NiO phase in SFNNi0.2. Typically, NiO contributes to surface exchange processes, while the RP phase is known for its excellent hydration properties [13]. The presence of NiO and RP phases is expected to promote the ORR/WOR reactions in the air electrode.

6.4 Electrochemical properties

The electrochemical performance of four electrodes is evaluated using symmetrical cell tests at 500–700 °C in a 3% H_2O-air atmosphere, with BZCYYb as the electrolyte. **Figure 6.3a** compares the EIS curves of the four symmetrical cells at 550 °C, with the ohmic resistance set to zero for a more intuitive reflection of the R_p of the four electrodes. With the introduction of Ni, the R_p gradually decreases. At 550 °C, the R_p values of the SFN, SFNNi0.1, SFNNi0.2, and SFNNi0.3 electrodes are 1.39, 1.30, 0.95, and 1.08 Ω cm^2, respectively, indicating that the presence of NiO and the RP phase contributes positively to performance improvement. However, further increasing the NiO and RP phase composition in the material slightly reduces electrode performance, as evidenced by the slightly higher R_p of the SFNNi0.3 electrode (1.08 Ω cm^2) compared to SFNNi0.2 at 550 °C. The SFNNi0.2 electrode exhibits the best ORR/WOR performance at 550 °C.

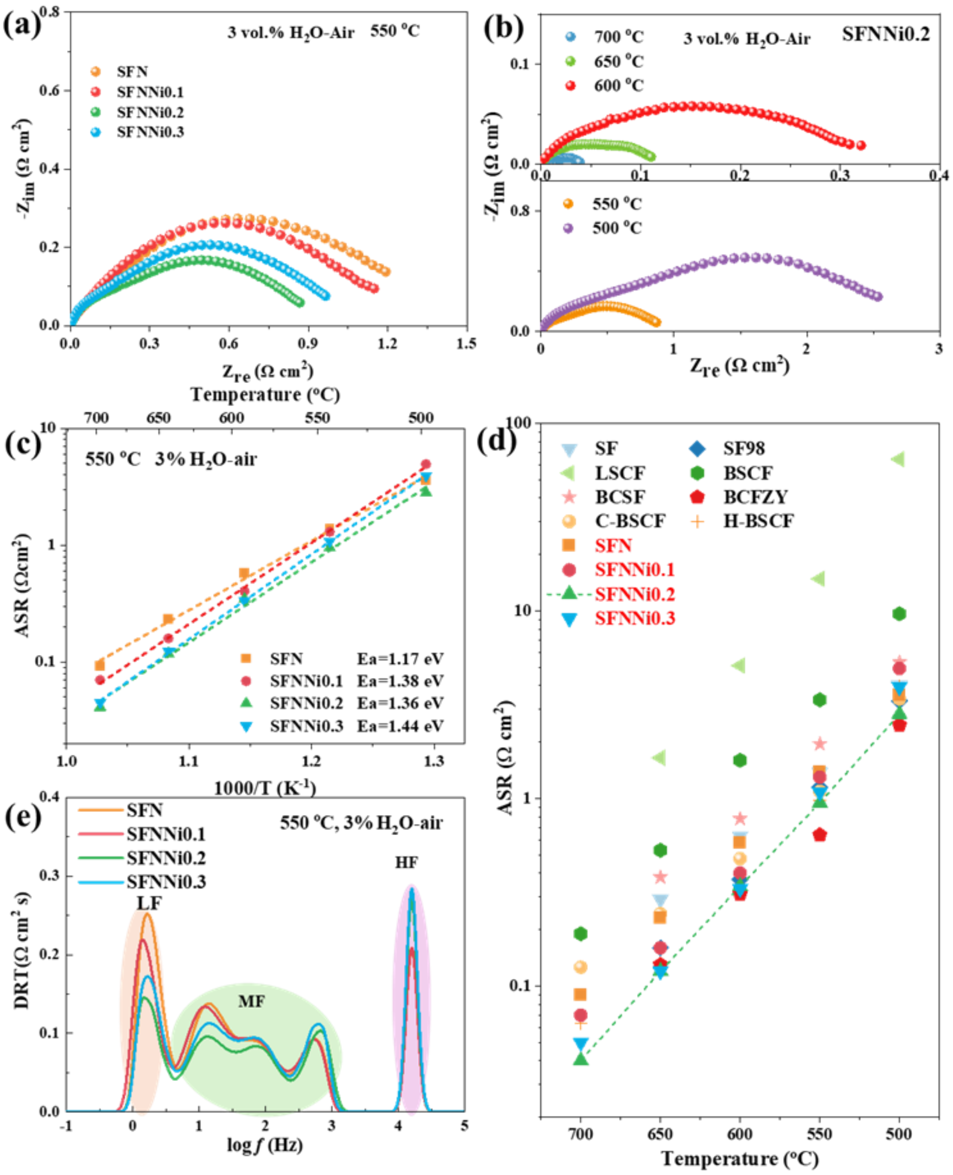

Figure 6. 3 Electrochemical performance of symmetrical cells with SFNNix as electrodes and BZCYYb as electrolyte. (a) EIS spectra of the four electrodes in 3% H_2O-air at 550 °C. (b) EIS curves of the SFNNi0.2 electrode in the temperature range of 500-700 °C. (c) Arrhenius plots of the four electrodes in the temperature range of 500-700 °C. (d) Performance comparison of the SFNNi0.2 electrode in a 3% H_2O-air atmosphere with reported air electrodes. (e) Elemental reaction processes analyzed by DRT based on EIS.

With increasing temperature, the performance of the SFNNi0.2 electrode improves significantly, with its Rp decreasing from 2.82 Ω cm^2 at 500 °C to 0.04 Ω cm^2 at 700 °C (**Figure 6.3b**). Additionally, the Arrhenius plot shows that SFNNi0.2

demonstrates the best ORR/WOR performance across the tested temperature range (**Figure 6.3c**), outperforming many reported cobalt-based electrodes (**Figure 6.3d** and **Table 6.2**).

Table 6. 2 Comparison of the performance of the SFNNix electrodes in 3% H_2O-air with other reported advanced electrodes.

Electrode	Electrolyte	ASR (Ωcm^2)					Ref.
		700 °C	650 °C	600 °C	550 °C	500 °C	
SF	BZCYYb		0.29	0.63	1.38	4.02	9
SF98	BZCYYb		0.16	0.37	1.15	3.31	9
LSCF	BZCYYb	0.09	0.24	0.51	1.45	3.89	235
BCSF	BZCYYb		0.38	0.78	1.95	5.32	159
BSCF	BZCYYb	0.19	0.53	1.60	3.36	9.66	157
BCFZY	BZCYYb		0.13	0.31	0.64	2.47	80
C-BSCF	BZCYYb	0.126	0.243	0.478	1.093	3.39	236
H-BSCF	BZCYYb	0.063	0.117	0.343	0.979	4.00	236
SFN	BZCYYb	0.09	0.23	0.58	1.39	3.56	This work
SFNNi0.1	BZCYYb	0.07	0.16	0.40	1.30	4.94	This work
SFNNi0.2	BZCYYb	0.04	0.12	0.34	0.95	2.82	This work
SFNNi0.3	BZCYYb	0.05	0.12	0.33	1.08	3.93	This work

Note: SF: $SrFeO_{3-\delta}$; SF98: $Sr_{0.9}Fe_{0.8}O_{3-\delta}$; LSCF: $La_{0.6}Sr_{0.4}Co_{0.2}Fe_{0.8}O_{3-\delta}$; BCSF: $BaCe_{0.4}Sm_{0.2}Fe0.4O_{3-\delta}$; BCSF: $Ba_{0.5}Sr_{0.5}Co_{0.8}Fe_{0.2}O_{3-\delta}$; BCFZY: $BaCo_{0.4}Fe_{0.4}Zr_{0.1}Y_{0.1}O_{3-\delta}$; C-BSCF: $Ba_{0.5}Sr_{0.5}Co_{0.8}Fe_{0.2}O_{3-\delta}$; H-BSCF: $Ba_4Sr_4(Co_{0.8}Fe_{0.2})_4O_{16-\delta}$.

The EIS curves of SFNNix electrodes are deconvoluted using the DRTTOOLS to obtain sub-step information of the ORR/WOR reaction [152]. As shown in **Figure 6.3e**, all four electrodes exhibit five characteristic peaks in the frequency range of 10^5 to 10^{-1} Hz. Among these, the low-frequency (LF) peak corresponds to gas diffusion and surface adsorption processes, the mid-frequency (MF) peaks correspond to surface exchange and bulk diffusion processes, and the high-frequency (HF) peak corresponds to ion transport across the membrane[237-239]. The area of each characteristic peak represents the resistance of the respective electrochemical sub-process.

The MF peaks dominate the total peak area for all four electrodes, indicating that surface exchange and bulk diffusion processes are the rate-determining steps of the electrode reaction. The performance improvement of the SFNNi0.2 component is primarily attributed to the reduced resistance in low-frequency and mid-frequency processes, suggesting that the increased RP phase and NiO phase effectively lower the resistance of surface exchange and bulk mass transfer processes. The surface NiO likely optimizes the oxygen surface exchange process, while the RP phase facilitates bulk proton diffusion [9, 240]. Compared to SFNNi0.2, the low- and mid-frequency resistance of SFNNi0.3 slightly increases, indicating that excessive NiO and RP phases negatively affect surface and bulk processes.

Additionally, the increased high-frequency process resistance in the multiphase components suggests partial obstruction of proton transmembrane transport, possibly due to the partial distribution of NiO within the bulk phase or at the triple-phase boundary, as NiO is an oxide-ion-conducting material [241]. Nevertheless, the high-frequency peak is not the rate-determining step of the electrode reaction, and the increase in resistance is limited. Therefore, the overall performance of the multiphase material remains superior to that of the SFN component.

The effects of oxygen and water vapor partial pressures on the performance of the SFNNi0.2 electrode are also tested to further elucidate the electrochemical sub-steps. Under humid conditions at 550 °C, with N_2 as the balance gas, the Rp of the SFNNi0.2 electrode decreases significantly as the oxygen partial pressure increases (**Figure 6.4a**).

Combined with DRT analysis (**Figure 6.4b**), it is observed that oxygen partial pressure primarily influences the low-to-mid frequency processes, confirming the involvement of oxygen exchange and oxygen ion transport in these steps.

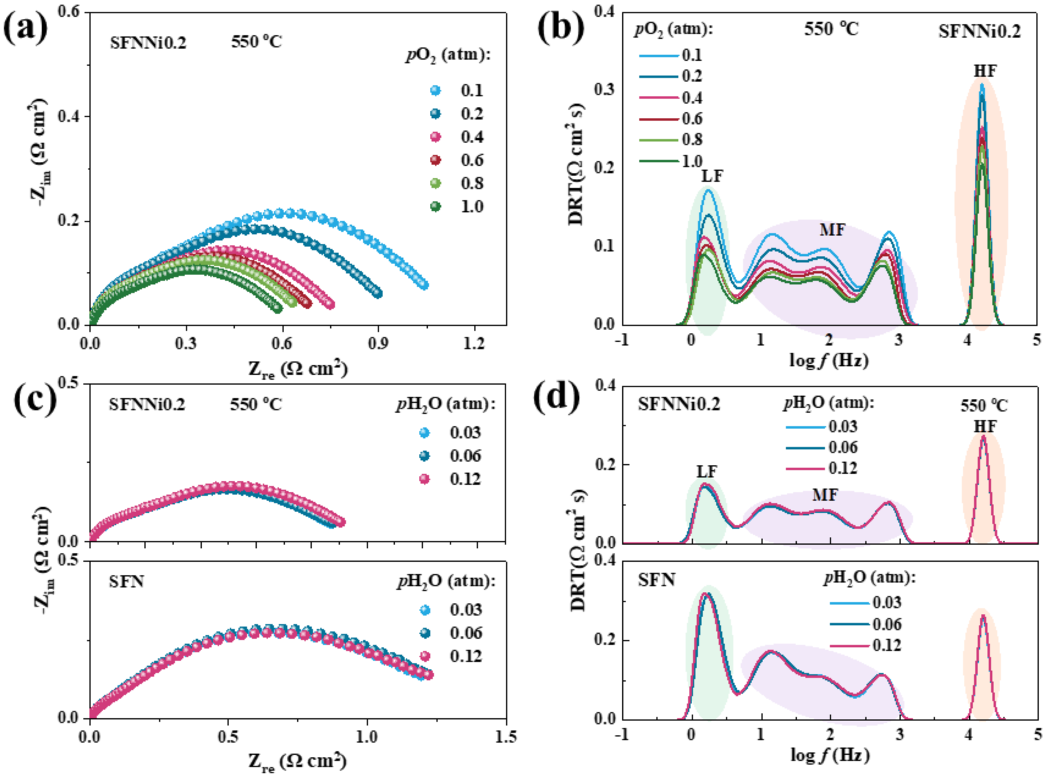

Figure 6. 4 Electrochemical performance of SFNNix/BZCYYb/SFNNix (x=0, 0.2) symmetrical cells under different oxygen and water vapor pressures. (a) EIS spectra and (b) DRT analysis of SFNNi0.2 electrode under varying oxygen pressures. (c) EIS spectra and (d) DRT analysis of SFN and SFNNi0.2 electrodes under varying water vapor pressures.

Figures 6.4c-d illustrate the effects of water vapor partial pressure on the performance of SFNNi0.2 and SFN electrodes. As the water vapor partial pressure increases from 0.03 atm to 0.12 atm, the polarization resistance of SFN gradually increases. In contrast, the polarization resistance of SFNNi0.2 remains unchanged as the vapor pressure increases from 0.03 atm to 0.06 atm and only slightly increases at 0.12 atm, indicating superior water retention capabilities, likely attributed to the presence of the RP phase.

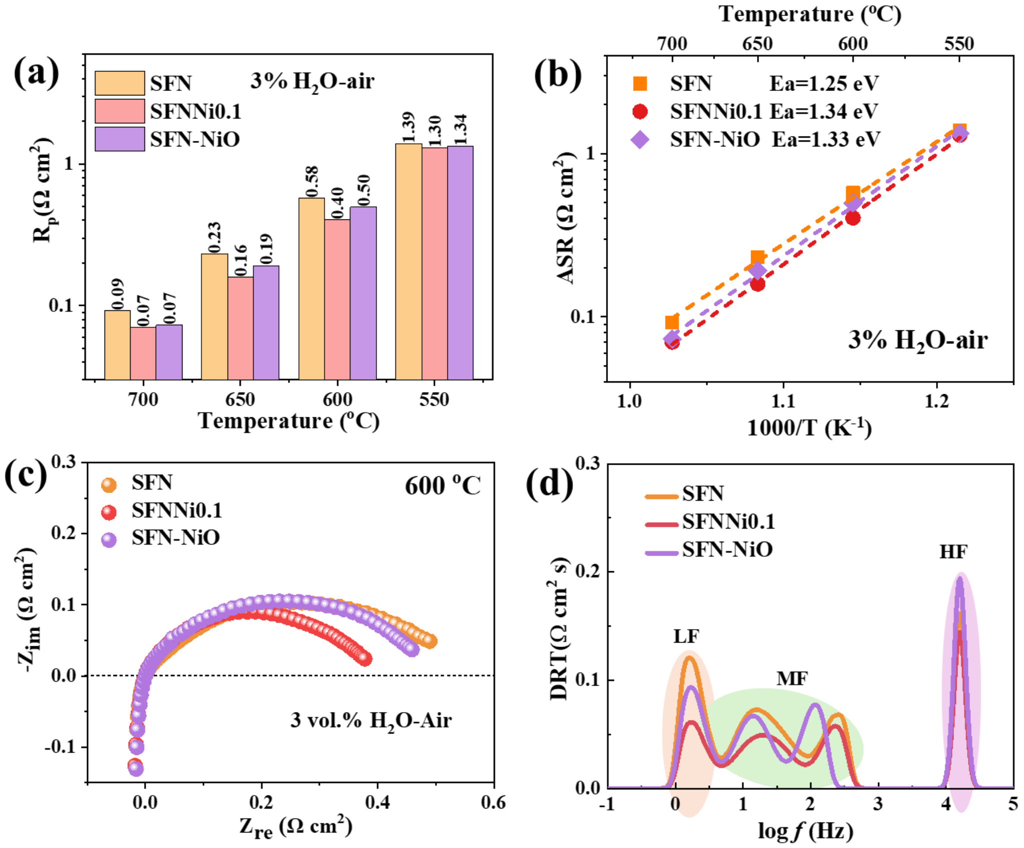

Figure 6. 5 Comparison of the performance of the composite SFN-NiO electrode with SFN and SFNNi0.1. (a) Polarization resistance of the electrodes at 550-700 °C. (b) Arrhenius plots. (c) EIS curves at 600 °C. (d) DRT analysis curves.

To distinguish the contribution of NiO and the RP phase to the performance enhancement of air electrodes, a composite SFN-NiO electrode was prepared by mechanical milling, and the performance of SFN, SFNNi0.1, and the composite SFN-NiO electrode was compared. The SFN-NiO electrode was fabricated by thoroughly mixing 99 wt.% SFN powder with 1 wt.% NiO. **Figures 6.5a-b** present the polarization resistance values and Arrhenius curves of the three electrodes in 550–700 °C. Compared with SFN, the R$_p$ value of the SFN-NiO electrode is significantly reduced, indicating that even 1 wt.% NiO enhances the electrode performance. On the other hand, the Rp value of SFNNi0.1 is lower than that of SFN-NiO, suggesting that the RP phase promotes the ORR/WOR performance of the electrode. At 600 °C, the polarization resistance of the SFN, SFNNi0.1, and SFN-NiO electrodes is 0.58, 0.40, and 0.50 Ω cm^2, respectively (**Figure 6.5c**). **Figure 6.5d** displays the DRT analysis results. Compared with SFN, the introduction of NiO in the SFN-NiO electrode mainly improves the low-frequency process while slightly increasing the resistance of the high-frequency process. A comparison of the performance of SFN-NiO and SFNNi0.1 electrodes reveals that the RP phase improves both the low-frequency and mid-frequency sub-steps.

6.5 Surface and Bulk Properties

The hydration properties of $SFNNi_x$ samples are investigated through TG curves, as shown in **Figures 6.6a-b**. The TG curves of fresh samples are measured from room temperature to 900 °C. The weight loss percentages of SFN, SFNNi0.1, SFNNi0.2, and SFNNi0.3 are 98.46%, 97.87%, 96.97%, and 96.46%, respectively. Subsequently, the SFNNix powders are exposed to 3% H_2O-air at 550 °C for 20 hours to ensure full hydration. The samples are then annealed at 150 °C in dry air to remove surface-adsorbed water until cooled to room temperature [9]. The TG curves of the hydrated samples are presented in **Figure 6.6b**. The weight loss difference of the SFNNix samples under dry and humid atmospheres represents the mass of hydration water, as shown in **Figure 6.6c**. Across the entire temperature range, the hydration water content increases with the addition of NiO and the RP phase, rising from 0.06 wt.% for SFN to 0.94 wt.% for SFNNi0.3, indicating an enhancement in hydration capacity. Furthermore, as shown in the FT-IR spectra in **Figure 6.6d**, the -OH absorption peak at 3350-3750 cm^{-1} intensifies with the increasing proportion of NiO and the RP phase, further corroborating the TG results. Considering that the NiO phase is an O^{2-}-conducting phase, the enhancement in hydration performance is likely attributed to the increased proportion of the RP phase [189, 216]. Previous studies have shown that the RP phase perovskite with a unique layered structure exhibits excellent hydration performance, which is usually the basis for proton bulk diffusion [10, 242].

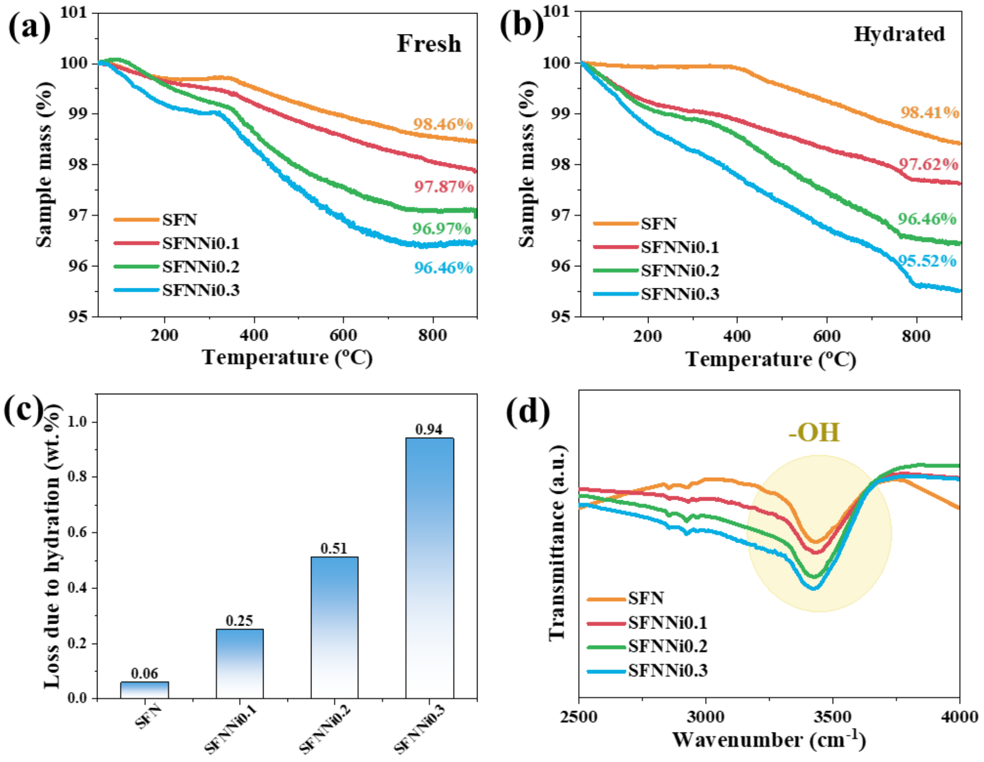

Figure 6. 6 Surface hydration performance of SFNNix materials. (a) TG curves of fresh samples. (b) TG curves of the hydrated samples. (c) Weight loss due to hydrated water. (d) FT-IR results of the hydrated samples.

SFNNix bar samples are prepared, and their oxygen surface exchange and bulk diffusion kinetics are investigated using ECR testing. These tests are conducted in the temperature range of 500–650 °C, with the testing atmosphere switching from 21% O_2-79% N_2 to 10% O_2-90% N_2. The relaxation curves are recorded using an electrochemical workstation, as shown in **Figures 6.7a-d**. Compared to SFN, the stabilization time of the Ni-doped samples is significantly shortened. By fitting the relaxation curves using ECRTOOLS, the oxygen surface exchange and bulk diffusion coefficients at 500–650 °C are obtained [135], as shown in **Figures 6.7e-f**.

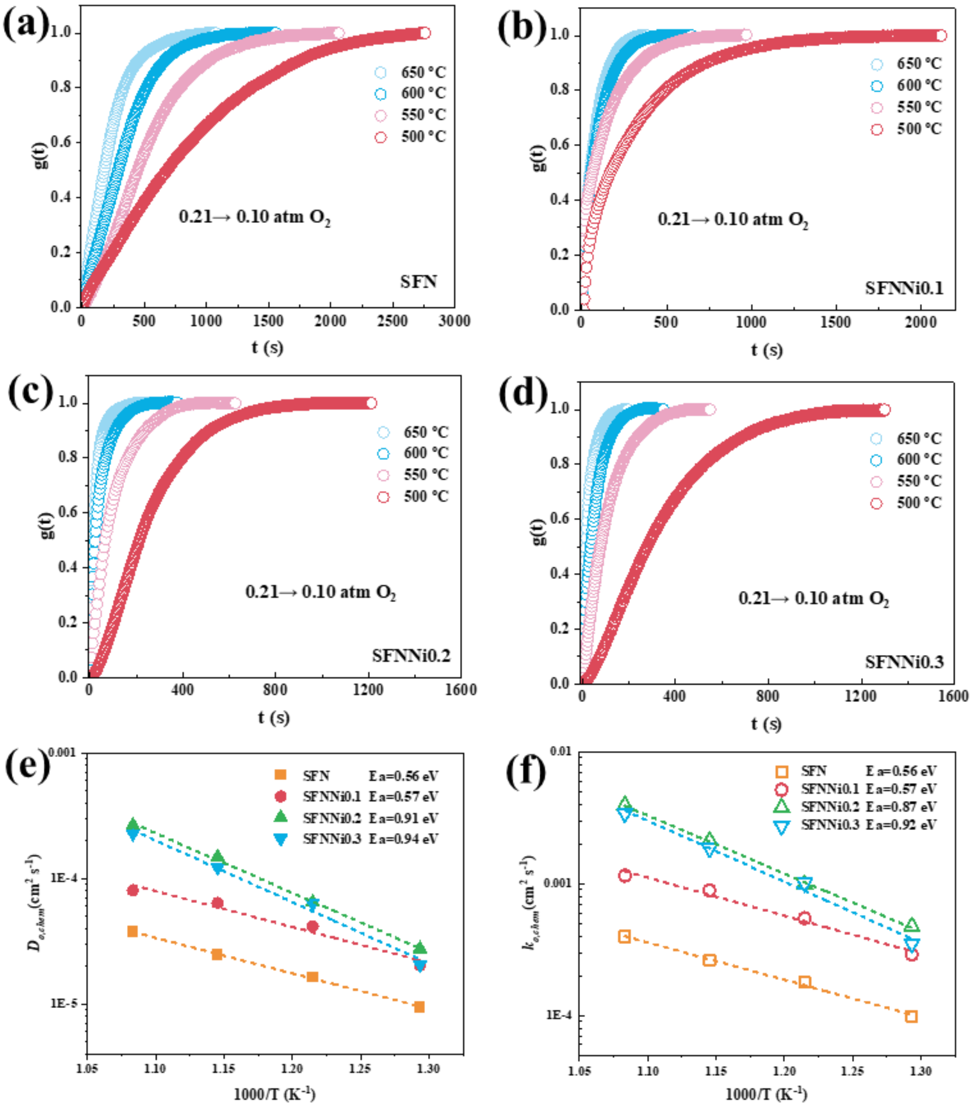

Figure 6. 7 Oxygen surface exchange and transport properties of SFNNix. (a-d) ECR curves for the transition from 79% N_2-21% O_2 to 90% N_2-10% O_2. (e) Corresponding bulk oxygen diffusion coefficients and f oxygen surface exchange coefficients.

The increased proportions of the RP phase and NiO phase enhance the oxygen surface exchange and bulk diffusion rates of the material. However, when the Ni doping level exceeds 0.2, the oxygen transport performance slightly decreases. SFNNi0.2 exhibits the best oxygen surface exchange and bulk diffusion kinetics. The phase structure and composition of the material greatly influence its mass transport and surface properties [243].

Based on previous analyses, NiO and the RP phase tend to segregate on the surface of Ni-doped samples. Numerous studies indicate that the NiO phase on the electrode surface serves as an oxygen adsorption site, facilitating oxygen surface exchange [244-245]. Additionally, bulk NiO contributes to bulk O^{2-} diffusion. Therefore, the oxygen surface exchange and bulk ionic transport performance improve with the increase in Ni content.

On the other hand, NiO is a poor electronic conductor [246-247]. While it promotes oxygen adsorption on the surface, it is unfavorable for oxygen reduction. As a result, excessive NiO coverage on the material's surface may reduce its oxygen surface exchange and bulk diffusion performance. Consequently, SFNNi0.3, which contains approximately 10 wt.% NiO, exhibits slightly inferior oxygen-related performance compared to SFNNi0.2, which contains 2 wt.% NiO.

6.6 Material Stability Test

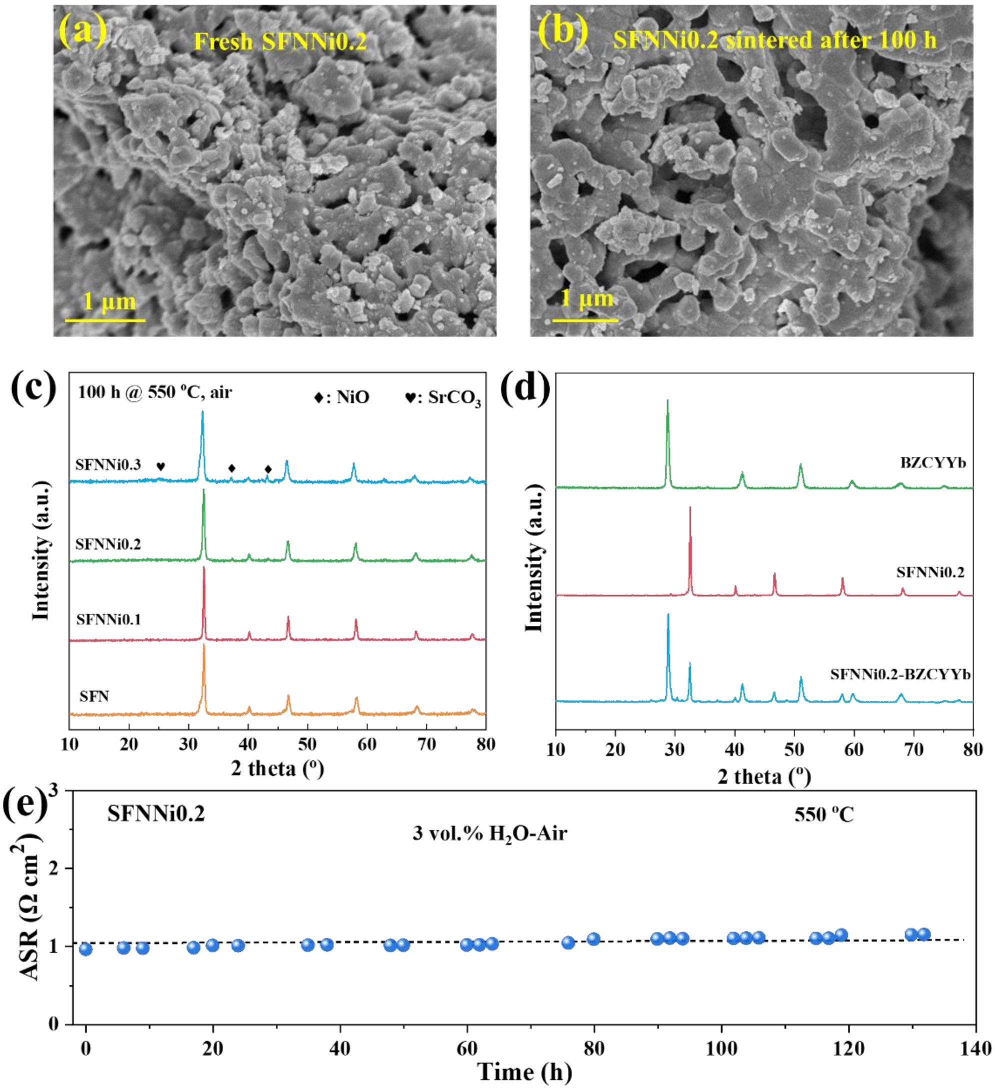

Figure 6. 8 Structural and performance stability of SFNNix samples. Microstructure of (a) fresh and (b) calcined SFNNi0.2 powder at 550 °C for 100 h in air. (c) XRD patterns of the powders after calcining in the air for 100 h. (d) Chemical compatibility of SFNNi0.2 and BZCYYb electrolyte powder. (e) Long-term polarization resistance evolution of the SFNNi0.2 electrode.

The phase stability of self-assembled materials prepared in one step is often a concern, as it is fundamental to the stability of electrode performance. During RePCC operation, air electrodes typically experience significant temperature variations and changes in the oxidative atmosphere, which can lead to phase transitions or segregation from the electrolyte, potentially causing cell failure. Therefore, it is necessary to study the stability of self-assembled materials. **Figures 6.8a-b** shows the microstructure of SFNNi0.2 before and after calcination for 100 hours. The morphology of the particulate SFNNi0.2 does not change significantly before and after calcination, and no significant agglomeration of the electrode particles is observed, indicating excellent sintering resistance of the self-assembled material. XRD is further used to investigate the phase composition of the four powder samples after calcination (**Figure 6.8c**). Except for the presence of $SrCO_3$ peaks near 25° in SFNNi0.3, the phase compositions of other three materials do not change significantly, indicating good phase stability of SFNNi0.2 electrode candidate.

Additionally, after thorough mixing and calcination of SFNNi0.2 and BZCYYb at 950 °C for 2 hours, only the characteristic diffraction peaks of BZCYYb and SFNNi0.2 are observed in the SFNNi0.2-BZCYYb composite material (**Figure 6.8d**), with no new phases forming, indicating good chemical compatibility between SFNNix powder and BZCYYb electrolyte. The evolution of polarization resistance of the SFNNi0.2 electrode is tested, as shown in **Figure 6.8e**. Over 132 hours of testing, the SFNNi0.2 electrode exhibits negligible degradation, demonstrating excellent stability.

Additionally, the thermal expansion curves of SFN and SFNNi0.2 samples are tested in an air atmosphere, as shown in **Figure 6.9**. In the temperature range of 30-1000 °C, the average linear TEC of the SFFNi0.2 sample is $18.1 \cdot 10^{-6}$ K^{-1}, which is significantly lower than the $24.2 \cdot 10^{-6}$ K^{-1} of the SFN sample. The lower TEC of SFNNi0.2 may be related to its multiphase structure. It is reported that strong chemical interactions between different phase structures in nanocomposite electrodes can effectively suppress chemical expansion during heating, thereby improving chemical compatibility with the electrolyte[80, 248].

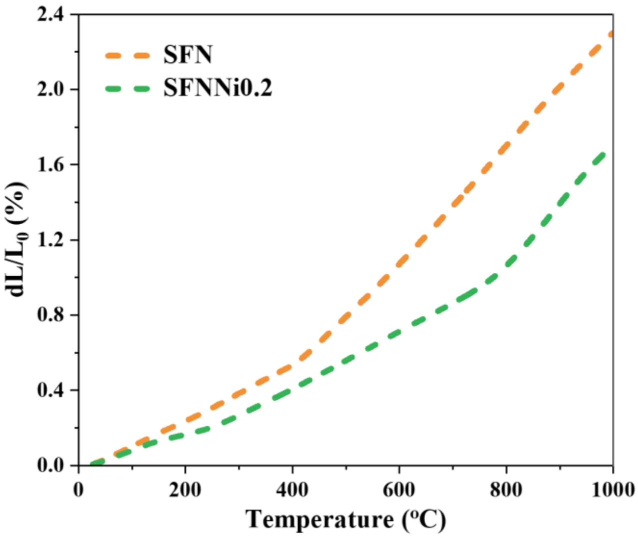

Figure 6. 9 Thermal expansion curves of SFN and SFNNi0.2 from room temperature to 1000 °C.

6.7 RePCC Testing

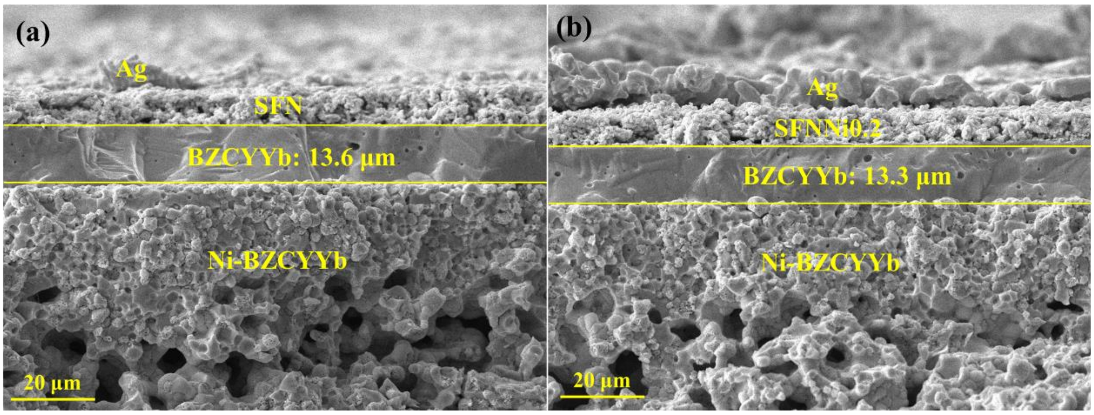

Figure 6. 10 Cross-sectional SEM images of SFNNix/BZCYYb/Ni-BZCYYb (x=0, 0.2) single cells after testing

RePCC performance testing is conducted on single cells configured as Ni-BZCYYb/BZCYYb/SFNNix. The cross-sectional morphology of the RePCC is examined after testing, as shown in **Figure 6.10**. The SFN and SFNNi0.2 air electrodes are closely bonded with the BZCYYb electrolyte. The two single cells have identical configurations except for the air electrode, with similar electrolyte thicknesses.

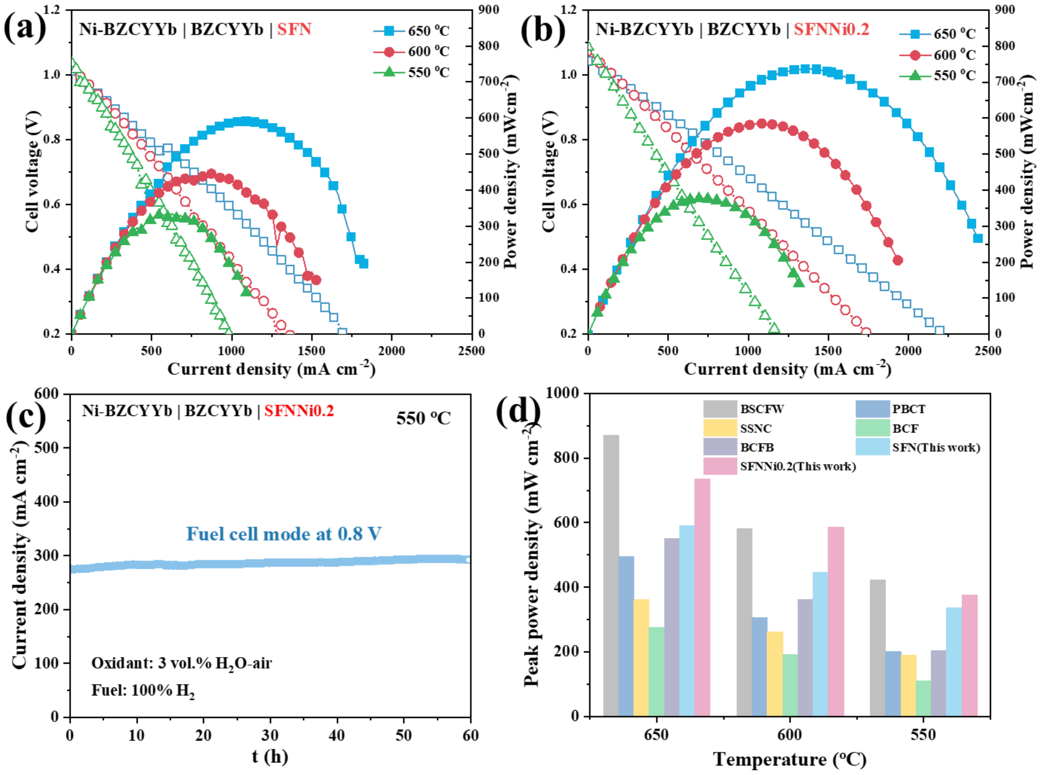

Figure 6. 11 Performance of single cells using SFNNix (x=0, 0.2) as the air electrode and BZCYYb as the electrolyte. I-V-p curves of the electrolysis cell with an SFN and b SFNNi0.2 as the air electrode. (c) Stability test of the fuel cell with SFNNi0.2 as the air electrode over 60 h. (d) Performance comparison of the SFNNi0.2-based single cell with reported cells.

The excellent electrochemical performance and durability of the SFNNi0.2 air electrode are further validated in the RePCC. **Figures 6.11a-b** show the I-V and I-P curves of the single cell with SFN and SFNNi0.2 as air electrodes, tested at temperatures ranging from 500 to 650 °C, with dry hydrogen supplied to the fuel electrode and 3 vol.% H2O-air to the air electrode. The maximum power densities of the single cell with the SFN air electrode at 650, 600, and 550 °C are 591, 446, and 335 mWcm^{-2}, respectively. In contrast, the single cell with the SFNNi0.2 air electrode in a nearly identical configuration achieves PPDs of 736, 586, and 377 mWcm^{-2}, representing increases of 25%, 31%, and 13%, respectively. The single cell with the SFNNi0.2 air electrode operates stably at an applied voltage of 0.8 V for 60 hours, maintaining consistent performance (**Figure 6.11c**). Compared to the performance of reported single cells under the same test conditions (**Figure 6.11d** and **Table 6.3**), the single cell with the SFNNi0.2 air electrode outperforms many Fe-based electrodes and is highly competitive with Co-based electrodes [227, 249].

Table 6. 3 The performance comparison of the SFNNi0.2-based PCFC with the reported single cells under the same operating conditions.

Air electrode	Electrolyte	PPD (mW cm^{-2})			Ref.
		650 °C	600 °C	550 °C	
BSCFW	BZCYYb (15 μm)	870	582	422	249
PBCT	BZCY (10 μm)	495	305	200	250
SSNC	BZCY (46 μm)	361	262	190	163
BCF	BZCY (25 μm)	276	192	111	164
BCYF	BZCYYb (16 μm)	829	656	487	227
BCFB	BZCY (25 μm)	551	362	203	165
SFN	BZCYYb (20 μm)	591	446	335	This work
SFNNi0.2	BZCYYb (20 μm)	736	586	377	This work

Note: BSCFW: $Ba_{0.5}Sr_{0.5}(Co_{0.7}Fe_{0.3})_{0.6875}W_{0.3125}O_{3-\delta}$; PBCT: $PrBaCo_{1.75}Ta_{0.25}O_{5+\delta}$; SSNC: $SrSc_{0.175}Nb_{0.025}Co_{0.8}O_{3-\delta}$; BCF: $BaCe_{0.5}Fe_{0.5}O_{3-\delta}$; BCYF: $BaCe_{0.16}Y_{0.04}Fe_{0.8}O_{3-\delta}$; BCFB: $BaCe_{0.5}Fe_{0.3}Bi_{0.2}O_{3-\delta}$.

In addition to fuel cell testing, the electrochemical performance and stability of RePCC using the SFNNi0.2 air electrode are evaluated in the electrolysis mode. The air electrode is supplied with humidified air containing 3 vol.% H_2O to perform the WOR. **Figures 6.12a-b** show the current-voltage curves from OCV to 1.6 V for cells using SFN and SFNNi0.2 as air electrodes, respectively. At 650 °C, the current density at 1.3 V for the SFN-based cell is 0.78 A cm^{-2}, while the current density for the SFNNi0.2-based cell reaches 0.92 A cm^{-2}. Additionally, electrolysis is sustained at a constant voltage of 1.3 V for nearly 140 hours, with a performance degradation rate of less than 1.5%, demonstrating the excellent long-term electrolysis stability of the cell with the SFNNi0.2 air electrode (**Figure 6.12c**).

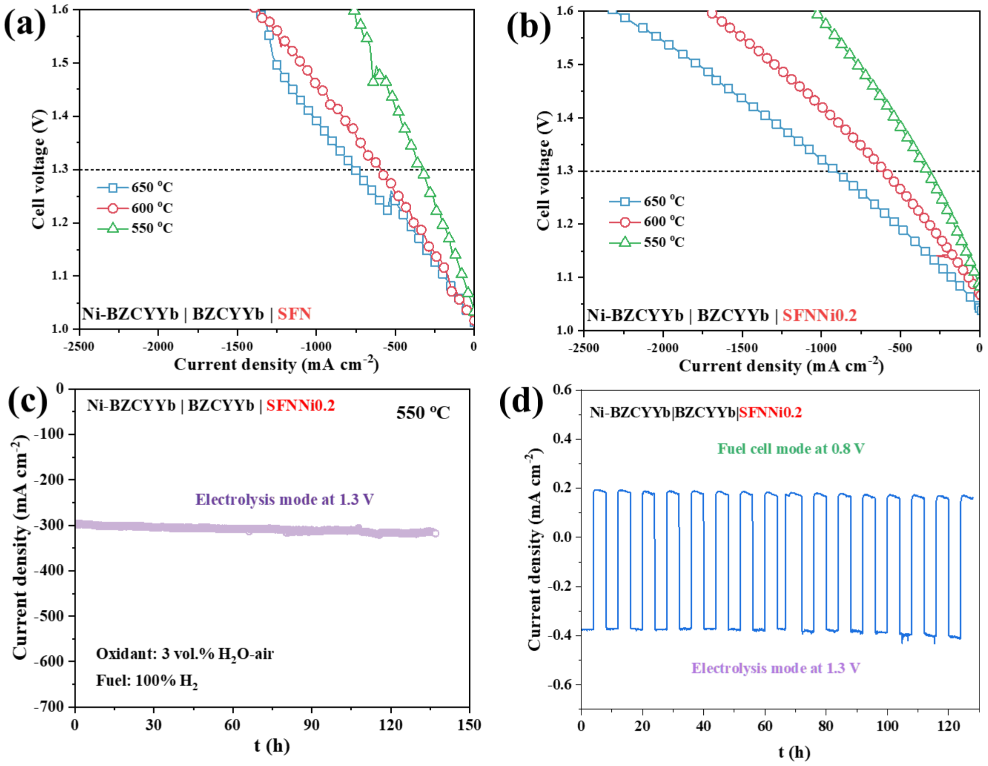

Figure 6. 12 The electrochemical performance and stability of the cells operated in electrolysis and reversible modes are evaluated. (a-b) Polarization curves with SFNNix (x=0, 0.2) as the air electrode. (c) Stability of the electrolysis cell with SFNNi0.2 as the air electrode over 137 hours. (d) The reversible stability test of the cell continuously operated in FC mode (under 0.8 V applied voltage) and EC mode (under 1.3 V applied voltage) for 128 h.

Furthermore, the cell is cycled between FC and EC modes for 128 hours, showing negligible performance degradation during the test (**Figure 6.12d**), confirming the superior reversible operability and durability of the single cell with the SFNNi0.2 air electrode.

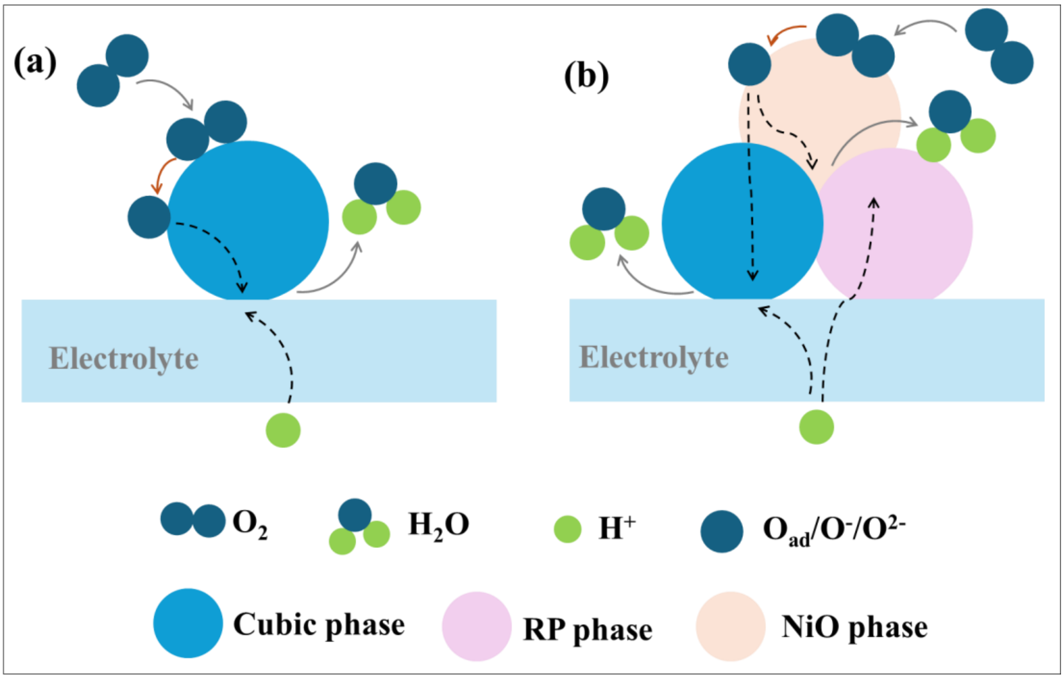

Figure 6. 13 Schematic diagram of the ORR reaction of self-assembled materials. (a) SFN air electrode. (b) Self-assembled SFNNix (x=0.1-0.3) air electrode.

Based on the above analysis, a schematic diagram illustrating the mechanism by which the self-assembled SFNNi0.2 material exhibits excellent performance as a RePCC air electrode is presented, as shown in **Figure 6.13**. For the sake of description, only the ORR process at the air electrode is depicted. When a single-phase SFN is used as the air electrode, the ORR activity is limited by the slow surface exchange and bulk proton transport properties of the electrode material (**Figure 6.13a**). In this case, the active sites for the electrode reaction are mainly located at the interface between the SFN electrode and the BZCYYb electrolyte. Conversely, when SFNNi0.2 is used as the air electrode, the introduction of NiO effectively enhances the surface exchange rate of the electrode, while the formation of the RP phase facilitates the creation of proton defects and bulk transport (**Figure 6.13b**). The close contact among the three phases significantly expands the active sites for the electrode reaction.

6.8 Conclusion

In this study, a series of SFNNix self-assembled materials is controllably synthesized. The incorporation of Ni introduces secondary phases, including C2/m monoclinic NiO and I4/mmm tetragonal RP phases. As the Ni doping level increases, the content of NiO and RP phases also increases. The close contact among the well-dispersed multiphases results in excellent sintering resistance and a low TEC. Electrochemical tests reveal that Ni doping significantly enhances the oxygen surface exchange and bulk diffusion rates, while the RP phase contributes to improved hydration performance and proton diffusion of the air electrode. The SFNNi0.2 electrode, with an optimal proportion of NiO and RP phases, exhibits the best performance. In RePCC applications, cells with SFNNi0.2 air electrodes demonstrate higher power densities and stable operation for 128 hours under RePCC conditions compared to cells with SFN electrodes. The superior performance of SFNNi0.2 is attributed to its balanced multiphase structure, enhanced surface exchange, and improved bulk diffusion properties. This study highlights the potential of the self-assembly method in the development of efficient and stable RePCC air electrode materials.

CHAPTER 7 Conclusions and Perspectives

7.1 Conclusions

This thesis examines the preparation and application of Fe-based RePCC air electrodes from the perspective of the material design. RePCC operates at intermediate temperatures rather than high temperatures, where its performance is frequently constrained by the air electrode. An ideal air electrode demonstrates excellent ORR/WOR electrochemical performance and durability. Careful design of air electrodes effectively addresses slow electrode reaction kinetics and enhances durability at intermediate temperatures. This study proposes three air electrode modification strategies through a comprehensive analysis of electrode reaction mechanisms and material design.

Firstly, a strategy involving high-valent Nb ion substitution achieves a balance between proton and oxygen properties in the material. By regulating the oxygen vacancy concentration and B-site metal-oxygen bond strength in the high-dimensional RP perovskite $Sr_3Fe_2O_{7-\delta}$ (SF), the balance mechanism between ORR/WOR and hydration in Nb-doped SF-based materials is elucidated. This coordination optimizes the proton- and oxygen-related properties of the material. A small amount of Nb doping ($Sr_3Fe_{1.9}Nb_{0.1}O_{7-\delta}$) reduces the surface hydration of SF without compromising oxygen vacancies, enhancing oxygen surface exchange and bulk transport. This results in synergistic improvements in ORR/WOR performance and durability, maintaining stable performance over 112 hours of RePCC testing.

Secondly, a simple A/B-site co-doping strategy for designing and developing RP-layered oxide-based perovskite air electrodes further enhances the stability of SF-based materials. By introducing Sr defects and Nb doping simultaneously, $Sr_{2.8}Fe_{1.8}Nb_{0.2}O_{7-\delta}$ (D2-SFN) is synthesized. Physical-chemical characterization and theoretical calculations demonstrate that Nb doping stabilizes the crystal structure and suppresses excessive formation of $Sr_3Fe_2(OH)_{12}$, thereby ensuring the stability of the main phase structure. Simultaneously, the introduction of Sr defects increases the oxygen vacancy concentration, improving oxygen transport properties. The results show that D2-SFN achieves a peak power density of 596 mW cm^{-2} in fuel cell mode at 650 °C, a current density of -1.19 A cm^{-2} at 1.3 V in electrolysis mode, and stable performance over 160 hours and 20 fuel cell-electrolysis cycles.

Finally, a strategy to control the phase composition of self-assembled materials leverages the self-segregation of RP and NiO phases within a stable cubic parent material. This approach capitalizes on the hydration and proton transport properties of the RP phase while preserving the stability of the parent phase. The multiphase synergistic approach enhances electrode activity and stability. Self-assembled air electrodes with closely matched multiphase structures exhibit significantly reduced thermal expansion coefficients and improved anti-sintering properties. By adjusting the Ni doping level, the phase proportions are optimized to improve electrochemical performance. The optimized SFNNi0.2 air electrode-based RePCC achieves a maximum power density of 736 mW cm^{-2} at 650 °C and operates stably for 128 hours in both fuel cell and electrolysis cell modes.

7.2 Perspectives

This thesis conducts a comprehensive study on the development of RePCC air electrodes from the perspective of material design, achieving improvements in both the electrochemical activity and stability of RePCCs. However, challenges remain between current research and the practical application of RePCCs. Future research directions in this field are suggested as follows:

Firstly, the durability of SF-based RP perovskite materials for air electrodes requires further improvement. Current studies reveal that the stability of SF-based RP materials remains insufficient for air electrode applications, particularly as existing tests often show significant phase transformations within a few hundred hours. In contrast, practical applications of RePCCs demand stability over tens of thousands of hours. Moreover, secondary phases of RP perovskites formed in humid atmospheres negatively impact their electrochemical performance. Strategies to stabilize the phase composition and enhance the electrochemical properties of SF-based RP materials need further development to promote their practical applications.

Secondly, the proton conduction mechanism and experimental characterization techniques for RP perovskite materials require further investigation and development. Limited research currently addresses the proton conduction mechanism of RP perovskites, with most studies approximating the mechanism observed in cubic perovskites. This approach is also adopted in this study. However, crystal structure significantly influences ion transport mechanisms, necessitating more theoretical studies on proton conduction in RP perovskites. Additionally, in most existing studies on RePCC air electrodes, the characterization of proton defects and conduction is primarily achieved by assessing hydration performance. While simple, this method lacks precision. Direct measurement of proton conductivity remains challenging because it is substantially lower than O^{2-} conductivity. Since proton conductivity is a critical property for RePCC air electrode materials, developing advanced experimental techniques for proton-related property characterization is essential for designing triple-conducting (H^+-O^{2-}-e^-) air electrode materials.

Finally, while multiphase self-assembled materials exhibit synergistic performance enhancement in air electrodes, further optimization of air electrode structure and phase distribution is necessary. This study finds that the distribution of NiO at the three-phase boundary affects proton transport across the membrane, a factor overlooked in previous studies using NiO-modified air electrodes. By precisely controlling the distribution of each phase, closer interphase synergistic effects can be achieved, further improving air electrode performance. Combining self-assembly strategies with more advanced electrode preparation techniques, or adopting state-of-the-art powder preparation methods, offers promising opportunities to optimize the structural configuration of multiphase electrodes and achieve further performance enhancements.

REFERENCES

1. Mogensen, M. B., Materials for reversible solid oxide cells. *Current Opinion in Electrochemistry* **2020,** *21*, 265-273.
2. Wang, Y.; Song, Y.; Liu, J.; Yang, K.; Lin, X.; Yang, Z.; Ciucci, F., Functionalized metal-supported reversible protonic ceramic cells with exceptional performance and durability. *Advanced Energy and Sustainability Research* **2022,** *3* (2), 2100171.
3. Hauch, A.; Küngas, R.; Blennow, P.; Hansen, A. B.; Hansen, J. B.; Mathiesen, B. V.; Mogensen, M. B., Recent advances in solid oxide cell technology for electrolysis. *Science* **2020,** *370* (6513), eaba6118.
4. Mogensen, M. B.; Chen, M.; Frandsen, H. L.; Graves, C.; Hansen, J. B.; Hansen, K. V.; Hauch, A.; Jacobsen, T.; Jensen, S. H.; Skafte, T. L.; Sun, X., Reversible solid-oxide cells for clean and sustainable energy. *Clean Energy* **2019,** *3* (3), 175-201.
5. Duan, C.; Kee, R.; Zhu, H.; Sullivan, N.; Zhu, L.; Bian, L.; Jennings, D.; O'Hayre, R., Highly efficient reversible protonic ceramic electrochemical cells for power generation and fuel production. *Nature Energy* **2019,** *4* (3), 230-240.
6. Wachsman, E. D.; Lee, K. T., Lowering the temperature of solid oxide fuel cells. *Science* **2011,** *334* (6058), 935-939.
7. Zhou, C.; Liu, D.; Fei, M.; Wang, X.; Ran, R.; Xu, M.; Wang, W.; Zhou, W.; O'Hayre, R.; Shao, Z., Cathode water management towards improved performance of protonic ceramic fuel cells. *Journal of Power Sources* **2023,** *556*, 232403.
8. Kim, J.; Sengodan, S.; Kim, S.; Kwon, O.; Bu, Y.; Kim, G., Proton conducting oxides: A review of materials and applications for renewable energy conversion and storage. *Renewable and Sustainable Energy Reviews* **2019,** *109*, 606-618.
9. Song, Y.; Liu, J.; Wang, Y.; Guan, D.; Seong, A.; Liang, M.; Robson, M. J.; Xiong, X.; Zhang, Z.; Kim, G.; Shao, Z.; Ciucci, F., Nanocomposites: A new opportunity for developing highly active and durable bifunctional air electrodes for reversible protonic ceramic cells. *Advanced Energy Materials* **2021,** *11* (36), 2101899.
10. Wang, N.; Tang, C.; Du, L.; Zhu, R.; Xing, L.; Song, Z.; Yuan, B.; Zhao, L.; Aoki, Y.; Ye, S., Advanced cathode materials for protonic ceramic fuel cells: Recent progress and future perspectives. *Advanced Energy Materials* **2022,** *12* (34), 2201882.
11. Lankauf, K.; Mroziński, A.; Błaszczak, P.; Gόrnicka, K.; Ignaczak, J.; Łapiński, M.; Karczewski, J.; Cempura, G.; Jasiński, P.; Molin, S., The effect of Fe on chemical stability and oxygen evolution performance of high surface area SrTix-1FexO3-δ mixed ionic-electronic conductors in alkaline media. *International Journal of Hydrogen Energy* **2021,** *46* (56), 28575-28590.

12. Zhu, Y.; Lin, Q.; Hu, Z.; Chen, Y.; Yin, Y.; Tahini, H. A.; Lin, H.-J.; Chen, C.-T.; Zhang, X.; Shao, Z.; Wang, H., Self-Assembled Ruddlesden–Popper/Perovskite Hybrid with Lattice-Oxygen Activation as a Superior Oxygen Evolution Electrocatalyst. *Small* **2020,** *16* (20), 2001204.
13. Wang, Z.; Yang, W.; Shafi, S. P.; Bi, L.; Wang, Z.; Peng, R.; Xia, C.; Liu, W.; Lu, Y., A high performance cathode for proton conducting solid oxide fuel cells. *Journal of Materials Chemistry A* **2015,** *3* (16), 8405-8412.
14. Matvejeff, M.; Lehtimäki, M.; Hirasa, A.; Huang, Y. H.; Yamauchi, H.; Karppinen, M., New Water-Containing Phase Derived from the Sr3Fe2O7-δ Phase of the Ruddlesden−Popper Structure. *Chemistry of Materials* **2005,** *17* (10), 2775-2779.
15. Wang, Y.; Ling, Y.; Wang, B.; Zhai, G.; Yang, G.; Shao, Z.; Xiao, R.; Li, T., A review of progress in proton ceramic electrochemical cells: material and structural design, coupled with value-added chemical production. *Energy & Environmental Science* **2023,** *16* (12), 5721-5770.
16. Kasyanova, A. V.; Zvonareva, I. A.; Tarasova, N. A.; Bi, L.; Medvedev, D. A.; Shao, Z., Electrolyte materials for protonic ceramic electrochemical cells: Main limitations and potential solutions. *Materials Reports: Energy* **2022,** *2* (4), 100158.
17. Zhou, X.-D., Kill two problems with one dual-ion cell. *Joule* **2019,** *3* (11), 2595-2597.
18. Yang, L.; Wang, S.; Blinn, K.; Liu, M.; Liu, Z.; Cheng, Z.; Liu, M., Enhanced Sulfur and Coking Tolerance of a Mixed Ion Conductor for SOFCs: BaZr0.1Ce0.7Y0.2–xYbxO3–δ. *Science* **2009,** *326* (5949), 126-129.
19. Choi, M.; Paik, J.; Kim, D.; Woo, D.; Lee, J.; Kim, S. J.; Lee, J.; Lee, W., Exceptionally high performance of protonic ceramic fuel cells with stoichiometric electrolytes. *Energy & Environmental Science* **2021,** *14* (12), 6476-6483.
20. Bae, K.; Kim, D. H.; Choi, H. J.; Son, J.-W.; Shim, J. H., High-performance protonic ceramic fuel cells with 1 µm thick $Y{:}Ba(Ce, Zr)O_3$ electrolytes. *Advanced Energy Materials* **2018,** *8* (25), 1801315.
21. Kreuer, K.-D., Proton conductivity: Materials and applications. *Chemistry of Materials* **1996,** *8* (3), 610-641.
22. Sun, C.; Hui, R.; Roller, J., Cathode materials for solid oxide fuel cells: a review. *Journal of Solid State Electrochemistry* **2010,** *14* (7), 1125-1144.
23. Bai, H.; Chu, J.; Chen, T.; Leng, Z.; Zhang, B.; Zhang, Y.; Zhou, Q.; Zhou, J.; Wang, S., PrBa0.5Sr0.5Co1.5Fe0.5O5+δ as air electrode for proton-conducting solid oxide cells. *Journal of Power Sources* **2023,** *574*, 233162.
24. Liang, M.; Song, Y.; Liu, D.; Xu, L.; Xu, M.; Yang, G.; Wang, W.; Zhou, W.; Ran, R.; Shao, Z., Magnesium tuned triple conductivity and bifunctionality of $BaCo_{0.4}Fe_{0.4}Zr_{0.1}Y_{0.1}O_{3-\delta}$ perovskite towards reversible protonic ceramic electrochemical cells. *Applied Catalysis B: Environmental* **2022,** *318*, 121868.
25. Stangl, A.; Riaz, A.; Rapenne, L.; Caicedo, J. M.; de Dios Sirvent, J.; Baiutti, F.; Jiménez, C.; Tarancón, A.; Mermoux, M.; Burriel, M., Tailored nano-columnar La2NiO4 cathodes for improved electrode performance. *Journal of Materials Chemistry A* **2022,** *10* (5), 2528-2540.

26. Ghani Harzand, A.; Golmohammad, M.; Zargar, S. A.; Khachatourian, A. M.; Nemati, A., Study of structural, electrical, and electrochemical properties of Sr3-xPrxFe1.8Co0.2O7-δ cathode for IT-SOFCs. *Solid State Ionics* **2024,** *404*, 116421.
27. He, F.; Wu, T.; Peng, R.; Xia, C., Cathode reaction models and performance analysis of $Sm_{0.5}Sr_{0.5}CoO_{3-\delta}$–$BaCe_{0.8}Sm_{0.2}O_{3-\delta}$ composite cathode for solid oxide fuel cells with proton conducting electrolyte. *Journal of Power Sources* **2009,** *194* (1), 263-268.
28. Cao, J.; Ji, Y.; Shao, Z., Perovskites for protonic ceramic fuel cells: A review. *Energy & Environmental Science* **2022,** *15* (6), 2200-2232.
29. Agmon, N., The Grotthuss mechanism. *Chemical Physics Letters* **1995,** *244* (5), 456-462.
30. Fabbri, E.; Oh, T.-k.; Licoccia, S.; Traversa, E.; Wachsman, E. D., Mixed Protonic/Electronic Conductor Cathodes for Intermediate Temperature SOFCs Based on Proton Conducting Electrolytes. *Journal of the Electrochemical Society* **2009,** *156* (1), B38.
31. Atkinson, A.; Barnett, S.; Gorte, R. J.; Irvine, J. T. S.; McEvoy, A. J.; Mogensen, M.; Singhal, S. C.; Vohs, J., Advanced anodes for high-temperature fuel cells. *Nature Materials* **2004,** *3* (1), 17-27.
32. Gross, M. D.; Vohs, J. M.; Gorte, R. J., Recent progress in SOFC anodes for direct utilization of hydrocarbons. *Journal of Materials Chemistry* **2007,** *17* (30), 3071-3077.
33. Richter, J.; Holtappels, P.; Graule, T.; Nakamura, T.; Gauckler, L. J., Materials design for perovskite SOFC cathodes. *Monatshefte für Chemie - Chemical Monthly* **2009,** *140* (9), 985-999.
34. Jorgensen, J. D.; Dabrowski, B.; Pei, S.; Richards, D. R.; Hinks, D. G., Structure of the interstitial oxygen defect in ${\mathrm{La}}_{2}$${\mathrm{NiO}}_{4+\mathrm{\ensuremath{\delta}}}$. *Physical Review B* **1989,** *40* (4), 2187-2199.
35. Skinner, S. J., Characterisation of La2NiO4+δ using in-situ high temperature neutron powder diffraction. *Solid State Sciences* **2003,** *5* (3), 419-426.
36. Cook, R. L.; Sammells, A. F., On the systematic selection of perovskite solid electrolytes for intermediate temperature fuel cells. *Solid State Ionics* **1991,** *45* (3), 311-321.
37. Merkle, R.; Poetzsch, D.; Maier, J., Oxygen reduction reaction at cathodes on proton conducting oxide electrolytes: Contribution from three phase boundary compared to bulk path. *ECS Transactions* **2015,** *66* (2), 95.
38. Merkle, R.; Hoedl, M. F.; Raimondi, G.; Zohourian, R.; Maier, J., Oxides with mixed protonic and electronic conductivity. *Annual Review of Materials Research* **2021,** *51* (Volume 51, 2021), 461-493.
39. Ren, R.; Wang, Z.; Meng, X.; Wang, X.; Xu, C.; Qiao, J.; Sun, W.; Sun, K., Tailoring the oxygen vacancy to achieve fast intrinsic proton transport in a perovskite cathode for protonic ceramic fuel cells. *ACS Applied Energy Materials* **2020,** *3* (5), 4914-4922.

40. Zohourian, R.; Merkle, R.; Maier, J., Proton uptake into the protonic cathode material BaCo0.4Fe0.4Zr0.2O3-δ and comparison to protonic electrolyte materials. *Solid State Ionics* **2017,** *299*, 64-69.
41. Papac, M.; Stevanović, V.; Zakutayev, A.; O'Hayre, R., Triple ionic–electronic conducting oxides for next-generation electrochemical devices. *Nature Materials* **2021,** *20* (3), 301-313.
42. Wei, Z.; Li, Z.; Wang, Z.; Zhao, Y.; Wang, J.; Chai, J., A free-cobalt barium ferrite cathode with improved resistance against CO_2 and water vapor for protonic ceramic fuel cells. *International Journal of Hydrogen Energy* **2022,** *47* (27), 13490-13501.
43. Yang, J.; Polfus, J. M.; Li, Z.; Tuller, H. L.; Yildiz, B., Role of adsorbate coverage on the oxygen dissociation rate on Sr-doped $LaMnO_3$ surfaces in the presence of H_2O and CO_2. *Chemistry of Materials* **2020,** *32* (13), 5483-5492.
44. Huang, Y. L.; Pellegrinelli, C.; Wachsman, E. D., Fundamental impact of humidity on SOFC cathode ORR. *Journal of the Electrochemical Society* **2016,** *163* (3), F171.
45. Kilner, J. A.; Burriel, M., Materials for intermediate-temperature solid-oxide fuel cells. *Annual Review of Materials Research* **2014,** *44* (Volume 44, 2014), 365-393.
46. Mather, G. C.; Muñoz-Gil, D.; Zamudio-García, J.; Porras-Vázquez, J. M.; Marrero-López, D.; Pérez-Coll, D. Perspectives on Cathodes for Protonic Ceramic Fuel Cells *Applied Sciences* [Online], 2021.
47. Zhang, Q.; Ding, J.; He, M., First principles study on structural, lattice dynamical and thermal properties of $BaCeO_3$. *Journal of Physics and Chemistry of Solids* **2017,** *108*, 76-81.
48. Zhu, K.; Liu, H.; Li, X.; Li, Q.; Wang, J.; Zhu, X.; Yang, W., Oxygen evolution reaction over Fe site of BaZrxFe1-xO3-δ perovskite oxides. *Electrochimica Acta* **2017,** *241*, 433-439.
49. Jing, J.; Pang, J.; Chen, L.; Zhang, H.; Lei, Z.; Yang, Z., Structure, synthesis, properties and solid oxide electrolysis cells application of $Ba(Ce, Zr)O_3$ based proton conducting materials. *Chemical Engineering Journal* **2022,** *429*, 132314.
50. Kim, J.; Sengodan, S.; Kwon, G.; Ding, D.; Shin, J.; Liu, M.; Kim, G., Triple-conducting layered perovskites as cathode materials for proton-conducting solid oxide fuel cells. *ChemSusChem* **2014,** *7* (10), 2811-2815.
51. Kim, J.-H.; Manthiram, A., Layered $LnBaCo_2O_{5+\delta}$ perovskite cathodes for solid oxide fuel cells: an overview and perspective. *Journal of Materials Chemistry A* **2015,** *3* (48), 24195-24210.
52. Streule, S.; Podlesnyak, A.; Sheptyakov, D.; Pomjakushina, E.; Stingaciu, M.; Conder, K.; Medarde, M.; Patrakeev, M. V.; Leonidov, I. A.; Kozhevnikov, V. L.; Mesot, J., High-temperature order-disorder transition and polaronic conductivity in $PrBaCo_2O_{5.48}$. *Physical Review B* **2006,** *73* (9), 094203.
53. Tarancón, A.; Marrero-López, D.; Peña-Martínez, J.; Ruiz-Morales, J. C.; Núñez, P., Effect of phase transition on high-temperature electrical properties of GdBaCo2O5+x layered perovskite. *Solid State Ionics* **2008,** *179* (17), 611-618.

54. Chen, Y.-C.; Yashima, M.; Peña-Martínez, J.; Kilner, J. A., Experimental Visualization of the Diffusional Pathway of Oxide Ions in a Layered Perovskite-type Cobaltite PrBaCo2O5+δ. *Chemistry of Materials* **2013,** *25* (13), 2638-2641.
55. Bernuy-Lopez, C.; Rioja-Monllor, L.; Nakamura, T.; Ricote, S.; O'Hayre, R.; Amezawa, K.; Einarsrud, M.-A.; Grande, T., Effect of cation ordering on the performance and chemical stability of layered double perovskite cathodes. *Materials* **2018,** *11* (2), 196.
56. Lei, L.; Tao, Z.; Wang, X.; Lemmon, J. P.; Chen, F., Intermediate-temperature solid oxide electrolysis cells with thin proton-conducting electrolyte and a robust air electrode. *Journal of Materials Chemistry A* **2017,** *5* (44), 22945-22951.
57. Seong, A.; Kim, J.; Kim, J.; Kim, S.; Sengodan, S.; Shin, J.; Kim, G., Influence of cathode porosity on high performance protonic ceramic fuel cells with $PrBa_{0.5}Sr_{0.5}Co_{1.5}Fe_{0.5}O_{5-\delta}$ cathode. *Journal of the Electrochemical Society* **2018,** *165* (13), F1098-F1102.
58. Choi, S.; Kucharczyk, C. J.; Liang, Y.; Zhang, X.; Takeuchi, I.; Ji, H.-I.; Haile, S. M., Exceptional power density and stability at intermediate temperatures in protonic ceramic fuel cells. *Nature Energy* **2018,** *3* (3), 202-210.
59. Xu, X.; Pan, Y.; Zhong, Y.; Ran, R.; Shao, Z., Ruddlesden–Popper perovskites in electrocatalysis. *Materials Horizons* **2020,** *7* (10), 2519-2565.
60. Ganguly, P.; Rao, C. N. R., Crystal chemistry and magnetic properties of layered metal oxides possessing the K2NiF4 or related structures. *Journal of Solid State Chemistry* **1984,** *53* (2), 193-216.
61. Tong, X.; Zhou, F.; Yang, S.; Zhong, S.; Wei, M.; Liu, Y., Performance and stability of Ruddlesden-Popper $La_2NiO_{4+\delta}$ oxygen electrodes under solid oxide electrolysis cell operation conditions. *Ceramics International* **2017,** *43* (14), 10927-10933.
62. Amow, G.; Skinner, S. J., Recent developments in Ruddlesden–Popper nickelate systems for solid oxide fuel cell cathodes. *Journal of Solid State Electrochemistry* **2006,** *10* (8), 538-546.
63. Miao, L.; Hou, J.; Gong, Z.; Jin, Z.; Liu, W., A high-performance cobalt-free Ruddlesden-Popper phase cathode $La_{1.2}Sr_{0.8}Ni_{0.6}Fe_{0.4}O_{4+\delta}$ for low temperature proton-conducting solid oxide fuel cells. *International Journal of Hydrogen Energy* **2019,** *44* (14), 7531-7537.
64. Song, J.; Ning, D.; Boukamp, B.; Bassat, J.-M.; Bouwmeester, H. J. M., Structure, electrical conductivity and oxygen transport properties of Ruddlesden–Popper phases $Ln_{n+1}Ni_nO_{3n+1}$ (Ln = La, Pr and Nd; n = 1, 2 and 3). *Journal of Materials Chemistry A* **2020,** *8* (42), 22206-22221.
65. Tarancón, A.; Burriel, M.; Santiso, J.; Skinner, S. J.; Kilner, J. A., Advances in layered oxide cathodes for intermediate temperature solid oxide fuel cells. *Journal of Materials Chemistry* **2010,** *20* (19), 3799-3813.
66. Mather, G. C.; Muñoz-Gil, D.; Zamudio-García, J.; Porras-Vázquez, J. M.; Marrero-López, D.; Pérez-Coll, D., Perspectives on cathodes for protonic ceramic fuel cells. *Applied Sciences* **2021,** *11* (12), 5363.

67. Mukundan, R.; Davies, P. K.; Worrell, W. L., Electrochemical characterization of mixed conducting $Ba(Ce_{1-(x+y)}Pr_yGd_x)O_{3-x/2}$ cathodes. *MRS Proceedings* **1996,** *453*, 573.
68. Wu, Y.; Li, K.; Yang, Y.; Song, W.; Ma, Z.; Chen, H.; Ou, X.; Zhao, L.; Khan, M.; Ling, Y., Investigation of Fe-substituted in $BaZr_{0.8}Y_{0.2}O_{3-\delta}$ proton conducting oxides as cathode materials for protonic ceramics fuel cells. *Journal of Alloys and Compounds* **2020,** *814*, 152220.
69. Wang, N.; Hinokuma, S.; Ina, T.; Toriumi, H.; Katayama, M.; Inada, Y.; Zhu, C.; Habazaki, H.; Aoki, Y., Incorporation of bulk proton carriers in cubic perovskite manganite driven by interplays of oxygen and manganese redox. *Chemistry of Materials* **2019,** *31* (20), 8383-8393.
70. Meng, X.; Yang, N.; Song, J.; Tan, X.; Ma, Z.-F.; Li, K., Synthesis and characterization of terbium doped barium cerates as a proton conducting SOFC electrolyte. *International Journal of Hydrogen Energy* **2011,** *36* (20), 13067-13072.
71. Oda, H.; Okuyama, Y.; Sakai, T.; Matsumoto, H., Preparation of nano-structured $La_{0.6}Sr_{0.4}Co_{0.2}Fe_{0.8}O_{3-\delta}$ cathode for protonic ceramic fuel cell by bead-milling method. *Materials Transactions* **2014,** *55* (4), 722-727.
72. Robinson, S.; Manerbino, A.; Grover Coors, W.; Sullivan, N. P., Fabrication and performance of tubular, electrode-supported $BaCe_{0.2}Zr_{0.7}Y_{0.1}O_{3-\delta}$ fuel cells. *Fuel Cells* **2013,** *13* (4), 584-591.
73. Wang, B.; Bi, L.; Zhao, X. S., Liquid-phase synthesis of $SrCo_{0.9}Nb_{0.1}O_{3-\delta}$ cathode material for proton-conducting solid oxide fuel cells. *Ceramics International* **2018,** *44* (5), 5139-5144.
74. Shao, Z.; Haile, S. M., A high-performance cathode for the next generation of solid-oxide fuel cells. *Nature* **2004,** *431* (7005), 170-3.
75. Yang, L.; Zuo, C.; Wang, S.; Cheng, Z.; Liu, M., A novel composite cathode for low-temperature SOFCs based on oxide proton conductors. *Advanced Materials* **2008,** *20* (17), 3280-3283.
76. Yang, L.; Liu, Z.; Wang, S.; Choi, Y.; Zuo, C.; Liu, M., A mixed proton, oxygen ion, and electron conducting cathode for SOFCs based on oxide proton conductors. *Journal of Power Sources* **2010,** *195* (2), 471-474.
77. Choi, J.; Kim, B.; Song, S.-H.; Park, J.-S., A composite cathode with undoped $LaFeO_3$ for protonic ceramic fuel cells. *International Journal of Hydrogen Energy* **2016,** *41* (22), 9619-9626.
78. Dailly, J.; Taillades, G.; Ancelin, M.; Pers, P.; Marrony, M., High performing $BaCe_{0.8}Zr_{0.1}Y_{0.1}O_{3-\delta}$-$Sm_{0.5}Sr_{0.5}CoO_{3-\delta}$ based protonic ceramic fuel cell. *Journal of Power Sources* **2017,** *361*, 221-226.
79. Duan Chuancheng , J. T., 1* Meng Shang,1 Stefan Nikodemski,1 Michael Sanders,1 Sandrine Ricote,1 Ali Almansoori,2 Ryan O'Hayre, Readily processed protonic ceramic fuel cells with high performance at low temperatures. *Science* **2015**.

80. Song, Y.; Chen, Y.; Wang, W.; Zhou, C.; Zhong, Y.; Yang, G.; Zhou, W.; Liu, M.; Shao, Z., Self-assembled triple-conducting nanocomposite as a superior protonic ceramic fuel cell cathode. *Joule* **2019,** *3* (11), 2842-2853.
81. Choi, S.; Yoo, S.; Kim, J.; Park, S.; Jun, A.; Sengodan, S.; Kim, J.; Shin, J.; Jeong, H. Y.; Choi, Y.; Kim, G.; Liu, M., Highly efficient and robust cathode materials for low-temperature solid oxide fuel cells: PrBa0.5Sr0.5Co2−xFexO5+ δ . *Scientific Reports* **2013,** *3* (1), 2426.
82. Duan, C.; Kee, R. J.; Zhu, H.; Karakaya, C.; Chen, Y.; Ricote, S.; Jarry, A.; Crumlin, E. J.; Hook, D.; Braun, R.; Sullivan, N. P.; O'Hayre, R., Highly durable, coking and sulfur tolerant, fuel-flexible protonic ceramic fuel cells. *Nature* **2018,** *557* (7704), 217-222.
83. Zhang, K.; Sunarso, J.; Shao, Z.; Zhou, W.; Sun, C.; Wang, S.; Liu, S., Research progress and materials selection guidelines on mixed conducting perovskite-type ceramic membranes for oxygen production. *RSC Advances* **2011,** *1* (9), 1661-1676.
84. Tejuca, L. G.; Fierro, J. L. G.; Tascón, J. M. D., Structure and reactivity of perovskite-type oxides. 1989; pp 237-328.
85. Inoue, I. H., Electrostatic carrier doping to perovskite transition-metal oxides. *Semiconductor Science and Technology* **2005,** *20* (4), S112.
86. Hwang, J.; Rao, R. R.; Giordano, L.; Katayama, Y.; Yu, Y.; Shao-Horn, Y., Perovskites in catalysis and electrocatalysis. *Science* **2017,** *358* (6364), 751-756.
87. Smith, D. W., An acidity scale for binary oxides. *Journal of Chemical Education* **1987,** *64* (6), 480-481.
88. Yang, Y.; Shi, N.; Xie, Y.; Li, X.; Hu, X.; Zhu, K.; Huan, D.; Peng, R.; Xia, C.; Lu, Y., K doping as a rational method to enhance the sluggish air-electrode reaction kinetics for proton-conducting solid oxide cells. *Electrochimica Acta* **2021,** *389*, 138453.
89. Chen, X.; Yu, N.; Bello, I. T.; Guan, D.; Li, Z.; Liu, T.; Liu, T.; Shao, Z.; Ni, M., Facile anion engineering: A pathway to realizing enhanced triple conductivity in oxygen electrodes for reversible protonic ceramic electrochemical cells. *Energy Storage Materials* **2023,** *63*, 103056.
90. Chen, X.; Yu, N.; Song, Y.; Liu, T.; Xu, H.; Guan, D.; Li, Z.; Huang, W.-H.; Shao, Z.; Ciucci, F.; Ni, M., Synergistic bulk and surface engineering for expeditious and durable reversible protonic ceramic electrochemical cells air electrode. *Advanced Materials* **2024,** *n/a* (n/a), 2403998.
91. Xu, S.; Qiu, H.; Jiang, S.; Jiang, J.; Wang, W.; Xu, X.; Kong, W.; Chivurugwi, T. D.; Proskurin, A.; Chen, D.; Su, C., New strategy for boosting cathodic performance of low temperature solid oxide fuel cells via chlorine doping. *Nano Research* **2024,** *17* (9), 8086-8094.
92. Zohourian, R.; Merkle, R.; Raimondi, G.; Maier, J., Mixed-conducting perovskites as cathode materials for protonic ceramic fuel cells: understanding the trends in proton uptake. *Advanced Functional Materials* **2018,** *28* (35), 1801241.
93. Tang, W.; Ding, H.; Bian, W.; Wu, W.; Li, W.; Liu, X.; Gomez, J. Y.; Regalado Vera, C. Y.; Zhou, M.; Ding, D., Understanding of A-site deficiency in layered

perovskites: promotion of dual reaction kinetics for water oxidation and oxygen reduction in protonic ceramic electrochemical cells. *Journal of Materials Chemistry A* **2020,** *8* (29), 14600-14608.

94. Zhang, Q.; Qiu, H.; Jiang, S.; Liu, Y.; Xu, J.; Wang, W.; Chen, D.; Su, C., Enhanced ORR Activity of A-Site-Deficient SrCo0.8Nb0.1Ti0.1O3−δ as a Bifunctional Air Electrode for Low-Temperature Solid Oxide Fuel Cells. *Energy & Fuels* **2023,** *37* (9), 6740-6748.
95. Shi, K.; Yin, Y.; Tang, Z.; Yu, S.; Zhang, Q., Ba-deficiency in BaCoO3 cathode allows high performance for proton-conducting solid oxide fuel cells. *Ceramics International* **2022,** *48* (9), 13024-13031.
96. Waller, D.; Lane, J. A.; Kilner, J. A.; Steele, B. C. H., The effect of thermal treatment on the resistance of LSCF electrodes on gadolinia doped ceria electrolytes. *Solid State Ionics* **1996,** *86-88*, 767-772.
97. Xu, X.; Pan, Y.; Zhong, Y.; Shi, C.; Guan, D.; Ge, L.; Hu, Z.; Chin, Y.-Y.; Lin, H.-J.; Chen, C.-T.; Wang, H.; Jiang, S. P.; Shao, Z., New Undisputed Evidence and Strategy for Enhanced Lattice-Oxygen Participation of Perovskite Electrocatalyst through Cation Deficiency Manipulation. *Advanced Science* **2022,** *9* (14), 2200530.
98. Neagu, D.; Tsekouras, G.; Miller, D. N.; Ménard, H.; Irvine, J. T. S., In situ growth of nanoparticles through control of non-stoichiometry. *Nature Chemistry* **2013,** *5* (11), 916-923.
99. Li, P.; Dong, R.; Wang, Y.; Yan, F.; Wang, L.; Li, M.; Fu, D., Improving the performance of Pr0.4Sr0.6Co0.2Fe0.7Nb0.1O3-δ-based single-component fuel cell and reversible single-component cells by manufacturing A-site deficiency. *Renewable Energy* **2021,** *177*, 387-396.
100. He, F.; Liang, M.; Wang, W.; Ran, R.; Yang, G.; Zhou, W.; Shao, Z., High-Performance Proton-Conducting Fuel Cell with B-Site-Deficient Perovskites for All Cell Components. *Energy & Fuels* **2020,** *34* (9), 11464-11471.
101. Kuai, X.; Yang, G.; Chen, Y.; Sun, H.; Dai, J.; Song, Y.; Ran, R.; Wang, W.; Zhou, W.; Shao, Z., Boosting the activity of $BaCo_{0.4}Fe_{0.4}Zr_{0.1}Y_{0.1}O_{3-\delta}$ perovskite for oxygen reduction reactions at low-to-intermediate temperatures through tuning B-site cation deficiency. *Advanced Energy Materials* **2019,** *9* (38), 1902384.
102. Su, C.; Wang, W.; Shao, Z., Cation-Deficient Perovskites for Clean Energy Conversion. *Accounts of Materials Research* **2021,** *2* (7), 477-488.
103. Konysheva, E. Y.; Xu, X.; Irvine, J. T. S., On the Existence of A-Site Deficiency in Perovskites and Its Relation to the Electrochemical Performance. *Advanced Materials* **2012,** *24* (4), 528-532.
104. Cantor, B.; Chang, I. T. H.; Knight, P.; Vincent, A. J. B., Microstructural development in equiatomic multicomponent alloys. *Materials Science and Engineering: A* **2004,** *375-377*, 213-218.
105. Yeh, J. W.; Chen, S. K.; Lin, S. J.; Gan, J. Y.; Chin, T. S.; Shun, T. T.; Tsau, C. H.; Chang, S. Y., Nanostructured High-Entropy Alloys with Multiple Principal

Elements: Novel Alloy Design Concepts and Outcomes. *Advanced Engineering Materials* **2004,** *6* (5), 299-303.

106. Xiang, H.; Xing, Y.; Dai, F.-z.; Wang, H.; Su, L.; Miao, L.; Zhang, G.; Wang, Y.; Qi, X.; Yao, L.; Wang, H.; Zhao, B.; Li, J.; Zhou, Y., High-entropy ceramics: Present status, challenges, and a look forward. *Journal of Advanced Ceramics* **2021,** *10* (3), 385-441.
107. Wang, Y.; Liu, J.; Song, Y.; Yu, J.; Tian, Y.; Robson, M. J.; Wang, J.; Zhang, Z.; Lin, X.; Zhou, G.; Wang, Z.; Shen, L.; Zhao, H.; Grasso, S.; Ciucci, F., High-Entropy Perovskites for Energy Conversion and Storage: Design, Synthesis, and Potential Applications. *Small Methods* **2023,** *7* (4), 2201138.
108. Yang, C.; Li, J.; Hu, S.; Pu, J.; Chi, B., Novel high-entropy BaCo0.2Zn0.2Ga0.2Zr0.2Y0.2O3-δ cathode for proton ceramic fuel cells. *Ceramics International* **2023,** *49* (23, Part A), 38331-38338.
109. Li, H.; Lai, J.; Li, Z.; Wang, L., Multi-Sites Electrocatalysis in High-Entropy Alloys. *Advanced Functional Materials* **2021,** *31* (47), 2106715.
110. Hao, J.; Zhuang, Z.; Cao, K.; Gao, G.; Wang, C.; Lai, F.; Lu, S.; Ma, P.; Dong, W.; Liu, T.; Du, M.; Zhu, H., Unraveling the electronegativity-dominated intermediate adsorption on high-entropy alloy electrocatalysts. *Nature Communications* **2022,** *13* (1), 2662.
111. Wang, Z.; Hao, Z.; Shi, F.; Zhu, K.; Zhu, X.; Yang, W., Boosting the oxygen evolution reaction through migrating active sites from the bulk to surface of perovskite oxides. *Journal of Energy Chemistry* **2022,** *69*, 434-441.
112. Wang, X.; Li, X.; Chu, X.; Cao, R.; Qian, J.; Cong, Y.; Huang, K.; Wang, J.; Redshaw, C.; Sarangi, R.; Li, G.; Feng, S., Manipulating Surface Termination of Perovskite Manganate for Oxygen Activation. *Advanced Functional Materials* **2021,** *31* (14), 2006439.
113. Zhuang, Z.; Li, Y.; Yu, R.; Xia, L.; Yang, J.; Lang, Z.; Zhu, J.; Huang, J.; Wang, J.; Wang, Y.; Fan, L.; Wu, J.; Zhao, Y.; Wang, D.; Li, Y., Reversely trapping atoms from a perovskite surface for high-performance and durable fuel cell cathodes. *Nature Catalysis* **2022,** *5* (4), 300-310.
114. Plonczak, P.; Gazda, M.; Kusz, B.; Jasinski, P., Fabrication of solid oxide fuel cell supported on specially performed ferrite-based perovskite cathode. *Journal of Power Sources* **2008,** *181* (1), 1-7.
115. Gómez, S. Y.; Hotza, D., Current developments in reversible solid oxide fuel cells. *Renewable and Sustainable Energy Reviews* **2016,** *61*, 155-174.
116. Vergunst, T.; Kapteijn, F.; Moulijn, J. A., Monolithic catalysts — non-uniform active phase distribution by impregnation. *Applied Catalysis A: General* **2001,** *213* (2), 179-187.
117. Jiang, Z.; Xia, C.; Chen, F., Nano-structured composite cathodes for intermediate-temperature solid oxide fuel cells via an infiltration/impregnation technique. *Electrochimica Acta* **2010,** *55* (11), 3595-3605.
118. Jiang, S. P., Nanoscale and nano-structured electrodes of solid oxide fuel cells by infiltration: Advances and challenges. *International Journal of Hydrogen Energy* **2012,** *37* (1), 449-470.

119. Kim, J. H.; Yoo, S.; Murphy, R.; Chen, Y.; Ding, Y.; Pei, K.; Zhao, B.; Kim, G.; Choi, Y.; Liu, M., Promotion of oxygen reduction reaction on a double perovskite electrode by a water-induced surface modification. *Energy & Environmental Science* **2021,** *14* (3), 1506-1516.
120. Zhou, Y.; Liu, E.; Chen, Y.; Liu, Y.; Zhang, L.; Zhang, W.; Luo, Z.; Kane, N.; Zhao, B.; Soule, L.; Niu, Y.; Ding, Y.; Ding, H.; Ding, D.; Liu, M., An active and robust air electrode for reversible protonic ceramic electrochemical cells. *ACS Energy Letters* **2021,** *6* (4), 1511-1520.
121. Gao, Y.; Zhang, M.; Fu, M.; Hu, W.; Tong, H.; Tao, Z., A comprehensive review of recent progresses in cathode materials for Proton-conducting SOFCs. *Energy Reviews* **2023,** *2* (3), 100038.
122. Ai, N.; Chen, K., A La0. 8Sr0. 2MnO3/La0. 6Sr0. 4Co0. 2Fe0. 8O3− δ core–shell structured cathode by a rapid sintering process for solid oxide fuel cells. *International Journal Of Hydrogen Energy* **2017,** *42* (10), 7246-7251.
123. Duan, C.; Huang, J.; Sullivan, N.; O'Hayre, R., Proton-conducting oxides for energy conversion and storage. *Applied Physics Reviews* **2020,** *7* (1), 011314.
124. Chiara, A.; Giannici, F.; Pipitone, C.; Longo, A.; Aliotta, C.; Gambino, M.; Martorana, A., Solid–Solid Interfaces in Protonic Ceramic Devices: A Critical Review. *Acs Applied Materials & Interfaces* **2020,** *12* (50), 55537-55553.
125. Bu, Y.; Joo, S.; Zhang, Y.; Wang, Y.; Meng, D.; Ge, X.; Kim, G., A highly efficient composite cathode for proton-conducting solid oxide fuel cells. *Journal of Power Sources* **2020,** *451*, 227812.
126. Kim, J. H.; Jang, K.; Lim, D.-K.; Ahn, S.; Oh, D.; Kim, H.; Seo, J.; Choi, P.-P.; Jung, W., Self-assembled nano-composite perovskites as highly efficient and robust hybrid cathodes for solid oxide fuel cells. *Journal of Materials Chemistry A* **2022,** *10* (5), 2496-2508.
127. Lee, S.; Park, S.; Wee, S.; Baek, H. w.; Shin, D., One-dimensional structured $La_{0.6}Sr_{0.4}Co_{0.2}Fe_{0.8}O_{3-\delta}$ - $BaCe_{0.5}Zr_{0.35}Y_{0.15}O_{3-\delta}$ composite cathode for protonic ceramic fuel cells. *Solid State Ionics* **2018,** *320*, 347-352.
128. Lee, S.; Park, S.; Wee, S.; Baek, H. w.; Shin, D., One-dimensional structured La0.6Sr0.4Co0.2Fe0.8O3−δ - BaCe0.5Zr0.35Y0.15O3−δ composite cathode for protonic ceramic fuel cells. *Solid State Ionics* **2018,** *320*, 347-352.
129. Bae, K.; Jang, D. Y.; Choi, H. J.; Kim, D.; Hong, J.; Kim, B.-K.; Lee, J.-H.; Son, J.-W.; Shim, J. H., Demonstrating the potential of yttrium-doped barium zirconate electrolyte for high-performance fuel cells. *Nature Communications* **2017,** *8* (1), 14553.
130. Park, J. S.; Choi, H. J.; Han, G. D.; Koo, J.; Kang, E. H.; Kim, D. H.; Bae, K.; Shim, J. H., High–performance protonic ceramic fuel cells with a PrBa0.5Sr0.5Co1.5Fe0.5O5+δ cathode with palladium–rich interface coating. *Journal of Power Sources* **2021,** *482*, 229043.
131. Shim, J. H.; Kang, S.; Cha, S.-W.; Lee, W.; Kim, Y. B.; Park, J. S.; Gür, T. M.; Prinz, F. B.; Chao, C.-C.; An, J., Atomic layer deposition of thin-film ceramic

electrolytes for high-performance fuel cells. *Journal of Materials Chemistry A* **2013,** *1* (41), 12695-12705.

132. Park, H. S.; Jeong, H. J.; Kim, K.-h.; Chang, W.; Kim, Y. S.; Choi, Y. S.; Shim, J. H., High-performance proton ceramic fuel cells using a perovskite oxide cathode surface decorated with CoOx nanoparticles. *Applied Surface Science* **2023,** *612*, 155812.
133. Li, Y.; Gerdes, K.; Liu, X., Oxygen transport kinetics in infiltrated SOFCs cathode by electrical conductivity relaxation technique. *Journal of the Electrochemical Society* **2013,** *160* (6), F554-F559.
134. Ouyang, J.; Li, C.-H.; Hu, S.-H., Chemical bulk diffusion coefficient of $Sm_{0.5}Sr_{0.5}CoO_{3-\delta}$ cathode for solid oxide fuel cells. *Journal of Power Sources* **2013,** *240*, 168-177.
135. Ciucci, F., Electrical conductivity relaxation measurements: Statistical investigations using sensitivity analysis, optimal experimental design and ECRTOOLS. *Solid State Ionics* **2013,** *239*, 28-40.
136. Kresse, G.; Furthmüller, J., Efficiency of ab-initio total energy calculations for metals and semiconductors using a plane-wave basis set. *Computational materials science* **1996,** *6* (1), 15-50.
137. Kresse, G.; Furthmüller, J., Efficient iterative schemes for ab initio total-energy calculations using a plane-wave basis set. *Physical Review B* **1996,** *54* (16), 11169-11186.
138. Perdew, J. P.; Burke, K.; Ernzerhof, M., Generalized gradient approximation made simple. *Physical Review Letters* **1996,** *77* (18), 3865-3868.
139. Suntivich, J.; Gasteiger, H. A.; Yabuuchi, N.; Nakanishi, H.; Goodenough, J. B.; Shao-Horn, Y., Design principles for oxygen-reduction activity on perovskite oxide catalysts for fuel cells and metal-air batteries. *Nature Chemistry* **2011,** *3* (7), 546-550.
140. Yao, P.; Zhang, J.; Qiu, Q.; Li, G.; Zhao, Y.; Yu, F.; Li, Y., Design of a perovskite oxide cathode for a protonic ceramic fuel cell. *Ceramics International* **2024,** *50* (1, Part B), 2373-2382.
141. Viswanathan, V.; Hansen, H. A.; Rossmeisl, J.; Norskov, J. K., Unifying the 2e(-) and 4e(-) Reduction of Oxygen on Metal Surfaces. *J Phys Chem Lett* **2012,** *3* (20), 2948-51.
142. Bajdich, M.; García-Mota, M.; Vojvodic, A.; Nørskov, J. K.; Bell, A. T., Theoretical investigation of the activity of cobalt oxides for the electrochemical oxidation of water. *Journal of the American Chemical Society* **2013,** *135* (36), 13521-13530.
143. Chen, C.; Ciucci, F., Designing Fe-based oxygen catalysts by density functional theory calculations. *Chemistry of Materials* **2016,** *28* (19), 7058-7065.
144. Wang, Z.; Wang, Y.; Wang, J.; Song, Y.; Robson, M. J.; Seong, A.; Yang, M.; Zhang, Z.; Belotti, A.; Liu, J.; Kim, G.; Lim, J.; Shao, Z.; Ciucci, F., Rational design of perovskite ferrites as high-performance proton-conducting fuel cell cathodes. *Nature Catalysis* **2022,** *5* (9), 777-787.

145. Malerød-Fjeld, H.; Clark, D.; Yuste-Tirados, I.; Zanón, R.; Catalán-Martinez, D.; Beeaff, D.; Morejudo, S. H.; Vestre, P. K.; Norby, T.; Haugsrud, R.; Serra, J. M.; Kjølseth, C., Thermo-electrochemical production of compressed hydrogen from methane with near-zero energy loss. *Nature Energy* **2017,** *2* (12), 923-931.
146. Chen, Y.; Qian, B.; Yang, G.; Chen, D.; Shao, Z., Insight into an unusual lanthanum effect on the oxygen reduction reaction activity of Ruddlesden-Popper-type cation-nonstoichiometric $La_{2-x}NiO_{4+\delta}$ (x = 0–0.1) oxides. *Journal of Materials Chemistry A* **2015,** *3* (12), 6501-6508.
147. Batocchi, P.; Mauvy, F.; Fourcade, S.; Parco, M., Electrical and electrochemical properties of architectured electrodes based on perovskite and A_2MO_4-type oxides for protonic ceramic fuel cell. *Electrochimica Acta* **2014,** *145*, 1-10.
148. Liu, Z.; Xie, H.; Zhang, Y.; Li, J.; You, J.; Yang, H.; Zhu, H.; Ni, M.; Shao, Z.; Chen, B., Towards high performance durable ceramic fuel cells using a triple conducting perovskite cathode. *Applied Catalysis B: Environment and Energy* **2024,** *346*, 123678.
149. Wang, X.; Li, W.; Zhou, C.; Xu, M.; Hu, Z.; Pao, C.-W.; Zhou, W.; Shao, Z., Enhanced proton conduction with low oxygen vacancy concentration and favorable hydration for protonic ceramic fuel cells cathode. *ACS Applied Materials & Interfaces* **2023,** *15* (1), 1339-1347.
150. Xiao, Y.; Bao, D.; Wang, Z.; Wang, Y.; He, T., Tailoring $Ba_{0.5}Sr_{0.5}FeO_{3-\delta}$ cobalt-free perovskites with zinc as triple-conducting cathodes for protonic ceramic fuel cells. *International Journal of Hydrogen Energy* **2024,** *57*, 880-888.
151. Wang, X.; Ma, Z.; Zhang, T.; Kang, J.; Ou, X.; Feng, P.; Wang, S.; Zhou, F.; Ling, Y., Charge-transfer modeling and polarization DRT analysis of proton ceramics fuel cells based on mixed conductive electrolyte with the modified anode-electrolyte interface. *ACS Applied Materials and Interfaces* **2018,** *10* (41), 35047-35059.
152. Wan, T. H.; Saccoccio, M.; Chen, C.; Ciucci, F., Influence of the discretization methods on the distribution of relaxation times deconvolution: Implementing radial basis functions with DRTtools. *Electrochimica Acta* **2015,** *184*, 483-499.
153. Dailly, J.; Fourcade, S.; Largeteau, A.; Mauvy, F.; Grenier, J. C.; Marrony, M., Perovskite and A_2MO_4-type oxides as new cathode materials for protonic solid oxide fuel cells. *Electrochimica Acta* **2010,** *55* (20), 5847-5853.
154. Yahia, H. B.; Mauvy, F.; Grenier, J. C., $Ca_{3-x}La_xCo_4O_{9+\delta}$ (x=0, 0.3): New cobaltite materials as cathodes for proton conducting solid oxide fuel cell. *Journal of Solid State Chemistry* **2010,** *183* (3), 527-531.
155. Fabbri, E.; Licoccia, S.; Traversa, E.; Wachsman, E. D., Composite cathodes for proton conducting electrolytes. *Fuel Cells* **2009,** *9* (2), 128-138.
156. Vert, V. B.; Solís, C.; Serra, J. M., Electrochemical properties of PSFC–BCYb composites as cathodes for proton conducting solid oxide fuel cells. *Fuel Cells* **2011,** *11* (1), 81-90.
157. Grimaud, A.; Mauvy, F.; Bassat, J. M.; Fourcade, S.; Rocheron, L.; Marrony, M.; Grenier, J. C., Hydration properties and rate determining steps of the oxygen

reduction reaction of perovskite-related oxides as H^+-SOFC cathodes. *Journal of the Electrochemical Society* **2012,** *159* (6), B683.

158. Shang, M.; Tong, J.; O'Hayre, R., A promising cathode for intermediate temperature protonic ceramic fuel cells: $BaCo_{0.4}Fe_{0.4}Zr_{0.2}O_{3-\delta}$. *RSC Advances* **2013,** *3* (36), 15769-15775.
159. Zhang, C.; Zhao, H., A novel cobalt-free cathode material for proton-conducting solid oxide fuel cells. *Journal of Materials Chemistry* **2012,** *22* (35), 18387-18394.
160. Samat, A. A.; Jais, A. A.; Somalu, M. R.; Osman, N.; Muchtar, A.; Lim, K. L., Electrical and electrochemical characteristics of $La_{0.6}Sr_{0.4}CoO_{3-\delta}$ cathode materials synthesized by a modified citrate-EDTA sol-gel method assisted with activated carbon for proton-conducting solid oxide fuel cell application. *Journal of Sol-Gel Science and Technology* **2018,** *86* (3), 617-630.
161. Duan, C.; Tong, J.; Shang, M.; Nikodemski, S.; Sanders, M.; Ricote, S.; Almansoori, A.; O'Hayre, R., Readily processed protonic ceramic fuel cells with high performance at low temperatures. *Science* **2015,** *349* (6254), 1321-1326.
162. Wei, Z.; Wang, J.; Yu, X.; Li, Z.; Zhao, Y.; Chai, J., Study on Ce and Y co-doped $BaFeO_{3-\delta}$ cubic perovskite as free-cobalt cathode for proton-conducting solid oxide fuel cells. *International Journal of Hydrogen Energy* **2021,** *46* (46), 23868-23878.
163. Zhu, A.; Zhang, G.; Wan, T.; Shi, T.; Wang, H.; Wu, M.; Wang, C.; Huang, S.; Guo, Y.; Yu, H.; Shao, Z., Evaluation of $SrSc_{0.175}Nb_{0.025}Co_{0.8}O_{3-\delta}$ perovskite as a cathode for proton-conducting solid oxide fuel cells: The possibility of in situ creating protonic conductivity and electrochemical performance. *Electrochimica Acta* **2018,** *259*, 559-565.
164. Tao, Z.; Bi, L.; Zhu, Z.; Liu, W., Novel cobalt-free cathode materials $BaCe_xFe_{1-x}O_{3-\delta}$ for proton-conducting solid oxide fuel cells. *Journal of Power Sources* **2009,** *194* (2), 801-804.
165. Shan, D.; Gong, Z.; Wu, Y.; Miao, L.; Dong, K.; Liu, W., A novel $BaCe_{0.5}Fe_{0.3}Bi_{0.2}O_{3-\delta}$ perovskite-type cathode for proton-conducting solid oxide fuel cells. *Ceramics International* **2017,** *43* (4), 3660-3663.
166. Zhang, L.; Yang, S.; Zhang, S.; Yang, Y., Cerium and gadolinium co-doped perovskite oxide for a protonic ceramic fuel cell cathode. *International Journal of Hydrogen Energy* **2019,** *44* (51), 27921-27929.
167. Huan, D.; Shi, N.; Zhang, L.; Tan, W.; Xie, Y.; Wang, W.; Xia, C.; Peng, R.; Lu, Y., New, efficient, and reliable air electrode material for proton-conducting reversible solid oxide cells. *ACS Applied Materials & Interfaces* **2018,** *10* (2), 1761-1770.
168. Moreno Botello, Z. L.; Montenegro, A.; Grimaldos Osorio, N.; Huvé, M.; Pirovano, C.; Småbråten, D. R.; Selbach, S. M.; Caneiro, A.; Roussel, P.; Gauthier, G. H., Pure and Zr-doped $YMnO_{3+\delta}$ as a YSZ-compatible SOFC cathode: A combined computational and experimental approach. *Journal of Materials Chemistry A* **2019,** *7* (31), 18589-18602.

169. Xu, J.; Cai, H.; Hao, G.; Zhang, L.; Song, Z.; Long, W.; Zhang, L.; Wang, L., Characterization of high–valence Mo–doped $PrBaCo_2O_{5+\delta}$ cathodes for IT-SOFCs. *Journal of Alloys and Compounds* **2020,** *842*, 155600.
170. Lu, C.; Ren, R.; Zhu, Z.; Pan, G.; Wang, G.; Xu, C.; Qiao, J.; Sun, W.; Huang, Q.; Liang, H.; Wang, Z.; Sun, K., $BaCo_{0.4}Fe_{0.4}Nb_{0.1}Sc_{0.1}O_{3-\delta}$ perovskite oxide with super hydration capacity for a high-activity proton ceramic electrolytic cell oxygen electrode. *Chemical Engineering Journal* **2023,** *472*, 144878.
171. Wang, J.; Saccoccio, M.; Chen, D.; Gao, Y.; Chen, C.; Ciucci, F., The effect of A-site and B-site substitution on $BaFeO_{3-\delta}$: An investigation as a cathode material for intermediate-temperature solid oxide fuel cells. *Journal of Power Sources* **2015,** *297*, 511-518.
172. Dong, F.; Chen, Y.; Ran, R.; Chen, D.; Tadé, M. O.; Liu, S.; Shao, Z., $BaNb_{0.05}Fe_{0.95}O_{3-\delta}$ as a new oxygen reduction electrocatalyst for intermediate temperature solid oxide fuel cells. *Journal of Materials Chemistry A* **2013,** *1* (34), 9781-9791.
173. Ren, R.; Wang, Z.; Xu, C.; Sun, W.; Qiao, J.; Rooney, D. W.; Sun, K., Tuning the defects of the triple conducting oxide $BaCo_{0.4}Fe_{0.4}Zr_{0.1}Y_{0.1}O_{3-\delta}$ perovskite toward enhanced cathode activity of protonic ceramic fuel cells. *Journal of Materials Chemistry A* **2019,** *7* (31), 18365-18372.
174. Li, Y.; Tian, Y.; Li, J.; Pu, J.; Chi, B., Sr-free orthorhombic perovskite $Pr_{0.8}Ca_{0.2}Fe_{0.8}Co_{0.2}O_{3-\delta}$ as a high-performance air electrode for reversible solid oxide cell. *Journal of Power Sources* **2022,** *528*, 231202.
175. Liang, M.; Zhu, Y.; Song, Y.; Guan, D.; Luo, Z.; Yang, G.; Jiang, S. P.; Zhou, W.; Ran, R.; Shao, Z., A new durable surface nanoparticles-modified perovskite cathode for protonic ceramic fuel cells from selective cation exsolution under oxidizing atmosphere. *Advanced Materials* **2022,** *34* (10), 2106379.
176. Lee, K.-C.; Choi, M.-B.; Lim, D.-K.; Singh, B.; Song, S.-J., Effect of humidification on the performance of intermediate-temperature proton conducting ceramic fuel cells with ceramic composite cathodes. *Journal of Power Sources* **2013,** *232*, 224-233.
177. Hagiwara, A.; Hobara, N.; Takizawa, K.; Sato, K.; Abe, H.; Naito, M., Preparation and evaluation of mechanochemically fabricated LSM/ScSZ composite materials for SOFC cathodes. *Solid State Ionics* **2006,** *177* (33), 2967-2977.
178. Huan, D.; Zhang, L.; Zhu, K.; Li, X.; Shi, N.; Yang, Y.; Xia, C.; Xie, Y.; Peng, R., Oxygen vacancy-engineered cobalt-free Ruddlesden-Popper cathode with excellent CO_2 tolerance for solid oxide fuel cells. *Journal of Power Sources* **2021,** *497*, 229872.
179. Jiang, S.; Sunarso, J.; Zhou, W.; Shen, J.; Ran, R.; Shao, Z., Cobalt-free $SrNb_xFe_{1-x}O_{3-\delta}$ (x = 0.05, 0.1 and 0.2) perovskite cathodes for intermediate temperature solid oxide fuel cells. *Journal of Power Sources* **2015,** *298*, 209-216.
180. Idisi, D. O.; Meyer, E. L.; Benecha, E. M., The role of iron oxide on the electronic and electrical properties of nitrogenated reduced graphene oxide: Experimental and density functional theory approach. *Journal of Materials Science: Materials in Electronics* **2024,** *35* (2), 192.

181. Pham, T. T.; Pham, T. N.; Chihaia, V.; Vu, Q. A.; Trinh, T. T.; Pham, T. T.; Van Thang, L.; Son, D. N., How do the doping concentrations of N and B in graphene modify the water adsorption? *RSC Advances* **2021,** *11* (32), 19560-19568.
182. Zhang, H.; Gao, Y.; Xu, H.; Guan, D.; Hu, Z.; Jing, C.; Sha, Y.; Gu, Y.; Huang, Y.-C.; Chang, Y.-C.; Pao, C.-W.; Xu, X.; Lee, J.-F.; Chin, Y.-Y.; Lin, H.-J.; Chen, C.-T.; Chen, Y.; Guo, Y.; Ni, M.; Zhou, W.; Shao, Z., Combined corner-sharing and edge-sharing networks in hybrid nanocomposite with unusual lattice-oxygen activation for efficient water oxidation. *Advanced Functional Materials* **2022,** *32* (45), 2207618.
183. Fujimori, A.; Bocquet, A. E.; Saitoh, T.; Mizokawa, T., Electronic structure of 3d transition metal compounds: Systematic chemical trends and multiplet effects. *Journal of Electron Spectroscopy and related Phenomena* **1993,** *62* (1), 141-152.
184. Zhou, X.; Hou, N.; Gan, T.; Fan, L.; Zhang, Y.; Li, J.; Gao, G.; Zhao, Y.; Li, Y., Enhanced oxygen reduction reaction activity of $BaCe_{0.2}Fe_{0.8}O_{3-\delta}$ cathode for proton-conducting solid oxide fuel cells via Pr-doping. *Journal of Power Sources* **2021,** *495*, 229776.
185. Xia, W.; Li, Q.; Sun, L.; Huo, L.; Zhao, H., Enhanced electrochemical performance and CO_2 tolerance of $Ba_{0.95}La_{0.05}Fe_{0.85}Cu_{0.15}O_{3-\delta}$ as Fe-based cathode electrocatalyst for solid oxide fuel cells. *Journal of the European Ceramic Society* **2020,** *40* (5), 1967-1974.
186. Xu, X.; Wang, H.; Fronzi, M.; Wang, X.; Bi, L.; Traversa, E., Tailoring cations in a perovskite cathode for proton-conducting solid oxide fuel cells with high performance. *Journal of Materials Chemistry A* **2019,** *7* (36), 20624-20632.
187. Millican, S. L.; Deml, A. M.; Papac, M.; Zakutayev, A.; O'Hayre, R.; Holder, A. M.; Musgrave, C. B.; Stevanović, V., Predicting oxygen off-stoichiometry and hydrogen incorporation in complex perovskite oxides. *Chemistry of Materials* **2022,** *34* (2), 510-518.
188. Li, H.; Li, J.; Wang, X.; Xie, C.; Wang, Y.; Ding, X., Electrochemical performance and enhancement of hydration kinetics on $BaCo_{0.7}Fe_{0.2}Zr_{0.1}O_{3-\delta}$ cathode for protonic ceramic fuel cells. *ACS Applied Energy Materials* **2023,** *6* (17), 8966-8975.
189. Zhang, W.; Muroyama, H.; Mikami, Y.; Liu, Q.; Liu, X.; Matsui, T.; Eguchi, K., Effectively enhanced oxygen reduction activity and stability of triple-conducting composite cathodes by strongly interacting interfaces for protonic ceramic fuel cells. *Chemical Engineering Journal* **2023,** *461*, 142056.
190. Lee, Y.-L.; Kleis, J.; Rossmeisl, J.; Morgan, D., Ab initio energetics of $LaBO_3$ (001) (B=Mn, Fe, Co, and Ni) for solid oxide fuel cell cathodes. *Physical Review B* **2009,** *80* (22), 224101.
191. Huan, D.; Zhang, L.; Li, X.; Xie, Y.; Shi, N.; Xue, S.; Xia, C.; Peng, R.; Lu, Y., A durable ruddlesden-popper cathode for protonic ceramic fuel cells. *ChemSusChem* **2020,** *13* (18), 4994-5003.
192. Wang, J.; Lam, K. Y.; Saccoccio, M.; Gao, Y.; Chen, D.; Ciucci, F., Ca and In co-doped $BaFeO_{3-\delta}$ as a cobalt-free cathode material for intermediate-temperature solid oxide fuel cells. *Journal of Power Sources* **2016,** *324*, 224-232.

193. Wang, S.; Zan, J.; Qiu, W.; Zheng, D.; Li, F.; Chen, W.; Pei, Q.; Jiang, L., Evaluation of perovskite oxides $LnBaCo_2O_{5+\delta}$ (Ln = La, Pr, Nd and Sm) as cathode materials for IT-SOFC. *Journal of Electroanalytical Chemistry* **2021,** *886*, 115144.
194. Kim, J.; Jun, A.; Shin, J.; Kim, G., Effect of Fe doping on layered $GdBa_{0.5}Sr_{0.5}Co_2O_{5+\delta}$ perovskite cathodes for intermediate temperature solid oxide fuel cells. *Journal of the American Ceramic Society* **2014,** *97* (2), 651-656.
195. Gou, M.; Ren, R.; Sun, W.; Xu, C.; Meng, X.; Wang, Z.; Qiao, J.; Sun, K., Nb-doped $Sr_2Fe_{1.5}Mo_{0.5}O_{6-\delta}$ electrode with enhanced stability and electrochemical performance for symmetrical solid oxide fuel cells. *Ceramics International* **2019,** *45* (12), 15696-15704.
196. Yun, S.; Yu, J.; Lee, W.; Lee, H.; Yoon, W.-S., Achieving structural stability and enhanced electrochemical performance through Nb-doping into Li- and Mn-rich layered cathode for lithium-ion batteries. *Materials Horizons* **2023,** *10* (3), 829-841.
197. Hou, Y.; Wang, L.; Bian, L.; Zhang, Q.; Chen, L.; Chou, K.-c., Effect of high-valence elements doping at B site of $La_{0.5}Sr_{0.5}FeO_{3-\delta}$. *Ceramics International* **2022,** *48* (3), 4223-4229.
198. Bello, I. T.; Zhai, S.; He, Q.; Cheng, C.; Dai, Y.; Chen, B.; Zhang, Y.; Ni, M., Materials development and prospective for protonic ceramic fuel cells. *International Journal of Energy Research* **2022,** *46* (3), 2212-2240.
199. Hoedl, M. F.; Gryaznov, D.; Merkle, R.; Kotomin, E. A.; Maier, J., Interdependence of oxygenation and hydration in mixed-conducting $(Ba, Sr)FeO_{3-\delta}$ perovskites studied by density functional theory. *Journal of Physical Chemistry C* **2020,** *124* (22), 11780-11789.
200. Merkle, R.; Hoedl, M. F.; Raimondi, G.; Zohourian, R.; Maier, J., Oxides with mixed protonic and electronic conductivity. *Annual Review of Materials Research* **2021,** *51* (1), 461-493.
201. Matvejeff, M.; Lehtimäki, M.; Hirasa, A.; Huang, Y. H.; Yamauchi, H.; Karppinen, M., New water-containing phase derived from the $Sr_3Fe_2O_{7-\delta}$ phase of the Ruddlesden-Popper structure. *Chemistry of Materials* **2005,** *17* (10), 2775-2779.
202. Zakharchuk, K. V.; Yaremchenko, A. A.; Fagg, D. P., Electrical properties and thermal expansion of strontium aluminates. *Journal of Alloys and Compounds* **2014,** *613*, 232-237.
203. Slater, P. R.; Greaves, C., The ionic conductivity of proton containing garnets and their decomposition products. *Solid State Ionics* **1992,** *53-56*, 989-992.
204. Zhang, Y.; Chen, B.; Guan, D.; Xu, M.; Ran, R.; Ni, M.; Zhou, W.; O'Hayre, R.; Shao, Z., Thermal-expansion offset for high-performance fuel cell cathodes. *Nature* **2021,** *591* (7849), 246-251.
205. Fu, Y.-P.; Subardi, A.; Hsieh, M.-Y.; Chang, W.-K., Electrochemical properties of $La_{0.5}Sr_{0.5}Co_{0.8}M_{0.2}O_{3-\delta}$ (M=Mn, Fe, Ni, Cu) perovskite cathodes for IT-SOFCs. *Journal of the American Ceramic Society* **2016,** *99* (4), 1345-1352.
206. Wan, Y.; Xing, Y.; Li, Y.; Huan, D.; Xia, C., Thermal cycling durability improved by doping fluorine to $PrBaCo_2O_{5+\delta}$ as oxygen reduction reaction electrocatalyst in

intermediate-temperature solid oxide fuel cells. *Journal of Power Sources* **2018,** *402*, 363-372.

207. Wang, Y.; Jin, F.; Hao, X.; Niu, B.; Lyu, P.; He, T., B–site-ordered Co-based double perovskites $Sr_2Co_{1-x}Nb_xFeO_{5+\delta}$ as active and stable cathodes for intermediate-temperature solid oxide fuel cells. *Journal of Alloys and Compounds* **2020,** *829*, 154470.
208. Wei, B.; Lü, Z.; Huang, X.; Miao, J.; Sha, X.; Xin, X.; Su, W., Crystal structure, thermal expansion and electrical conductivity of perovskite oxides $Ba_xSr_{1-x}Co_{0.8}$Fe0.2$O_{3-\delta}$ (0.3≤x≤0.7). *Journal of the European Ceramic Society* **2006,** *26* (13), 2827-2832.
209. An, H.; Lee, H.-W.; Kim, B.-K.; Son, J.-W.; Yoon, K. J.; Kim, H.; Shin, D.; Ji, H.-I.; Lee, J.-H., A 5 × 5 cm^2 protonic ceramic fuel cell with a power density of 1.3 W cm^{-2} at 600 °C. *Nature Energy* **2018,** *3* (10), 870-875.
210. Shan, D.; Gong, Z.; Wu, Y.; Miao, L.; Dong, K.; Liu, W., A novel $BaCe_{0.5}Fe_{0.3}Bi_{0.2}O_{3-\delta}$ perovskite-type cathode for proton-conducting solid oxide fuel cells. *Ceramics International* **2017,** *43* (4), 3660-3663.
211. Xia, Y.; Xu, X.; Teng, Y.; Lv, H.; Jin, Z.; Wang, D.; Peng, R.; Liu, W., A novel $BaFe_{0.8}Zn_{0.1}Bi_{0.1}O_{3-\delta}$ cathode for proton conducting solid oxide fuel cells. *Ceramics International* **2020,** *46* (16, Part A), 25453-25459.
212. Fan, L.; Su, P.-C., Layer-structured $LiNi_{0.8}Co_{0.2}O_2$: A new triple ($H^+/O^{2-}/e^-$) conducting cathode for low temperature proton conducting solid oxide fuel cells. *Journal of Power Sources* **2016,** *306*, 369-377.
213. Wang, N.; Hinokuma, S.; Ina, T.; Zhu, C.; Habazaki, H.; Aoki, Y., Mixed proton-electron-oxide ion triple conducting manganite as an efficient cobalt-free cathode for protonic ceramic fuel cells. *Journal of Materials Chemistry A* **2020,** *8* (21), 11043-11055.
214. Zhao, Z.; Cui, J.; Zou, M.; Mu, S.; Huang, H.; Meng, Y.; He, K.; Brinkman, K. S.; Tong, J., Novel twin-perovskite nanocomposite of Ba-Ce-Fe-Co-O as a promising triple conducting cathode material for protonic ceramic fuel cells. *Journal of Power Sources* **2020,** *450*, 227609.
215. Ma, J.; Pan, Y.; Wang, Y.; Chen, Y., A Sr and Ni doped Ruddlesden−Popper perovskite oxide $La_{1.6}Sr_{0.4}Cu_{0.6}Ni_{0.4}O_{4+\delta}$ as a promising cathode for protonic ceramic fuel cells. *Journal of Power Sources* **2021,** *509*, 230369.
216. Ding, H.; Wu, W.; Jiang, C.; Ding, Y.; Bian, W.; Hu, B.; Singh, P.; Orme, C. J.; Wang, L.; Zhang, Y., Self-sustainable protonic ceramic electrochemical cells using a triple conducting electrode for hydrogen and power production. *Nature Communications* **2020,** *11* (1), 1907.
217. Li, W.; Guan, B.; Ma, L.; Hu, S.; Zhang, N.; Liu, X., High performing triple-conductive $Pr_2NiO_{4+\delta}$ anode for proton-conducting steam solid oxide electrolysis cell. *Journal of Materials Chemistry A* **2018,** *6* (37), 18057-18066.

218. Kim, J.; Jun, A.; Gwon, O.; Yoo, S.; Liu, M.; Shin, J.; Lim, T.-H.; Kim, G., Hybrid-solid oxide electrolysis cell: A new strategy for efficient hydrogen production. *Nano Energy* **2018,** *44*, 121-126.
219. Huan, D.; Wang, W.; Xie, Y.; Shi, N.; Wan, Y.; Xia, C.; Peng, R.; Lu, Y., Investigation of real polarization resistance for electrode performance in proton-conducting electrolysis cells. *Journal of Materials Chemistry A* **2018,** *6* (38), 18508-18517.
220. Meng, Y.; Gao, J.; Huang, H.; Zou, M.; Duffy, J.; Tong, J.; Brinkman, K. S., A high-performance reversible protonic ceramic electrochemical cell based on a novel Sm-doped $BaCe_{0.7}Zr_{0.1}Y_{0.2}O_{3-\delta}$ electrolyte. *Journal of Power Sources* **2019,** *439*, 227093.
221. Lyagaeva, J.; Danilov, N.; Vdovin, G.; Bu, J.; Medvedev, D.; Demin, A.; Tsiakaras, P., A new Dy-doped $BaCeO_3$–$BaZrO_3$ proton-conducting material as a promising electrolyte for reversible solid oxide fuel cells. *Journal of Materials Chemistry A* **2016,** *4* (40), 15390-15399.
222. Liu, Z.; Cheng, D.; Zhu, Y.; Liang, M.; Yang, M.; Yang, G.; Ran, R.; Wang, W.; Zhou, W.; Shao, Z., Robust bifunctional phosphorus-doped perovskite oxygen electrode for reversible proton ceramic electrochemical cells. *Chemical Engineering Journal* **2022,** *450*, 137787.
223. Zheng, H.; Riegraf, M.; Sata, N.; Costa, R., A double perovskite oxygen electrode in Zr-rich proton conducting ceramic cells for efficient electricity generation and hydrogen production. *Journal of Materials Chemistry A* **2023,** *11* (20), 10955-10970.
224. Jing, J.; Lei, Z.; Zheng, Z.; Wang, H.; Zhang, P.; Wang, Z.; Xu, H.; Yang, Z., Triple conducting perovskite $Ba_{0.95}La_{0.05}Fe_{0.8}Zn_{0.2}O_{3-\delta}$ as oxygen electrode for reversible protonic ceramic cells. *International Journal of Hydrogen Energy* **2023,** *48* (24), 9037-9045.
225. Lei, L.; Zhang, J.; Guan, R.; Liu, J.; Chen, F.; Tao, Z., Energy storage and hydrogen production by proton conducting solid oxide electrolysis cells with a novel heterogeneous design. *Energy Conversion and Management* **2020,** *218*, 113044.
226. Danilov, N.; Lyagaeva, J.; Vdovin, G.; Pikalova, E.; Medvedev, D., Electricity/hydrogen conversion by the means of a protonic ceramic electrolysis cell with $Nd_2NiO_{4+\delta}$-based oxygen electrode. *Energy Conversion and Management* **2018,** *172*, 129-137.
227. Zou, D.; Yi, Y.; Song, Y.; Guan, D.; Xu, M.; Ran, R.; Wang, W.; Zhou, W.; Shao, Z., The $BaCe_{0.16}Y_{0.04}Fe_{0.8}O_{3-\delta}$ nanocomposite: a new high-performance cobalt-free triple-conducting cathode for protonic ceramic fuel cells operating at reduced temperatures. *Journal of Materials Chemistry A* **2022,** *10* (10), 5381-5390.
228. Qiu, H.; Liang, M.; Zhao, J.; Liang, Z.; Jiang, S.; Shi, H.; Wang, W.; Wen, H.; Su, C., A-site cation deficient SrTa0.1Fe0.9O3-δ as a bi-functional cathode for both oxygen ion- and proton-conducting solid oxide fuel cells. *Ceramics International* **2024,** *50* (20, Part C), 40500-40509.

229. Ma, J.; Xu, Y.; Zhu, F.; Chen, Y., An efficient and robust Co-free BaFeO3-based oxygen electrode for protonic ceramic electrochemical cells. *Sustainable Materials and Technologies* **2024,** *40*, e00888.
230. Wang, W.-T.; Wu, Y.-T.; Lin, X.-L.; Babar, Z. U. D.; Li, C.-X.; Liu, C.-Q., Highly Efficient A- and B-Site-Doped Ruddlesden–Popper Perovskite Oxide Nd2–xSrxNi0.9Cu0.1O4+δ as a Cathode for PCFCs. *ACS Applied Energy Materials* **2024,** *7* (6), 2197-2209.
231. Han, D.; Liu, X.; Bjørheim, T. S.; Uda, T., Yttrium-Doped Barium Zirconate-Cerate Solid Solution as Proton Conducting Electrolyte: Why Higher Cerium Concentration Leads to Better Performance for Fuel Cells and Electrolysis Cells. *Advanced Energy Materials* **2021,** *11* (8), 2003149.
232. Yang, Y.; Wu, Y.; Bao, H.; Song, W.; Ni, H.; Tian, D.; Lin, B.; Feng, P.; Ling, Y., An efficient and prospective self-assembled hybrid electrocatalyst for symmetrical and reversible solid oxide cells. *Electrochimica Acta* **2020,** *362*.
233. Xie, C.; Li, J.; Wang, Y.; Li, H.; Hu, H.; Zhou, X.; Wang, X.; Ding, X., Investigation of self-assembled dual-phase cathodes with triple conductivity for protonic ceramic fuel cells. *ACS Applied Energy Materials* **2023,** *6* (11), 5979-5988.
234. He, F.; Teng, Z.; Yang, G.; Zhou, C.; Guan, D.; Chen, S.; Ran, R.; Wang, W.; Zhou, W.; Shao, Z., Manipulating cation nonstoichiometry towards developing better electrolyte for self-humidified dual-ion solid oxide fuel cells. *Journal of Power Sources* **2020,** *460*.
235. Zhou, Y.; Zhang, W.; Kane, N.; Luo, Z.; Pei, K.; Sasaki, K.; Choi, Y.; Chen, Y.; Ding, D.; Liu, M., An efficient bifunctional air electrode for reversible protonic ceramic electrochemical cells. *Advanced Functional Materials* **2021,** *31* (40), 2105386.
236. Liu, Z.; Bai, Y.; Sun, H.; Guan, D.; Li, W.; Huang, W.-H.; Pao, C.-W.; Hu, Z.; Yang, G.; Zhu, Y.; Ran, R.; Zhou, W.; Shao, Z., Synergistic dual-phase air electrode enables high and durable performance of reversible proton ceramic electrochemical cells. *Nature Communications* **2024,** *15* (1), 472.
237. Chen, Y.; Choi, Y.; Yoo, S.; Ding, Y.; Yan, R.; Pei, K.; Qu, C.; Zhang, L.; Chang, I.; Zhao, B.; Zhang, Y.; Chen, H.; Chen, Y.; Yang, C.; deGlee, B.; Murphy, R.; Liu, J.; Liu, M., A highly efficient multi-phase catalyst dramatically enhances the rate of oxygen reduction. *Joule* **2018,** *2* (5), 938-949.
238. Tong, Y.; Meng, X.; Luo, T.; Cui, C.; Wang, Y.; Wang, S.; Peng, R.; Xie, B.; Chen, C.; Zhan, Z., Protonic ceramic electrochemical cell for efficient separation of hydrogen. *ACS Applied Materials & Interfaces* **2020,** *12* (23), 25809-25817.
239. Bello, I. T.; Song, Y.; Yu, N.; Li, Z.; Zhao, S.; Maradesa, A.; Liu, T.; Shao, Z.; Ni, M., Evaluation of the electrocatalytic performance of a novel nanocomposite cathode material for ceramic fuel cells. *Journal of Power Sources* **2023,** *560*, 232722.
240. Lee, H.; Jung, H.; Kim, C.; Kim, S.; Jang, I.; Yoon, H.; Paik, U.; Song, T., Enhanced electrochemical performance and durability of the $BaCo_{0.4}Fe_{0.4}Zr_{0.1}Y_{0.1}O_{3-\delta}$ composite cathode of protonic ceramic fuel cells via

forming nickel oxide nanoparticles. *ACS Applied Energy Materials* **2021,** *4* (10), 11564-11573.

241. Otomo, J.; Furumoto, Y.; Hatano, H.; Hatanaka, T.; Oshima, Y., Nickel oxide redox processes with oxide ion conductor-supported nickel oxide in dry and humidified methane: Effect of oxide ion conductors on induction period in nickel oxide reduction and subsequent hydrogen production. *Fuel* **2013,** *104*, 691-697.
242. Yu, N.; Bello, I. T.; Chen, X.; Liu, T.; Li, Z.; Song, Y.; Ni, M., Rational design of Ruddlesden-popper perovskite ferrites as air electrode for highly active and durable reversible protonic ceramic cells. *Nano-micro letters* **2024**.
243. Wang, M.; Su, C.; Zhu, Z.; Wang, H.; Ge, L., Composite cathodes for protonic ceramic fuel cells: Rationales and materials. *Composites Part B: Engineering* **2022,** *238*, 109881.
244. Song, Y.; Chen, Y.; Xu, M.; Wang, W.; Zhang, Y.; Yang, G.; Ran, R.; Zhou, W.; Shao, Z., A cobalt-free multi-phase nanocomposite as near-ideal cathode of intermediate-temperature solid oxide fuel cells developed by smart self-assembly. *Advanced Materials* **2020,** *32* (8).
245. Yang, G.; Zhou, W.; Liu, M.; Shao, Z., Enhancing electrode performance by exsolved nanoparticles: A superior cobalt-free perovskite electrocatalyst for solid oxide fuel cells. *ACS Applied Materials & Interfaces* **2016,** *8* (51), 35308-35314.
246. Yu, J.; Rosso, K. M.; Bruemmer, S. M., Charge and Ion Transport in NiO and Aspects of Ni Oxidation from First Principles. *The Journal of Physical Chemistry C* **2012,** *116* (2), 1948-1954.
247. Liao, C.; Yang, B.; Zhang, N.; Liu, M.; Chen, G.; Jiang, X.; Chen, G.; Yang, J.; Liu, X.; Chan, T.-S.; Lu, Y.-J.; Ma, R.; Zhou, W., Constructing Conductive Interfaces between Nickel Oxide Nanocrystals and Polymer Carbon Nitride for Efficient Electrocatalytic Oxygen Evolution Reaction. *Advanced Functional Materials* **2019,** *29* (40), 1904020.
248. Shin, J. F.; Xu, W.; Zanella, M.; Dawson, K.; Savvin, S. N.; Claridge, J. B.; Rosseinsky, M. J., Self-assembled dynamic perovskite composite cathodes for intermediate temperature solid oxide fuel cells. *Nature Energy* **2017,** *2* (3), 16214.
249. Hu, D.; Kim, J.; Niu, H.; Daniels, L. M.; Manning, T. D.; Chen, R.; Liu, B.; Feetham, R.; Claridge, J. B.; Rosseinsky, M. J., High-performance protonic ceramic fuel cell cathode using protophilic mixed ion and electron conducting material. *Journal of Materials Chemistry A* **2022,** *10* (5), 2559-2566.
250. Wang, D.; Xia, Y.; Lv, H.; Miao, L.; Bi, L.; Liu, W., $PrBaCo_{2-x}TaxO_{5+\delta}$ based composite materials as cathodes for proton-conducting solid oxide fuel cells with high CO_2 resistance. *International Journal of Hydrogen Energy* **2020,** *45* (55), 31017-31026.